

WATERMOVEMENT OVER A HORIZONTAL BED AND SOLITARY SANDDUNE

A.P.P. Terres

May 1984

R/1984/H/8

Delft University of Technology

Department of Civil Engineering

Fluid Mechanics Group

CONTENTS

Summary	2
Acknowledgements	2
1. Introduction	3
1.1 General	3
1.2 Definitions and assumptions with respect to fluid and sediment	5
2. Theory	7
2.1 Introduction	7
2.2 Watermovement	7
2.2.1 General	7
2.2.2 Conservation of mass and momentum	7
2.2.3 Uniform channel flow	10
2.2.4 Non-uniform channel flow	13
2.2.5 The k- ϵ model	16
2.2.6 Sidewall effects for channel flow	20
2.3 Sedimentmovement	21
2.3.1 General	21
2.3.2 Conservation of mass equation	21
2.3.3 A simple transport equation	23
2.3.4 A comprehensive transport equation	25
3. Experiments	28
3.1 Introduction	28
3.2 Experimental facilities	28
3.3 Flowconditions	31
3.3.1 General	31
3.3.2 Horizontal bed situation	31
3.3.3 Solitary dune situation	31
3.4 Measurements	32
3.4.1 General	32
3.4.2 Measured quantities	32
3.4.3 Influence of the measuring volume	34
3.5 Processing of measured data	35
4. Results	41
4.1 Introduction	41
4.2 Watermovement	41
4.2.1 General	41
4.2.2 Horizontal bed situation	41
4.2.3 Solitary dune situation	53
4.3 Sedimentmovement	63
4.3.1 General	63
4.3.2 Sediment transport	63
4.3.3 Sediment transport and flowquantities	64
4.4 Recapitulation	65
4.4.1 Horizontal bed situation	65
4.4.2 Solitary dune situation	66
5. Recommendations	67
5.1 Introduction	67
5.2 Solitary dune	67
5.3 Measuring equipment	67
5.4 Experiments	68
5.5 Theory	69
Symbols	70
Literature	72
Appendix A (Operation of the Laser Doppler Anemometer, heterodyne system)	--
Appendix B (Preliminary experiments with a dune on a conveyor)	--
Appendix C (Tables of measured data)	--

Summary

In order to predict waterlevel changes in rivers due to floodwaves and local bedshapes for navigation, the local behaviour of the riverbed should be known.

In many cases the bed of a river consists of dunes, which propagate downstream due to the sediment transport along the dunes.

In this report mainly the watermovement but also the sediment transport along a dune is studied.

The investigation consists of a theoretical and an experimental part.

In the theoretical part a calculation of the flowfield above a dune is carried out using a computer model for the watermovement (ODYSSEE computer program of the Delft Hydraulics Laboratory, DHL).

In the experimental part the mechanism of the local sediment transport along the dune is studied.

The experimental set up consists of a solitary sanddune on a conveyor belt in a flume.

The position of the dune is constant due to: conveyor belt velocity = - propagationvelocity of the dune.

In this situation the flowfield above the dune is measured using a Laser Doppler Anemometer (LDA), which is tested first in a uniform flow situation.

The local sediment transport, which is known along the steady dune, is related to the local bedshearstress.

Acknowledgements

The investigation presented in this report lasted 1½ year, from the moment the preparations for the project started until the final version of the report.

During the project about 30 persons, with different specializations, were involved.

I want to thank the next institutes and persons, in alphabetic sequence, for their contributions:

Delft Hydraulics Laboratory; for the information about the Laser Doppler Anemometer, for the use of their computer facilities in Delft as well as in 'de Voorst', and the enormous help I received when I used the ODYSSEE computer program.

Fluid Mechanics Group of the Delft University of Technology; for their advice concerning the experiments and the treatment of data by the computer.

Laboratory of Fluid Mechanics of the Delft University of Technology; for their stimulating support during the experiments, the treatment of data and information about theoretical topics.

Especially the superb constructed conveyor and the adapted Laser Doppler equipment were most important for a succesful experiment.

prof. dr. ir. G. Ooms, as external adviser; for his valuable advice, suggestions and guidance in the field of turbulence, and his support during the writing of the report.

ir. J.S. Ribberink, as direct mentor; for the gigantic amout of time he spend on the project, the guidance during the experiments and during the writing of the report, and for his valuable advice in general.

prof. dr. ir. C.B. Vreugdenhil, as adviser; for his valuable advice in the field of numerical methods during the use of the ODYSSEE program and during the writing of the report.

prof. dr. ir. M. de Vries, as chief mentor; for his thoughtful advice in the field of fluidmechanics, sediment transport and during the writing of the report, and for the 'help when needed' which was essential for a succesful project.

1. Introduction

1.1 General

Sediment transport in alluvial rivers can be divided into bedload transport, which occurs mainly over the bottom of the river and suspended transport, which occurs between bottom and watersurface.

Changes in the geometry of the riverbed due to changing flowconditions are important for the estimation of the local bedroughness and local bedshape.

The flowconditions, in turn, are influenced by the riverbed geometry, which makes the interaction flow-sediment transport very complex.

The forecasting of the local waterlevel in a river due to floodwaves, for example, or local bedlevels for navigation requires insight in the behaviour of the riverbed.

The bedload transport can take place in different ways. Sediment particles are transported downstream, in the vicinity of the bed, over dunes, ripples or over a flat bed.

The particles move with a velocity almost equal to the flowvelocity of the water near the bed.

Dunes and ripples propagate downstream, with a velocity which is an order smaller than that of the individual particles.

In a natural situation dunes and ripples are shaped three-dimensionally, are catching up eachother and so influence the local flowconditions of the river.

To get insight in the interaction flow-sediment transport, detailed investigations of the sediment transport mechanism are necessary.

In this report an investigation of the local watermovement and local bedload transport over a dune is described.

The phenomena are studied under quasi-steady flowconditions in a vertical plane parallel to the main flow direction.

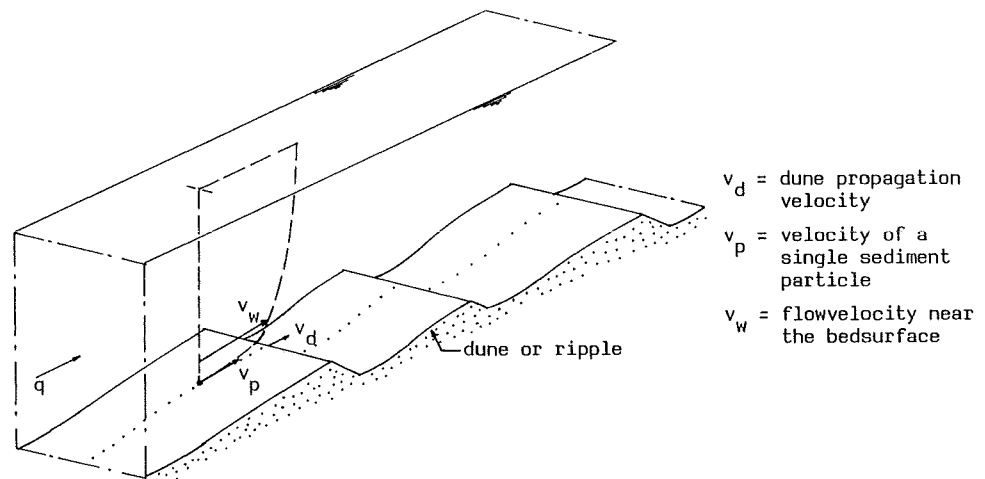


Figure 1.1: Bedshape and characteristic velocities for a dune or ripple, per unit width.

The investigation is divided into a theoretical part and an experimental part.

In the theoretical part, the watermovement and the sediment movement are studied separately.

The Navier-Stokes equation is used to describe the watermovement. For the description of the turbulent viscosity there has been chosen for a two-dimensional $k-\epsilon$ model.

With this model accelerating flows and wakes can be described satisfactory.

The $k-\epsilon$ model is used in the computer program ODYSSEE of the Delft Hydraulics Laboratory (DHL), with the program a numerical solution of a flowfield is derived.

For the sediment movement different models for local bedload transport can be used.

However, specific models for sediment transport are not studied, but a general treatment of bedload transport is given. Furthermore two simple models for local changes of the duneheight are treated.

In the experimental part, experiments carried out in a straight flume will be described. The set up of the experiments must be so, that measurements can be carried out easily and measurements of mean flow velocities as well as turbulent flow quantities are possible. An important link can be made between the local sediment transport and the local bed shear stress.

In the experiments measurements could have been carried out over a series of moving or solid dunes in a flume.

However, measurements over moving dunes are difficult and measurements over solid dunes have already been carried out (Raudkivi, 1976).

There has been chosen for a 'solitary dune' which propagates downstream due to the flow, but is placed on a conveyor belt. The velocity of the belt is equal but opposite directed with respect to the dune-propagating velocity.

In this way the dune 'stands still' in the flume. The experiment is carried out in a flume with horizontal bottom upstream and downstream the solitary dune.

For a description of the development of the experiment to a solitary dune, see appendix B.

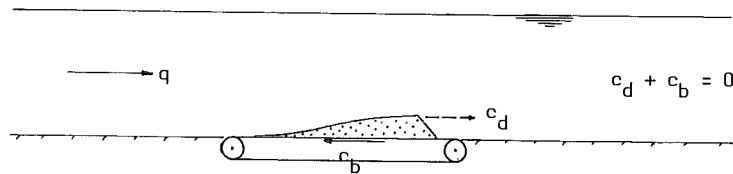


Figure 1.2: Solitary dune on a conveyor.

Advantages of this set up are:

- The measurements can be carried out easily (stationary dune) and are done with a Laser Doppler Anemometer (LDA) which measures instantaneous flow velocities in a very small area in the water.
- The local sediment transport can be determined easily as the product of the conveyor belt velocity and the local dune height.
- With respect to a solid dune the influence of the moving sediment particles on the flow near the dune surface is present.
- For the numerical solution of the flowfield a simple inflow boundary can be chosen. Upstream the dune a flow over a horizontal bed occurs with developed (logarithmic) flow velocity-, turbulent energy- and shear stress profile.
- The $k-\epsilon$ model can be tested in this flow situation, numerical results can be compared with results of measurements.

A disadvantage is that the situation is not similar to the situation with a series of dunes, but the investigation of sediment transport in an accelerating flow is still interesting.

In this report the results of theoretical study and experiments are given:

- Treatment of applications of the Navier-Stokes equation, treatment of the $k-\epsilon$ model and treatment of simple models for local dune height changes.
- Results of measurements carried out with the LDA in a flume with horizontal bed. The LDA is specially adapted for the experiments and tested in a flow situation for which analytical solutions of mean flow velocity and shear stress profiles exist.
- Results of measurements above the solitary dune, carried out with the LDA.

The results are compared with the numerical solution of the flowfield calculated with the computer program ODYSSEE (DHL) based on a two-dimensional $k-\epsilon$ model.

- Relating the local sediment transport and local flow quantities near the dune surface.

1.2 Definitions and assumptions with respect to fluid and sediment

To describe the physical behaviour of the fluid and sediment mathematically, first some definitions and assumptions must be made.

The mathematical description is done in a three-dimensional orthogonal coordinate system, with the positive x_3 -axis pointed upward with respect to gravity.

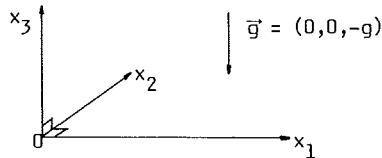


Figure 1.3: Definition of the coordinate system.

The equations are often simplified to equations for a vertical plane (x_1, x_3) because, whether the x_2 -direction is not of importance, or the simplification results in a less complicated equation which can be solved more easily.

The Einstein summation convention is used, with $i=1,2,3$ this holds:

x_i	means	x_1, x_2, x_3
$\sum x_i$	means	$x_1 + x_2 + x_3$
$\frac{\partial U_i}{\partial x_i}$	means	$\frac{\partial U_1}{\partial x_1} + \frac{\partial U_2}{\partial x_2} + \frac{\partial U_3}{\partial x_3}$
$\frac{\partial \tau_{ij}}{\partial x_i}$	means	$\frac{\partial \tau_{1j}}{\partial x_1} + \frac{\partial \tau_{2j}}{\partial x_2} + \frac{\partial \tau_{3j}}{\partial x_3}$

The laws for conservation of mass and momentum are regarded with respect to a control volume. The fluid and sediment move through this volume.

The control volume has an arbitrary but steady position in the coordinate system and is constant of size. The fluid and sediment are thus considered in an Eulerian frame.

The volume of the control volume reads: $\Delta V = dx_1 \cdot dx_2 \cdot dx_3$ and becomes zero at the limit and physical laws hold for this mathematical point.

This yields, however, that molecules are infinite small, which they are definitely not !

So when $\Delta V = 0$, what is the definition of the density, temperature, velocity, acceleration and pressure ?

The problem will be solved here for the density, the other properties can be treated in a similar way.

The density is defined by: $\Delta M / \Delta V$ in which ΔM is an arbitrary mass and ΔV is an arbitrary volume.

In general it holds that for large volumes the density depends on the magnitude of the volume.

When ΔV is taken smaller and smaller the density appears to be constant.

At very small values of ΔV the density is dependant on ΔV again and is strongly fluctuating with decreasing ΔV , because the amount of molecules in the volume can fluctuate strongly.

At the limit $\Delta V = 0$, no molecule is present in the volume and the density becomes zero.

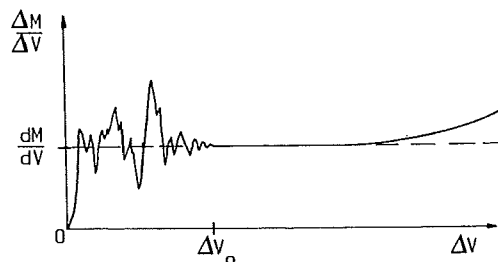


Figure 1.4: Density as function of the control volume size (from Prandtl, 1957).

In practice, however, $\Delta V = \Delta V_0$ will be taken small enough to make the density constant and finite but still large enough to prevent the influence of the number of molecules on the density.

The definition of the density reads:

$$\lim_{V \rightarrow 0} \frac{\Delta M}{\Delta V} = \frac{dM}{dV}$$

The control volume ΔV_0 is now a physical point instead of a mathematical point.

In this way the fluid and sediment can be treated as continua and molecular forces can be neglected.

The sediment consists of discrete particles of different size, shape and density in practice and the particles are very large compared to the molecular scale.

However, the derivations made in this report are done for sediment as a continuum, which is a reasonable approach because time averaged considerations are held.

In this way the sediment transport can be seen as a flow with mean physical properties.

In the report the general terms 'fluid' and 'sediment' are often used.

However, more specific terms to indicate the different phases are 'water' and 'sand'.

This should be kept in mind when assumptions are made or effects are neglected in derivations.

2. Theory

2.1 Introduction

The movement of water and sediment is treated in separate mathematical models.

A conservation of mass equation and conservation of momentum equation are set up for water as well as for sediment.

The conservation of mass equation together with the conservation of momentum equation describe the water-movement generally and are treated separately.

A good description of the conservation of momentum is the Navier-Stokes equation which is appropriate for watermovements in many situations.

For turbulent flow a 'turbulent viscosity' appears in the Navier-Stokes equation and for this viscosity different mathematical models exist.

In this report only two turbulent viscosity models are treated, the mixing length model of Prandtl and a two-equation k- ϵ model.

The mixing length model is based on an analogy with the kinetic gas theory (see Rodi, 1980).

The k- ϵ model describes the turbulent viscosity with an extensive mathematical model, which describes two dimensional flows, even with wakes, reasonably well, see the applications in Rodi (1980).

Furthermore the ODYSSEE computer program (Alfrink, 1983) is based on this k- ϵ model.

ODYSSEE was used to derive numerical solutions for a flowfield which occurred in the experiments.

A general conservation of momentum equation for the sediment is yet not known (1984).

In this report two different equations for the conservation of momentum are used to describe the sediment-movement.

2.2 Watermovement

2.2.1 General

The conservation of mass and momentum equations hold generally, the choice of the mixing length model or the k- ϵ model depends on the type of flow or the desired accuracy of the calculation.

The difference of a mixing length model and a k- ϵ model lies fundamentally in the description of the turbulent viscosity.

In the mixing length model the turbulent viscosity is expressed directly in length scales.

In the k- ϵ model, however, the turbulent viscosity is expressed in turbulent energy and energy dissipation.

2.2.2 Conservation of mass and momentum

The equations are derived in an orthogonal x_1, x_2, x_3 -coordinate system.

The density of the fluid is $\rho(x_1, x_2, x_3, t)$ and the flowvelocity \bar{U} consists of the flowvelocity components $U_i(x_1, x_2, x_3, t)$ with $i=1, 2, 3$.

The equations are worked out for a stationary two dimensional flow in a vertical plane. Also an expression for the shearstress under these circumstances is derived.

Conservation of mass

It generally holds for a fluid that the difference of inflow and outflow of mass through a control volume is equal to the increase of mass in the control volume in time (an Eulerian frame).

This yields:

$$\frac{\partial \rho}{\partial t} + \frac{\partial(\rho \cdot U_i)}{\partial x_i} = 0 \quad ; \quad i=1, 2, 3 \quad (2-1)$$

In the experiments, described in this report, the fluid is water and no extreme density differences occur, so it safely can be stated that ρ is constant in time and space.

Equation (2-1) now reads:

$$\frac{\partial \rho_i}{\partial x_i} = 0 \quad ; \quad i=1,2,3 \quad (2-2)$$

The flow is further assumed to be two-dimensional in the vertical plane with flowvelocity components,

$$\rho_1 = \rho_1(x_1, x_3, t) \text{ and } \rho_3 = \rho_3(x_1, x_3, t) .$$

So equation (2-2) reduces to:

$$\frac{\partial \rho_1}{\partial x_1} + \frac{\partial \rho_3}{\partial x_3} = 0 \quad (2-3)$$

The instantaneous flowvelocity components ρ_1 and ρ_3 can both be separated in a mean flowvelocity and a turbulent flowvelocity, the Reynolds decomposition:

$$\begin{aligned} \rho_1(x_1, x_3, t) &= U_1(x_1, x_3, t) + u_1(x_1, x_3, t) \\ \rho_3(x_1, x_3, t) &= U_3(x_1, x_3, t) + u_3(x_1, x_3, t) \end{aligned}$$

These flowvelocities are defined as follows:

$$\bar{\rho}_i = U_i = \frac{1}{T} \int_0^T \rho_i dt \quad ; \quad \bar{u}_i = \frac{1}{T} \int_0^T u_i dt \equiv 0$$

For example: $\frac{\partial \bar{\rho}_1}{\partial x_1} = \frac{1}{T} \int_0^T \frac{\partial \rho_1}{\partial x_1} dt = \frac{\partial U_1}{\partial x_1} \quad ; \quad \bar{\rho}_1 \bar{\rho}_1 = \frac{1}{T} \int_0^T \rho_1 \rho_1 dt = U_1 U_1 + \overline{u_1 u_1} \quad ; \quad \bar{\rho}_1 \bar{\rho}_3 = \frac{1}{T} \int_0^T \rho_1 \rho_3 dt = U_1 U_3 + \overline{u_1 u_3}$

The time T is in principle infinite long, but in practice a finite value of T is accurate enough.

A mean flowvelocity depending on time requires deviding the time axis into areas in which the flowvelocity U_1 and U_3 do not alter significantly, this case is not treated further.

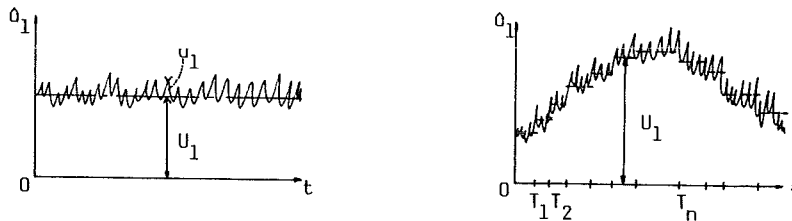


Figure 2.1: example of instantaneous flowvelocity, constant mean velocity and changing with time.

After decomposition, equation (2-3) results in two equations:

conservation of mass for mean flowvelocity:
$$\frac{\partial U_1}{\partial x_1} + \frac{\partial U_3}{\partial x_3} = 0 \quad (2-4)$$

conservation of mass for turbulent flowvelocity:
$$\frac{\partial u_1}{\partial x_1} + \frac{\partial u_3}{\partial x_3} = 0 \quad (2-5)$$

Conservation of momentum

Generally Newton's second law can be applied to the fluid in a control volume in the orthogonal x_1, x_2, x_3 -coordinate system.

There must be equilibrium between the acceleration of the mass in the control volume and external forces acting on the control volume.

This leads to the Navier-Stokes equation, which is exact for a laminar flow of homogeneous fluid, and gives generally a good description for turbulent flow.

The equation yields:

$$\frac{d\bar{U}}{dt} = - \frac{1}{\rho} \frac{\partial \bar{p}}{\partial x_i} + \frac{1}{\rho} \frac{\partial \bar{\tau}}{\partial x_i} + \bar{g} \quad ; \quad i=1,2,3 \quad (2-6)$$

A complete derivation of equation (2-6) can be found in Prandtl (1957).

The left hand side of equation (2-6) is the acceleration per unit mass of the fluid and reads:

$$\frac{\partial a_i}{\partial t} + u_j \frac{\partial a_i}{\partial x_j} \quad ; \quad i=1,2,3 \quad \text{and} \quad j=1,2,3$$

The first term on the right hand side of (2-6) is a pressure gradient, $\rho(x_1, x_2, x_3) = P(x_1, x_2, x_3) + \rho(x_1, x_2, x_3)$. The second term on the right hand side of (2-6) is the stress tensor of viscosity acting on the control volume and reads:

$$\bar{\tau} = \tau_{ij} = \rho \cdot v \left(\frac{\partial a_i}{\partial x_j} + \frac{\partial a_j}{\partial x_i} \right) \quad ; \quad i=1,2,3 \quad \text{and} \quad j=1,2,3 \quad (2-7)$$

The third term on the right hand side of (2-6) is the gravity vector: $\bar{g} = (0, 0, -g)$

For further considerations the flow velocity and derivatives in the x_2 -direction are omitted.

The equations are derived for a vertical plane so, equation (2-6) can be rewritten with the equations stated above, equation (2-3) and taking the average over a period T .

This yields conservation of momentum equations in the x_1 and x_3 direction:

$$\frac{\partial u_1^2}{\partial x_1} + \frac{\partial u_1 u_3}{\partial x_3} = -\frac{1}{\rho} \frac{\partial P}{\partial x_1} + \frac{\partial}{\partial x_1} \left(v \frac{\partial u_1}{\partial x_1} - \overline{u_1^2} \right) + \frac{\partial}{\partial x_3} \left(v \frac{\partial u_1}{\partial x_3} - \overline{u_1 u_3} \right) \quad (2-8)$$

$$\frac{\partial u_1 u_3}{\partial x_1} + \frac{\partial u_3^2}{\partial x_3} = -\frac{1}{\rho} \frac{\partial P}{\partial x_3} + \frac{\partial}{\partial x_1} \left(v \frac{\partial u_3}{\partial x_1} - \overline{u_1 u_3} \right) + \frac{\partial}{\partial x_3} \left(v \frac{\partial u_3}{\partial x_3} - \overline{u_3^2} \right) - g \quad (2-9)$$

The terms $\overline{u_1^2}$, $\overline{u_1 u_3}$ and $\overline{u_3^2}$ are the Reynolds stresses.

The equations (2-8) and (2-9) are conservation of momentum equations for a turbulent flow averaged over a period T and are too complex to give an analytical solution in general.

Shearstress equation

In some cases an approximated analytical solution of (2-8) and (2-9) can be found, like the flow in one of the experiments, a stationary flow in a straight flume with rectangular cross-section and horizontal bottom. In this particular case the flowfield can be approximated as a boundary layer in a vertical plane. The layer reaches from the horizontal bottom of the flume to the slightly inclined watersurface.

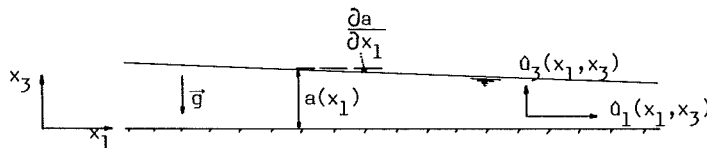


Figure 2.2: Definition of the flowfield

The terms on the left hand side of (2-8) and (2-9) can be simplified with the aid of the conservation of mass equation (2-4), because the next expressions hold:

$$\frac{\partial u_1^2}{\partial x_1} + \frac{\partial u_1 u_3}{\partial x_3} = u_1 \cdot \frac{\partial u_1}{\partial x_1} + u_3 \cdot \frac{\partial u_1}{\partial x_3}$$

$$\frac{\partial u_1 u_3}{\partial x_1} + \frac{\partial u_3^2}{\partial x_3} = u_1 \cdot \frac{\partial u_3}{\partial x_1} + u_3 \cdot \frac{\partial u_3}{\partial x_3}$$

First equation (2-9) is further simplified. Length scales and velocity scales can be defined to neglect some terms, this is clearly outlined in Tennekes (1977).

The velocity scales are $u_1 \approx O(v)$ and $u_3 \approx O(v)$.

The length scales (scales of change in x_1 -direction) are $\partial x_1 \approx O(L)$ and $\partial x_3 \approx O(\ell)$.

With the conservation of mass equations (2-4) and (2-5) this yields: $u_3 \approx O(v \cdot \ell / L)$ and $u_3 \approx O(v \cdot \ell / L)$.

For the case of parallel flow the ratio $\ell/L \rightarrow 0$ and for nearly parallel flow $\ell/L \ll 1$; this yields for some terms: $\partial/\partial x_1 \ll \partial/\partial x_3$.

With these definitions, equation (2-9) becomes:

$$0 = -\frac{1}{\rho} \frac{\partial P}{\partial x_3} + \frac{\partial}{\partial x_3} \left(\nu \frac{\partial u_3}{\partial x_3} - \overline{u_3^2} \right) - g \quad (2-10)$$

Integrating of (2-10) from $x_3=0$ to $x_3=a(x_1)=a$, with boundary conditions at $x_3=0$ which read: $P = \rho \cdot g \cdot a$, $\partial u_3/\partial x_3 = 0$ and $\overline{u_3^2} = 0$, the result is:

$$0 = -\frac{1}{\rho} P + g \cdot a + \nu \frac{\partial u_3}{\partial x_3} - \overline{u_3^2} - g \cdot x_3 \quad (2-11)$$

The derivative to x_1 of (2-11) reads:

$$\frac{1}{\rho} \frac{\partial P}{\partial x_1} = g \cdot \frac{\partial a}{\partial x_1} + \nu \frac{\partial^2 u_3}{\partial x_1 \partial x_3} - \frac{\partial \overline{u_3^2}}{\partial x_1} \quad (2-12)$$

After simplifying, equation (2-8) reads:

$$u_1 \frac{\partial u_1}{\partial x_1} + u_3 \frac{\partial u_1}{\partial x_3} = -\frac{1}{\rho} \frac{\partial P}{\partial x_1} + \frac{\partial}{\partial x_3} \left(\nu \frac{\partial u_1}{\partial x_3} - \overline{u_1 u_3} \right)$$

Substitution of equation (2-12) gives finally:

$$u_1 \frac{\partial u_1}{\partial x_1} + u_3 \frac{\partial u_1}{\partial x_3} = -g \frac{\partial a}{\partial x_1} - \nu \frac{\partial^2 u_3}{\partial x_1 \partial x_3} + \nu \frac{\partial^2 u_1}{\partial x_3^2} - \frac{\partial \overline{u_3^2}}{\partial x_1} - \frac{\partial \overline{u_1 u_3}}{\partial x_3} \quad (2-13)$$

This equation can be simplified further. In Tennekes (1977) a length scale consideration is carried out to neglect the term $u_3 \cdot \partial u_1/\partial x_3$ with respect to $u_1 \cdot \partial u_1/\partial x_1$, which seem to be both of order (v^2/L) . For this flowfield, however, it can be stated that near the bottom u_3 is almost zero and $\partial u_1/\partial x_3$ is large and at some distance from the bottom u_3 has a certain value but $\partial u_1/\partial x_3$ is almost zero.

In both cases $u_3 \cdot \partial u_1/\partial x_3 \ll u_1 \cdot \partial u_1/\partial x_1$.

Furthermore $\frac{\partial^2 u_3}{\partial x_1 \partial x_3} = 0 (v/L^2)$ can be neglected with respect to $\frac{\partial^2 u_1}{\partial x_3^2} = 0 (v/\ell^2)$.

And finally $\frac{\partial \overline{u_3^2}}{\partial x_1} = 0 (v^2/L)$ can be neglected with respect to $\frac{\partial \overline{u_1 u_3}}{\partial x_3} = 0 (v^2/\ell)$.

The conservation of momentum equation after all these assumptions reads:

$$u_1 \frac{\partial u_1}{\partial x_1} = -g \frac{\partial a}{\partial x_1} + \frac{1}{\rho} \frac{\partial \tau}{\partial x_3} \quad (2-14)$$

with: $\frac{\tau}{\rho} = \nu \frac{\partial u_1}{\partial x_3} - \overline{u_1 u_3} \quad (2-15)$

Equation (2-15) expresses the total shearstress acting on the control volume, this stress consists of two components. The first component is the viscous shearstress which is dominant near the wall in a turbulent flow.

The second component is the Reynolds shearstress which is dominant at some distance from the wall.

In which region the components are dominant will be explained in the next sub-section.

2.2.3 Uniform channel flow

Under uniform flow conditions, $\partial u_1/\partial x_1 = 0$, and with some simple assumptions, a mean flow velocity profile in the boundary layer and even for the complete waterdepth can be determined.

Some layers in the fluid with specific properties have to be defined for this. Also an expression for the shearstress in the boundary layer and even for the complete waterdepth can be derived.

Definition of layers

In a turbulent flow the smallest length scale of the turbulence is the Kolmogorov micro scale, which reads, see Tennekes (1977):

$$\eta = (\nu^3/\epsilon)^{1/4}$$

and $\epsilon \cong u_*^3/(\kappa \cdot x_3)$ is the dissipation rate of the turbulence near the wall. In this expression u_* is the shearstressvelocity defined as:

$$u_*^2 = \tau(x_3=0)/\rho$$

A dimensionless distance is defined as: $x_3^+ \equiv x_3 \cdot u_* / \nu$ (a kind of Reynoldsnumber).

So the Kolmogorov micro scale reads:

$$\eta = \kappa^{1/4} \cdot x_3 \cdot (x_3^+)^{-3/4}$$

Near the wall the integral scale of the turbulence is, according to the Prandlt mixing length theory:

$$l \cong \kappa \cdot x_3$$

The dimensionless Kolmogorov length scale reads:

$$\eta^+ = \eta \cdot u_* / \nu = (\kappa \cdot x_3^+)^{1/4}$$

(2-16)

and the dimensionless integral scale reads:

$$l^+ = l \cdot u_* / \nu = \kappa \cdot x_3^+$$

Both relations are sketched in figure 2.3:

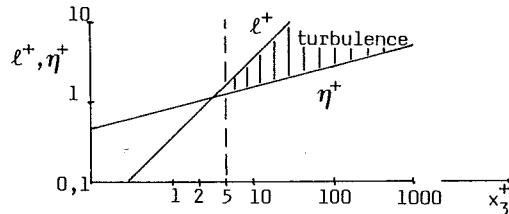


Figure 2.3: Integral scale and Kolmogorov micro scale, from Tennekes (1977).

For $x_3^+ < 2,5$ it follows that $l^+ < \eta^+$ which is not possible because the smallest turbulence scale is the Kolmogorov micro scale. So the region $x_3^+ < 2,5$ of the flow is not turbulent.

In practice the following regions are defined:

1. viscous sublayer, $x_3^+ < 5$ and $\tau/\rho = \nu \frac{\partial u_1}{\partial x_3}$ (2-17)

2. buffer layer, $5 < x_3^+ < 30$ and $\tau/\rho = \nu \frac{\partial u_1}{\partial x_3} - \overline{u_1 u_3}$ (2-15)

3. inertial sublayer, $x_3^+ < 30, x_3 \ll a$ and $\tau/\rho = -\overline{u_1 u_3}$ (2-18)

4. outer region, $x_3^+ < 30, x_3 < a$ and $\tau/\rho = -\overline{u_1 u_3}$ (2-18)

Now a mean flowvelocity profile can be derived for the viscous and inertial sublayer and for the outer region.

Mean flowvelocity and shearstress profiles

1. very close to the wall and for $x_3^+ < 5$, the shearstress reads: $\nu \partial U_1 / \partial x_3 \cong u_*^2$, so $\partial U_1 / \partial x_3 \cong u_*^2 / \nu$. This equation can be solved, with the boundary condition at $x_3=0, U_1=0$:

$$U_1 = u_*^2 \cdot x_3 / \nu$$

or dimensionless with $U_1^+ = U_1 / u_*$ this reads:

$$U_1^+ = x_3^+ \tag{2-19}$$

3. At some distance from the wall, for $x_3^+ > 30$, but still in a region where $x_3 \ll a$, so $\tau/\rho \cong u_*^2 = \tau(x_3=0)/\rho$ the shearstress reads: $-\overline{u_1 u_3} \cong u_*^2$.

The Reynoldsstress is expressed according to Boussinesq as:

$$-\overline{u_1 u_3} = \nu_t \cdot \frac{\partial U_1}{\partial x_3}$$

in which ν_t is the turbulent viscosity, a flow property.

The turbulent viscosity now, is expressed according to Prandtl's mixing length theory:

$$\nu_t = \ell^2 \cdot \frac{\partial U_1}{\partial x_3} \quad \text{and} \quad \ell = \kappa \cdot x_3$$

So finally $u_*^2 = \kappa^2 \cdot x_3^2 \cdot (\frac{\partial U_1}{\partial x_3})^2$ with boundary condition at $x_3 = z_0$, $U_1 = 0$ results in:

$$U_1 = u_* / \kappa \cdot \ln(x_3 / z_0) \tag{2-20}$$

Dimensionless this equation reads:

$$U_1^+ = 1/\kappa \cdot \ln x_3^+ + C \tag{2-21}$$

The equations (2-19) and (2-21) follow from assumptions for τ/ρ and not from the conservation of momentum equation (2-14).

2. The buffer layer lies between case 1 and 3, the shearstress can be expressed as:

$$\tau/\rho = (\nu + \nu_t) \cdot \frac{\partial U_1}{\partial x_3}$$

4. For the region, $x_3^+ > 30$, but not too close to the wall, $x_3 < a$ so $\tau/\rho < u_*^2$, another assumption can be made for an uniform flow, $\partial U_1 / \partial x_1 = 0$.

Equation (2-14) then results in: $0 = -g \cdot \frac{\partial a}{\partial x_1} + \frac{1}{\rho} \cdot \frac{\partial \tau}{\partial x_3}$

Integration of this equation with boundary conditions at $x_3=0$; $\tau/\rho = g \cdot a \cdot \frac{\partial a}{\partial x_1} = u_*^2$ and at $x_3=a$; $\tau/\rho = 0$ gives:

$$\tau(x_3) = \rho \cdot g \cdot \frac{\partial a}{\partial x_1} \cdot (a - x_3) = \rho \cdot \nu_t \cdot \frac{\partial U_1}{\partial x_3} \tag{2-22}$$

The shearstress decreases linearly from bottom to watersurface.

The same mean flowvelocity profile, described with equation (2-20), can be derived when an integral scale is chosen which holds aswell for case 3:

$$\ell = \kappa \cdot x_3 \cdot \sqrt{1 - x_3/a}$$

In case 3, $x_3 \ll a$, so $\ell \cong \kappa \cdot x_3$. Near the watersurface the mixing length decreases, at $x_3=a$; $\ell = 0$.

It is profitable to describe the mean flowvelocity profile from bottom to watersurface with the same equation, but instead of the logarithmic flowvelocity profile (2-20) also a power flowvelocity profile could have been chosen for the region $x_3^+ > 30$ and x_3 far from the wall.

Finally the flowvelocity profiles in the different regions are sketched in figure 2.4.

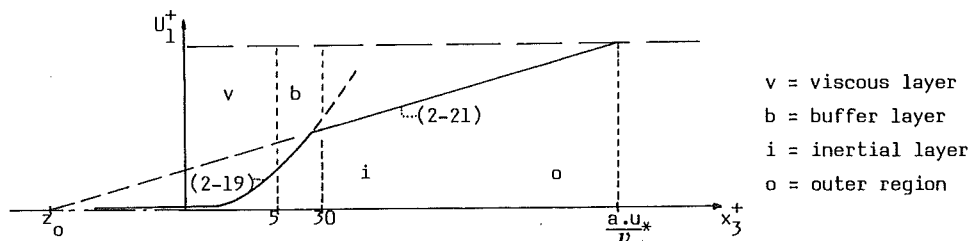


Figure 2.4: Flowvelocity profile in a uniform stationary channel flow.

2.2.4 Non-uniform channel flow

When the flow is stationary, but the flowvelocity is increasing in downstream direction, convection, the mean flowvelocity profile and shearstress profile are influenced, with respect to the profiles described in sub-section 2.2.3.

In this sub-section the influence of convection on the bottomshearstress is derived and the local change of the mean flowvelocity profile is treated.

Furthermore the development of the boundary layer in downstream direction is treated.

Bottomshearstress

When a slight convection occurs in the whole flowfield, $\partial U_1 / \partial x_1 \neq 0$, then the convection term influences the bottomshearstress.

The convection influence will be regarded for a flow situation with horizontal bottom and a waterlevel with constant slope.

The conservation of momentum equation in a two-dimensional stationary flow is given by equation (2-14):

$$U_1 \cdot \frac{\partial U_1}{\partial x_1} = -g \cdot \frac{\partial a}{\partial x_1} + \frac{1}{\rho} \cdot \frac{\partial \tau}{\partial x_3} \quad (2-14)$$

The term $g \cdot \partial a / \partial x_1$ produces the energy for the flow and this energy is distributed over the shearstress and the acceleration of the flow in x_1 -direction.

When $\partial U_1 / \partial x_1 = 0$, all energy goes to the shearstress. The shearstress passes the energy to turbulence. From the derivation in sub-section 2.2.3 it follows that for $\partial U_1 / \partial x_1 = 0$ the mean flowvelocity profile is logarithmic and the shearstress profile is linear over the waterdepth:

$$U_1 = u_* / \kappa \cdot \ln(x_3 / z_0) \quad (2-20)$$

$$\tau(x_3) = \rho \cdot g \cdot \frac{\partial a}{\partial x_1} \cdot (a - x_3) \quad (2-22)$$

$$\tau(0) = \rho \cdot u_*^2 \quad (2-23)$$

Equations (2-20) and (2-23) hold for the region near the wall, $x_3 \ll a$, and they hold with or without convection because they were derived without the aid of equation (2-14).

What the effect of convection is on equation (2-22) will be regarded next.

An overall influence of a slight convection can be derived by taking the depth-average of equation (2-14):

$$\overline{U_1 \cdot \frac{\partial U_1}{\partial x_1}} = -g \cdot \frac{\partial a}{\partial x_1} + \frac{1}{\rho} \cdot \frac{\partial \tau}{\partial x_3} \quad (2-24)$$

The convection term can be sufficient accurate enough approximated by: $\overline{U_1 \cdot \partial U_1 / \partial x_1} \approx \overline{U_1} \cdot \partial \overline{U_1} / \partial x_1$, see Verspuy (1981).

The conservation of mass equation reads: $\frac{\partial q}{\partial x_1} = \frac{\partial(\overline{U_1} \cdot a)}{\partial x_1} = a \frac{\partial \overline{U_1}}{\partial x_1} + \overline{U_1} \frac{\partial a}{\partial x_1} = 0$.

This leads to:

$$\overline{U_1 \cdot \frac{\partial U_1}{\partial x_1}} \approx - \frac{\overline{U_1}^2}{a} \frac{\partial a}{\partial x_1} \quad (2-25)$$

Substitution of equation (2-25) into (2-24) gives:

$$\frac{1}{\rho} \frac{\partial \tau}{\partial x_3} = \left(g - \frac{\overline{U_1}^2}{a} \right) \frac{\partial a}{\partial x_1} \quad (2-26)$$

The mean value of the shearstress can be calculated by: $\frac{1}{\rho a} \int_0^a \frac{\partial \tau}{\partial x_3} dx_3 = \frac{1}{\rho a} (\tau(a) - \tau(0)) = \frac{-1}{\rho a} \tau(0)$, when the shearstress at the surface is assumed to be zero.

Equation (2-26) results in:

$$\tau(0) = \rho \cdot g \cdot a \cdot \frac{\partial a}{\partial x_1} (1 - Fr^2) \quad (2-27)$$

with $Fr^2 = \overline{U_1}^2 / (g \cdot a)$; $a = a(x_1)$.

Equation (2-27) is the bottomshearstress with influence of convection, for slight convection the shearstress can be taken linearly from bottom to watersurface still.

Mean flowvelocity profile

The influence of convection on the flowvelocity profile based on empirical results is given in Tennekes (1977). A pressure-gradient parameter is defined as:

$$\Pi \equiv - \frac{\Delta}{u_*} \cdot \frac{\partial U_o}{\partial x_1} \tag{2-28}$$

with U_o as the flowvelocity in the outer layer just outside the boundary layer, in this case $U_o = U_1(a)$ is taken, the flowvelocity at the surface.

Also a normalized boundary layer thickness is defined as:

$$\Delta \equiv \frac{1}{u_*} \int (U_o - U_1) dx_3 \tag{2-29}$$

In which U_1 is the flowvelocity somewhere in the boundary layer.

A complete derivation is given in Tennekes (1977), here only the results are given.

The effect of the convection on the flowvelocity of the outer layer U_o results in an extra term depending on Π :

$$\frac{U_o}{u_*} = \frac{1}{\kappa} \ln \left(\frac{\Delta u_*}{\nu} \right) + A(\Pi) \tag{2-30}$$

U_o is the flowvelocity of the outer layer, for the flowvelocity U_1 in the boundary layer with influence a set of equations is given in Tennekes (1977). This is not treated here further.

Under certain conditions solutions of the set of equations can be found, in the expressions constants depending on Π occur. These constants for different values of Π have to be determined empirically. Clauser was the first who carried this out.

The result is that to the logarithmic flowvelocity profile a so-called wake-function must be added to get the effect of convection. In figure 2.5 some wake-functions depending on Π are sketched.

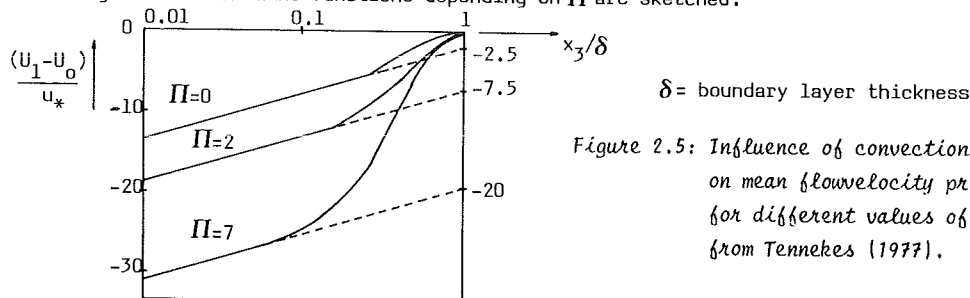


Figure 2.5: Influence of convection on mean flowvelocity profile for different values of Π , from Tennekes (1977).

An expression for the wake-function which gives reasonable results reads (see Tennekes, 1977):

$$W(x_3/a) = \frac{1}{2} \cdot (\sin \pi(x_3/a - \frac{1}{2}) + 1) \tag{2-31}$$

It must be mentioned that the stated above is valid for pipe-flow, which is symmetric with respect to the axis. When this is applied to a flow with free watersurface it should be done carefully.

Boundary layer development

The shearstress derived in sub-section 2.2.3 holds for fully developed boundary layers.

In practice a boundary layer starts at some point, for example the inflow of a flume, and increases in thickness downstream. Ofcourse it takes some distance to get a fully developed boundary layer stretching out from bottom to surface.

In Tennekes (1977) a derivation for the development of a boundary layer for $\Pi = 0$ is given.

Again only the results are given here.

The equations governing the boundary layer development read:

$$- \frac{x_3}{a} \cdot \frac{\partial (U_1 - U_o)}{\partial x_3} = - \frac{1}{u_*^2} \cdot \frac{\partial u_*^2}{\partial x_3} ; \frac{U_o}{u_*} \cdot \frac{\partial (\Delta u_*)}{\partial x_1} = 1 ; \frac{U_o}{u_*} = \frac{1}{\kappa} \cdot \ln \left(\frac{\Delta u_*}{\nu} \right) + A(o) \tag{2-32}$$

The growth of the boundary layer thickness is expressed in an angle which is approximated by:

$$\alpha_b \cong \frac{0.28}{U_o/u_* - 1/\kappa} \quad (2-33)$$

The angle is sketched in figure 2.6:

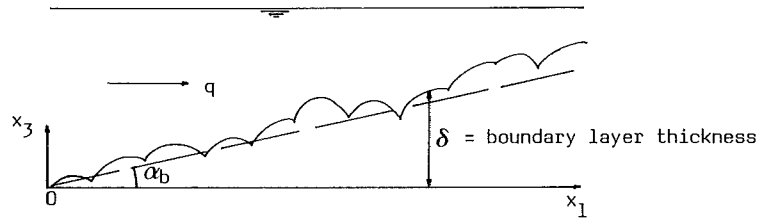


Figure 2.6: Downstream development of boundary layer.

The importance of the boundary layer development is the effect of it on the shearstress profile when the layer is not fully developed.

No simple expression for the shearsstress profile in a developing boundary layer is known.

In Tennekes (1977) a set of equations is given which is numerically soluted for the case $\Pi = 0$.

The set of equations reads:

$$\frac{x_3 \cdot u_*}{a} \cdot \frac{\partial(u_1 - u_o)}{\partial x_3} = \frac{\partial \overline{u_1 u_3}}{\partial x_3} \quad ; \quad \frac{u_o}{u_*} = \frac{1}{\kappa} \ln \left(\frac{\Delta u_*}{\nu} \right) + A(0) \quad (2-34)$$

A numerical solution is sketched in figure 2.7 for the Reynoldsshearstress:

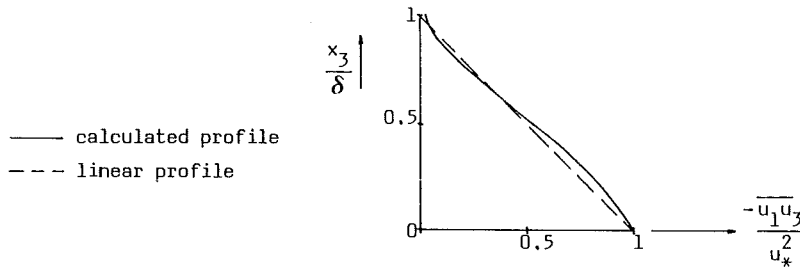


Figure 2.7: Influence boundary layer growth on Reynoldsshearstress for $\Pi = 0$, from Tennekes (1977).

It follows from figure 2.7 that $\overline{u_1 u_3}$ is not linear from bottom to surface.

It must be mentioned that the profile is calculated for a boundary layer with $\Pi = 0$ and an outer region which is thick compared to the boundary layer thickness.

So again applied to a boundary layer which is nearly as thick as the waterdepth should be done carefully.

For $\Pi \neq 0$ no profile for $\overline{u_1 u_3}$ is given, but for small deviations from $\Pi = 0$ the profile in figure 2.7 can be used for obtaining an indication.

2.2.5 The k-ε model

The description of turbulent quantities can be done in different ways.

The problem is to find suitable mathematical expressions for the turbulent viscosity, length scales, turbulent energy and energy dissipation.

Many different turbulence models have been developed already, an overview can be found in Rodi (1980) and Launder (1972).

In this sub-section only one turbulence model is treated, the two-equation k-ε model in which k is the turbulent kinetic energy and ε is the rate of turbulent kinetic energy dissipation.

This model is the basis for some computer programs, for example the ODYSSEE program of DHL and the PHOENICS program of Cham.

Calculations with the model give reasonable results for many tested flowtypes (Rodi, 1980) and constant factors in the model are verified for these flowtypes.

The conservation of momentum equation describes the flowfield and the turbulent viscosity in the equation is expressed in k and ε.

The k-ε model relates k and ε.

In this sub-section the k-ε model is treated and also some boundary conditions are given.

The k-ε model

The Navier-Stokes equation (2-6) for incompressible fluids and steady mean motion reads:

$$\frac{\partial U_i}{\partial t} + (U_j + u_j) \frac{\partial (U_i + u_i)}{\partial x_j} = -\frac{1}{\rho} \frac{\partial p}{\partial x_i} - \frac{1}{\rho} \frac{\partial p}{\partial x_i} + \nu \frac{\partial^2 (U_i + u_i)}{\partial x_j \partial x_j} + \bar{g}_i ; \begin{cases} i=1,2,3 \\ j=1,2,3 \end{cases} \quad (2-35)$$

Now add the conservation of mass equation times u_i ; ($u_i \cdot \partial u_j / \partial x_j$) to (2-35), subtract the average value of the resulting equation and multiply the new result by u_j .

Do the same for the u_j equation and multiply now by u_i .

Add these two resulting equations and after some manipulation the turbulent energy equation reads:

$$\frac{\partial \overline{u_i u_i}}{\partial t} + 2 \overline{u_i u_j} \frac{\partial U_i}{\partial x_j} + U_j \frac{\partial \overline{u_i u_i}}{\partial x_j} = -2 \cdot \frac{\partial}{\partial x_j} \left(\frac{p}{\rho} + \frac{u_i u_i}{2} \right) \cdot u_j + \nu \frac{\partial^2 \overline{u_i u_i}}{\partial x_j \partial x_j} - 2 \cdot \nu \cdot \frac{\partial u_i}{\partial x_j} \cdot \frac{\partial u_i}{\partial x_j} \quad (2-36)$$

A more detailed derivation is given in Hinze (1975).

To equation (2-36) also a buoyancy effect can be added, however, temperature effects are omitted here.

In the ODYSSEE program buoyancy effects are added, see Alfrink (1983).

The turbulent kinetic energy per unit mass is defined by :

$$k \equiv \frac{1}{2} \overline{(u_i u_i)} \quad (2-37)$$

Equation (2-36) can be rewritten with the aid of (2-37) in:

$$\frac{\partial k}{\partial t} + u_i \frac{\partial k}{\partial x_i} = -\frac{\partial}{\partial x_i} \left(\frac{p}{\rho} + \frac{u_i u_i}{2} \right) \cdot u_j - \overline{u_i u_j} \cdot \frac{\partial U_i}{\partial x_j} + \nu \frac{\partial^2 k}{\partial x_j \partial x_j} - \nu \frac{\partial u_i}{\partial x_j} \cdot \frac{\partial u_i}{\partial x_j} \quad (2-38)$$

This equation is an exact description of the turbulent kinetic energy derived from the Navier-Stokes equation and holds for high Reynoldnumbers.

To apply this equation it has to be modified, so the exact equation is approximated.

-The turbulent energy diffusion term: $\frac{\partial}{\partial x_i} \left(\frac{p}{\rho} + \frac{u_i u_i}{2} \right) \cdot u_j$, produces correlations $\overline{u_i u_i u_j}$ which are too complex to handle.

So this term is modelled by a 'diffusive expression': $\frac{\nu_t}{\sigma_k} \cdot \frac{\partial k}{\partial x_i}$, with σ_k as an empirical constant. See also Rodi (1980).

-The production of turbulent energy from the main stream is described by: $\overline{u_i u_j} \cdot \frac{\partial U_i}{\partial x_j}$.

The expression $\overline{u_i u_j}$ is a Reynoldsstress : $\frac{\tau_{ij}}{\rho} = -\overline{u_i u_j} = \rho \cdot \nu_t \cdot \left(\frac{\partial U_i}{\partial x_j} + \frac{\partial U_j}{\partial x_i} \right)$, according to Boussinesq. The complete term can be rewritten as:

$$\nu_t \cdot \left(\frac{\partial U_i}{\partial x_j} + \frac{\partial U_j}{\partial x_i} \right) \cdot \frac{\partial U_i}{\partial x_j}$$

- The term $\nu \cdot \frac{\partial^2 k}{\partial x_i \partial x_i}$ is the molecular diffusion of the turbulent kinetic energy, which is generally small for high Reynoldsnumbers.
- The term $\nu \cdot \overline{\partial u_i / \partial x_j \cdot \partial u_i / \partial x_j}$ is the turbulent kinetic energy dissipation ϵ .

The energy from the main stream is transported from large eddies via smaller eddies, to the smallest eddies with micro-length scales.

In these eddies the kinetic energy is dissipated in heat as a result of the molecular viscosity, see also sub-section 2.2.3.

For the dissipation an expression is given which is based on empirical grounds (Rodi, 1980).

Different expressions for the dissipation ϵ as function of k and ℓ , the integral length scale, are known, however, a general accepted convenient expression for the dissipation reads:

$$\epsilon = c_D \cdot \frac{k^{3/2}}{\ell} \quad (2-39)$$

In which c_D is an empirical constant. The dimension of ϵ is rate of kinetic energy dissipation per unit mass, which is not an exclusive result of physical laws, but much more a 'desired coincidence'.

The unknown integral scale demands an extra equation, this is the so-called closure-problem.

Without the expression for ϵ by equation (2-39) a general equation for ϵ can be derived from the Navier-Stokes equation. This derivation is complex and will not be given here.

To be mentioned has that the dissipation equation contains very troublesome correlations.

For reasons of convenience, however, the exact equation for ϵ is rewritten in a form which agrees with the equation for k .

Whether this is admissible from a physical point of view is not answered here, but the main reason to adapt the ϵ -equation lies in the field of solution techniques for partial differential equations.

Again a closure-problem occurs in the ϵ -equation, this is solved in this model by defining a source term (kind of dissipation) which solely depends on k and ϵ .

The final unknown variable is the turbulent viscosity.

Generally it is stated that $\nu_t \sim k^{1/2} \cdot \ell$ (Rodi, 1980) together with equation (2-39) the equation for the turbulent viscosity reads:

$$\nu_t = c_\mu \cdot \frac{k^2}{\epsilon} \quad (2-40)$$

In which c_μ is an empirical constant.

Now the complete k - ϵ equations are given (see also Rodi, 1980):

$$\underbrace{\frac{\partial k}{\partial t}}_R + \underbrace{U_i \frac{\partial k}{\partial x_i}}_C = \underbrace{\frac{\partial}{\partial x_i} \left[\frac{\nu_t}{\sigma_k} \cdot \frac{\partial k}{\partial x_i} \right]}_D + \underbrace{\nu_t \cdot \left(\frac{\partial U_i}{\partial x_j} + \frac{\partial U_j}{\partial x_i} \right) \cdot \frac{\partial U_i}{\partial x_j}}_P - \underbrace{\epsilon}_{\text{diss}} \quad (2-41)$$

$$\underbrace{\frac{\partial \epsilon}{\partial t}}_R + \underbrace{U_i \frac{\partial \epsilon}{\partial x_i}}_C = \underbrace{\frac{\partial}{\partial x_i} \left[\frac{\nu_t}{\sigma_\epsilon} \cdot \frac{\partial \epsilon}{\partial x_i} \right]}_D + \underbrace{c_{1\epsilon} \frac{\epsilon}{k} \cdot \nu_t \cdot \left(\frac{\partial U_i}{\partial x_j} + \frac{\partial U_j}{\partial x_i} \right) \cdot \frac{\partial U_i}{\partial x_j}}_P - \underbrace{c_{2\epsilon} \frac{\epsilon^2}{k}}_{\text{diss}} \quad (2-42)$$

The empirical constants with generally accepted values are (Rodi, 1980):

$$\sigma_k = 1 \quad ; \quad \sigma_\epsilon = 1.3 \quad ; \quad c_{1\epsilon} = 1.44 \quad ; \quad c_{2\epsilon} = 1.92 \quad ; \quad c_\mu = 0.09$$

- The k - ϵ model holds for:
- isotropic turbulence,
 - high Reynoldsnumbers,
 - regions outside the viscous layer and near the wall.

The terms in the equations (2-41) and (2-42) have the following physical meaning:

- R : rate of change of turbulent energy in time, or rate of change of dissipation in time
- C : convection of turbulent kinetic energy
- D : diffusion of kinetic turbulent energy
- P : production of kinetic turbulent energy (energy flow from main stream to turbulence)
- diss : dissipation of kinetic turbulent energy due to molecular viscosity.

Remark: the term $\nu \cdot \nabla^2 k / (\partial x_j \cdot \partial x_j)$ is generally small compared to the term D in equation (2-41), but for completeness this term is added to D, so ν_t is defined as $\nu_t = \nu_{\text{turbulent}} + \nu_{\text{moleculair}}$.

Boundary conditions

For the numerical solution of (2-41) and (2-42) together with (2-4), (2-8) and (2-9), boundary conditions are required.

Conditions for some different types of boundaries are given below (see also Rodi, 1980).

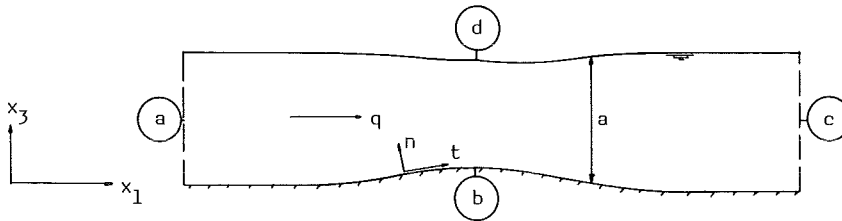


Figure 2.8: Definition of boundaries.

boundary condition a:

On this boundary the profiles of U_1 , U_3 , p , k and ϵ must be known.

boundary condition b:

For a solid wall, the no-slip condition holds, $U_1 = 0$ and k and ϵ are finite.

A large number of grid points near the wall is required to compute the steep flowvelocity and energy dissipation profiles accurate enough.

The viscous layer can not be calculated by the $k-\epsilon$ model, so the first grid-point must be taken at some distance from the wall. The law of the wall is applied in the region from wall to first grid-point.

For large Reynoldsnumbers the viscous and buffer layer are very thin with respect to the total boundary layer thickness, so the viscous and buffer layer can be omitted.

A logarithmic flowvelocity profile is used in the inertial layer which reads:

$$U_t = \frac{u_*}{\kappa} \cdot \ln (E \cdot x_3^+) \tag{2-43}$$

this equation holds for $30 < x_3^+ < 100$ (Rodi, 1980), with $E = 9$ for hydraulic smooth walls.

For hydraulic rough walls equation (2-20) holds.

The flowvelocity normal to the wall is $U_n = u_n = 0$.

In the region $30 < x_3^+ < 100$ the pressure is nearly constant and not changing in the direction along the wall $\partial p / \partial x_1 = 0$, otherwise accelerations in the inertial layer will occur.

Furthermore the convection and diffusion of $\overline{u_i u_j}$ are neglectible so local equilibrium prevails and the production of turbulent energy equals the dissipation $P = \epsilon$ (Tennekes, 1977).

This leads to the fact that the shearstress equals the wall stress and so the boundary condition for k reads:

$$k = \frac{u_*^2}{\sqrt{c} \mu} \tag{2-44}$$

With $P = \epsilon = u_*^2 \cdot \frac{\partial U_1}{\partial x_3}$ and equation (2-43) the boundary condition for ϵ reads:

$$\epsilon = \frac{u_*^3}{\kappa \cdot x_3} \tag{2-45}$$

Equations (2-44) and (2.45) hold for smooth and rough walls, the roughness enters in the equations via u_* .

boundary condition c:

Through this boundary the fluid leaves the area and generally the so-called weak boundary conditions are used here:

$$\frac{\partial^2 u_1}{\partial x_1^2} = 0 ; \frac{\partial^2 u_3}{\partial x_3^2} = 0 ; \frac{\partial^2 p_2}{\partial x_1^2} = 0 ; \frac{\partial^2 k_2}{\partial x_1^2} = 0 ; \frac{\partial^2 \epsilon_2}{\partial x_1^2} = 0$$

boundary condition d:

This boundary is free and generally a rigid-lid approximation is applied.

The conditions for the velocities read:

$$\frac{\partial u_1}{\partial x_1} = 0 \tag{2-46}$$

$$u_1 \cdot \frac{\partial a}{\partial x_1} - u_3 = 0 \tag{2-47}$$

See also Weugdenhill (1980)

The condition for the pressure reads: $p = p_0 = \text{constant}$.

The condition for k , with no shearforce acting on this boundary reads:

$$\frac{\partial k}{\partial x_3} = 0$$

otherwise:

$$k = \frac{u_*^2}{\sqrt{c_\mu}} [\text{surface}] \tag{Rodi, 1980}$$

The condition for ϵ is part of a discussion. Generally the condition $\partial \epsilon / \partial x_3 = 0$, but this leads to a finite mixing length ℓ near the watersurface.

Equation (2-39) reads: $\epsilon = c_D \cdot k^{3/2} / \ell$.

And the derivative from ϵ to x_3 reads: $\frac{\partial \epsilon}{\partial x_3} = \frac{3}{2} \cdot c_D \cdot k^{1/2} \cdot \frac{\partial k}{\partial x_3} - c_D \cdot \frac{k^{3/2}}{\ell^2} \cdot \frac{\partial \ell}{\partial x_3} = 0$.

The first term is zero because of $\partial k / \partial x_3 = 0$, the second term, however, is zero when $\partial \ell / \partial x_3 = 0$, or when $\ell = 0$ and $\partial \ell / \partial x_3 = 0$.

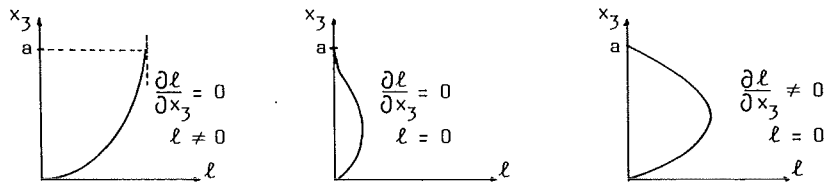


Figure 2.9: Shape of mixing length profile for different boundary conditions.

The demand for $\partial \ell / \partial x_3 = 0$ is not necessary, only $\ell = 0$ is required, so why should $\partial \epsilon / \partial x_3 = 0$?

Experiments lead to the conclusion that ℓ reduces near the surface.

Rodi (1980) gives a condition for ϵ which reads:

$$\epsilon = \frac{(k \cdot \sqrt{c_\mu})^{3/2}}{\kappa \cdot a \cdot c_S} \tag{2-48}$$

In which $c_S = 0,07$ is an empirical constant (Rodi, 1980).

2.2.6 Sidewall effects for channel flow

Generally walls in a flume affect the flowvelocity and shearstress profiles.

The rate of influence depends on the geometry of the flume and the flowconditions.

In this sub-section two methods are given to derive the influence of the sidewalls, the Einstein-method and a method described by Knight (1981).

The Einstein-method

The method can be used for steady flow in a channel, river or flume with arbitrary geometry of the cross-section. Here the geometry of the cross-section is assumed to be as sketched in figure 2.10.

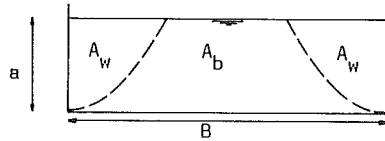


Figure 2.10: Definition of cross-section and areas.

According to the philosophy of the method, the areas A_w and A_b have the same mean flowvelocity and for each area the energy slope i_E is equal.

Via the Chézy formula for the mean flowvelocity, $\bar{U}_1 = C \cdot \sqrt{R \cdot i_E}$, this assumption yields:

$$\frac{1}{C_w^2 \cdot R_w} = \frac{1}{C_b^2 \cdot R_b} \tag{2-49}$$

With C_w as wall-roughness factor, C_b as bottom-roughness factor, $R_w = \frac{A_w}{a}$ and $R_b = \frac{A_b}{B}$.

The roughness according to White-Colebrook reads:

$$C_w = 18 \cdot \log \left(\frac{12 \cdot R_w}{k_w + \delta_w / 3,5} \right) \quad \text{and} \quad C_b = 18 \cdot \log \left(\frac{12 \cdot R_b}{k_b + \delta_b / 3,5} \right) \tag{2-50}$$

With k_w as wall-roughness and k_b as bottom-roughness. The thickness of the viscous layer reads:

$$\delta_w = \frac{11,6 \cdot \nu}{\sqrt{g \cdot R_w \cdot i_E}} \quad \text{and} \quad \delta_b = \frac{11,6 \cdot \nu}{\sqrt{g \cdot R_b \cdot i_E}} \tag{2-51}$$

An expression for R_b can be derived via, $A = 2 \cdot A_w + A_b = a \cdot B$, and reads: $R_b = a \cdot \left(1 - \frac{2 \cdot R_w}{B}\right)$

With these expressions R_w and R_b can be calculated which satisfy equation (2-49).

The Knight-method

This method is based on experiments carried out in a straight flume with a number of different values for wall and bottom roughness and waterdepth, the results are described by Knight (1981).

The following expressions are defined by Knight:

$$\bar{\tau}_w / (\rho \cdot g \cdot a \cdot i_E) = \%SF_w \cdot B / (2 \cdot a \cdot 100) ; \bar{\tau}_b / (\rho \cdot g \cdot a \cdot i_E) = \%SF_b / 100 ; \bar{\tau}_o = 2 \cdot a \cdot \bar{\tau}_w + B \cdot \bar{\tau}_b \tag{2-52}$$

with: $\bar{\tau}_w$ as mean wall shearstress, $\bar{\tau}_b$ as mean bottom shearstress, $\bar{\tau}_o$ as overall mean shearsstress, $\%SF_w$ as percentage wall shearstress, $\%SF_b$ as percentage bottom shearstress.

The empirical relations of wall and bottom shearstress are given in figure 2.11.

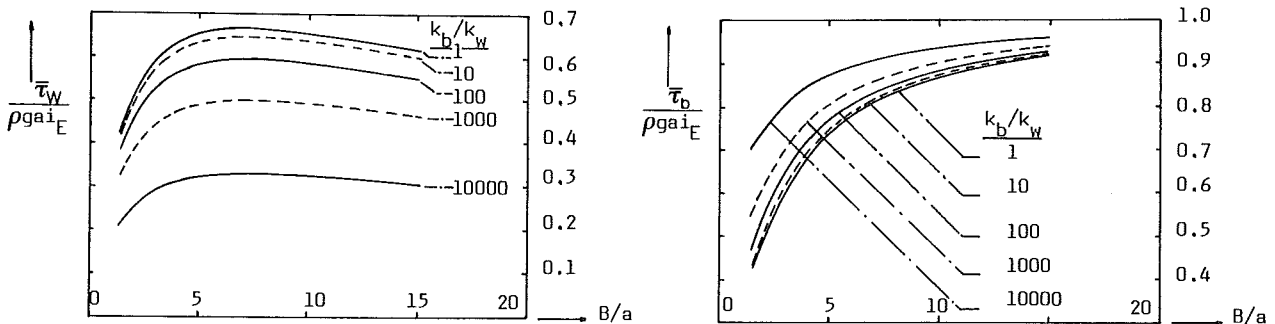


Figure 2.11: Influence sidewalls on shearstress, from Knight (1981).

2.3 Sediment movement

2.3.1 General

The conservation of mass equation for sediment holds generally. A general conservation of momentum equation, however, is difficult to derive for sediment.

Parameters like the mean flow velocity, turbulent quantities, sediment grain size and shape strongly influence the motion of sediment particles.

Empirical conservation of momentum equations have been derived for different types of sediment.

Many of these equations hold for average flow conditions and average sediment qualities, like the Mayer-Peter-Müller, Engelund-Hansen and Ackers&White equations.

In this section the sediment movement is regarded locally along a dune.

For this purpose two simple transport equations are used.

The first is an expression in which the sediment transport depends strongly on the flow velocity, $S = f(U_1)$.

The second expression reads, $S = f(U_1, x_1)$ in which the sediment transport depends strongly on the flow velocity and the position along the dune.

2.3.2 Conservation of mass equation

The derivation is carried out in the x_1, x_2, x_3 -orthogonal coordinate system, with instantaneous flow velocities $u_i = u_i(x_1, x_2, x_3, t)$ for $i=1, 2, 3$ and an instantaneous sediment concentration $\hat{c}(x_1, x_2, x_3, t)$.

A mass balance for a control volume (Eulerian frame) is set up as sketched in figure 2.12.

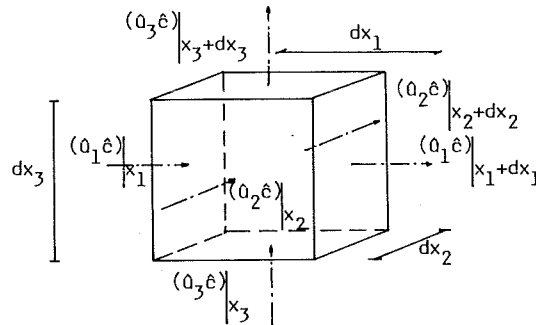


Figure 2.12: Definition of flow velocities and concentration in the control volume.

The sediment concentration in the control volume changes per unit time due to changes of the sediment flux through the control volume.

This yields the conservation of mass equation for sediment concentration:

$$\frac{\partial \hat{c}}{\partial t} + \frac{\partial u_1 \hat{c}}{\partial x_1} + \frac{\partial u_2 \hat{c}}{\partial x_2} + \frac{\partial u_3 \hat{c}}{\partial x_3} = 0 \quad (2-53)$$

The derivation is carried out for the two-dimensional x_1, x_3 -coordinate system in a vertical plane, so equation (2-53) reduces to:

$$\frac{\partial \hat{c}}{\partial t} + \frac{\partial u_1 \hat{c}}{\partial x_1} + \frac{\partial u_3 \hat{c}}{\partial x_3} = 0 \quad (2-54)$$

The instantaneous flow velocities and concentration will be separated in mean and fluctuating components, Reynolds decomposition: $u_1 = U_1 + u_1$; $u_2 = U_2 + u_2$; $u_3 = U_3 + u_3$; $\hat{c} = C + c$, with the same treatment as given in sub-section 2.2.2. this results for example for the concentration in: $\overline{\hat{c}} = C$ and $\overline{c} = 0$, when the concentration is averaged over a period T .

After decomposition and averaging over a period T equation (2-54) reads:

$$\frac{\partial C}{\partial t} + \frac{\partial U_1 C}{\partial x_1} + \frac{\partial U_3 C}{\partial x_3} + \frac{\partial \overline{u_1 c}}{\partial x_1} + \frac{\partial \overline{u_3 c}}{\partial x_3} = 0 \quad (2-55)$$

Now the flowfield over the dune and the dune itself will be regarded more detailed in order to rewrite equation (2-55) in a more convenient form.

the flowfield above the movable bed is sketched in figure 2.13, dune on a conveyor belt:

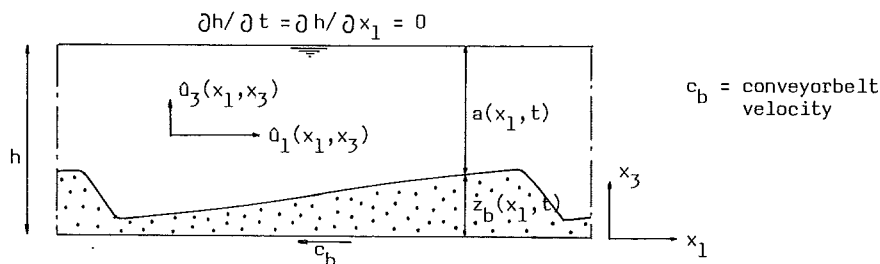


Figure 2.13: Definition of the flowfield.

The dune is moved upstream with a constant velocity c_b which is equal and reverse to the dune propagation velocity, so the dune does not move with respect to the x_1, x_3 -coordinate system.

Due to acceleration of the flow above the dune, the watersurface will not be horizontal, however, deviations from a horizontal plane will be small.

In the derivation a rigid-lid assumption will be made, $\partial h / \partial x_1 = 0$. The watersurface does not change with time, $\partial h / \partial t = 0$.

In the x_3 -direction three regions can be distinguished as sketched in figure 2.14.

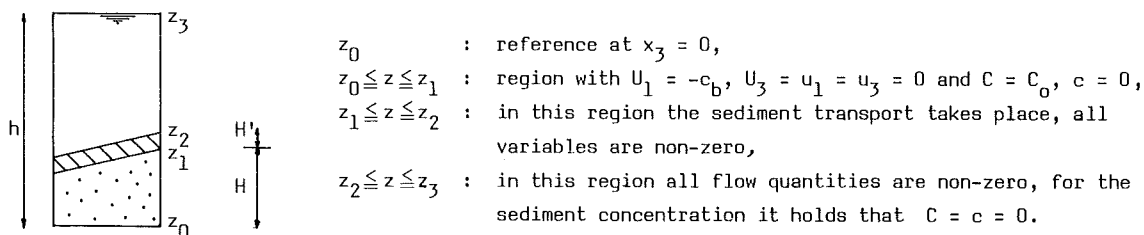


Figure 2.14: Definition of regions.

Before working out equation (2-55) an important mathematical relation is given (Abramowitz, 1972):

$$\int \frac{\partial f(x, z)}{\partial x} dz = \frac{\partial}{\partial x} \int f(x, z) dz - \frac{\partial b}{\partial x} f(x, b(x)) + \frac{\partial a}{\partial x} f(x, a(x)) \quad (2-56)$$

Equation (2-55) will be integrated along the x_3 -axis and the terms of the equation will be treated separately, with the aid of equation (2-56).

The term $\frac{\partial C}{\partial t}$:

$$\int_{z_0}^{z_3} \frac{\partial C}{\partial t} dx_3 = \frac{\partial}{\partial t} \int_{z_0}^{z_3} C dx_3 - C(x_1, z_3) \frac{\partial z_3}{\partial t} + C(x_1, z_0) \frac{\partial z_0}{\partial t}$$

The concentration at the surface $C(x_1, z_3) = 0$ and the terms $\partial z_3 / \partial t = \partial z_0 / \partial t = 0$, so the remaining expression reads:

$$\frac{\partial}{\partial t} [C_0 \cdot H + C \cdot H']$$

It is assumed that $C < C_0$ and $H' \ll H$, the transport layer is very thin with respect to the total duneheight, so finally for this term the result is:

$$C_0 \cdot \frac{\partial H}{\partial t}$$

The term $\frac{\partial U_1 C}{\partial x_1}$:

$$\int_{z_0}^{z_3} \frac{\partial U_1 C}{\partial x_1} dx_3 = \frac{\partial}{\partial x_1} \int_{z_0}^{z_3} U_1 C dx_3 - U_1 C(x_1, z_3) \frac{\partial z_3}{\partial x_1} + U_1 C(x_1, z_0) \frac{\partial z_0}{\partial x_1}$$

The terms $\partial z_3 / \partial x_1 = \partial z_0 / \partial x_1 = 0$ so the remaining expression reads:

$$\frac{\partial}{\partial x_1} [-c_b \cdot C_0 \cdot H + \int_{z_1}^{z_2} U_1 C dx_3]$$

The term $\int U_1 C dx_3$ describes the mean sediment transport in the transport layer, this term is estimated by $S \cdot C_0$, in which S is the mean transport per unit time and mass, including pores.

So finally this term can be approximated by:

$$-c_b \cdot c_o \frac{\partial H}{\partial x_1} + c_o \frac{\partial S}{\partial x_1}$$

The term $\frac{\partial u_3 c}{\partial x_3}$:

$$\int_{z_0}^{z_3} \frac{\partial u_3 c}{\partial x_3} dx_3 = \int_{z_0}^{z_3} \partial u_3 c = 0$$

The term $\frac{\partial \overline{u_1 c}}{\partial x_1}$:

$$\int_{z_0}^{z_3} \frac{\partial \overline{u_1 c}}{\partial x_1} dx_3 = \frac{\partial}{\partial x_1} \int_{z_0}^{z_3} \overline{u_1 c} dx_3 - \overline{u_1 c(x_1, z_3)} \frac{\partial z_3}{\partial x_1} + \overline{u_1 c(x_1, z_0)} \frac{\partial z_0}{\partial x_1}$$

with $c(x_1, z_3) = 0$ and $\partial z_3 / \partial x_1 = \partial z_0 / \partial x_1 = 0$, the remaining expression reads:

$$\frac{\partial}{\partial x_1} \left[\int_{z_1}^{z_2} \overline{u_1 c} dx_3 \right]$$

The term $\int \overline{u_1 c} dx_3$ describes the fluctuation of the sediment transport in the transport layer, this term is estimated by $s \cdot c_o$, in which s is the fluctuation of the sediment transport with $\overline{s} = 0$, when is averaged over a period T .

So finally this term can be approximated by:

$$\frac{\partial s c_o}{\partial x_1}$$

The term $\frac{\partial \overline{u_3 c}}{\partial x_3}$:

$$\int_{z_0}^{z_3} \frac{\partial \overline{u_3 c}}{\partial x_3} dx_3 = \int_{z_0}^{z_3} \partial \overline{u_3 c} = 0$$

When the above derived expressions for the different terms of equation (2-56) are substituted, when (2-56) is integrated over the x_3 -axis and the instantaneous sediment transport is defined as $\underline{s} = S + s$, and the local dune height $H = z_b$, then the conservation of mass equation reads:

$$\frac{\partial \underline{s}}{\partial x_1} + \frac{\partial z_b}{\partial t} - c_b \cdot \frac{\partial z_b}{\partial x_1} = 0 \tag{2-57}$$

The first term expresses the change of the sediment transport in time, the second term expresses the change of dune height in time and the third term expresses the influence of the conveyor belt velocity.

2.3.3 A simple transport equation

The sediment transport rate strongly depends on the mean flow velocity. so the most simple conservation of momentum equation reads (see also de Vries, 1981):

$$S = f(U_1) \tag{2-58}$$

This equation is used to express the transport term in equation (2-57).

It holds that:

- $h = a(x_1, t) + z_b(x_1, t) = a + z_b = \text{constant}$
- $q = U_1(x_1, x_3) \cdot a(x_1, t) = U_1 \cdot a = \text{constant (specific discharge)}$
- $\frac{\partial S}{\partial x_1} = \frac{\partial f}{\partial U_1} \cdot \frac{\partial U_1}{\partial x_1}$

After substitution of:

$$\frac{\partial S}{\partial x_1} = \frac{\partial f}{\partial U_1} \cdot \left(\frac{-q}{a^2}\right) \cdot \frac{\partial a}{\partial x_1} \tag{2-59}$$

$$\frac{\partial z_b}{\partial x_1} = - \frac{\partial a}{\partial x_1} \tag{2-60}$$

$$\frac{\partial z_b}{\partial t} = - \frac{\partial a}{\partial t} \tag{2-61}$$

in equation (2-57) and averaging over a period T , the result is:

$$\frac{\partial a}{\partial t} + K \cdot \frac{\partial a}{\partial x_1} = 0 \tag{2-62}$$

with:

$$K = K(a) = \frac{\partial f}{\partial U_1} \cdot \frac{q}{a^2} - c_b \tag{2-63}$$

Equation (2-62) is a non-linear hyperbolic partial differential equation with a celerity $K(a)$, this equation is based on the rigid lid approximation.

Now a more specific model is chosen for the conservation of momentum equation (2-58):

$$S = m.(U_1 - U_0)^n \tag{2-64}$$

In which m and n are constants and U_0 denotes the critical flowvelocity for sediment transport. The expression for K after using equation (2-64) reads:

$$K = \frac{m \cdot n \cdot q}{a^2} \cdot (U_1 - U_0)^{n-1} - c_b \tag{2-65}$$

Linearization of K is not required because it is essential that K depends on U_1 and a , but K will be regarded in a different way.

The celerity K is the local propagation velocity of the dune at an arbitrary coordinate (x_1, z_b) .

The total dune propagates with a certain velocity and is moved upstream with velocity c_b .

During the experiments it is required that the position and height of the dune do not change in time, so $\partial a / \partial t = 0$, and because $\partial a / \partial x_1 \neq 0$ it follows that K must be zero for all x_1 .

From equation (2-65) it can be seen that with constant m, n, q, c_b and U_0 this demand is impossible, because U_1 and a change with x_1 .

So K is non-zero along the x_1 -axis except for one point where: $\frac{m \cdot n \cdot q}{a^2} \cdot (U_1 - U_0)^{n-1} = c_b$.

The shape of the dune according to equation (2-64) and (2-65) changes to a horizontal bed where in every coordinate $x_1, K = 0$. A so-called shockwave appears.

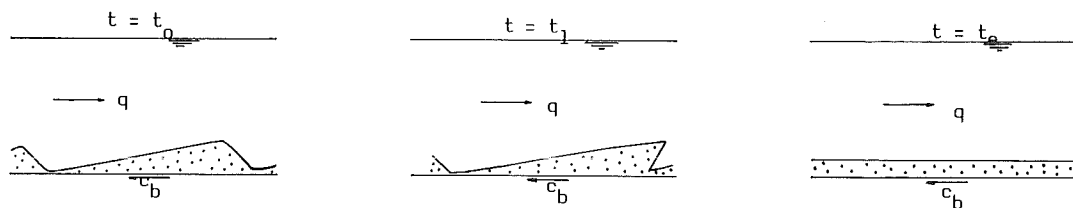


Figure 2.15: Development of a dune according to eq. (2-64) and (2-65).

Another way to look at K is to define a local velocity $c_b = c_b(x_1)$ so,

$$K = \frac{m \cdot n \cdot q}{a^2} \cdot (U_1 - U_0)^{n-1} - \frac{m \cdot n \cdot q}{a_e^2} \cdot (U_e - U_0)^{n-1} \tag{2-66}$$

In which m, n, q, U_0 are constants and U_1, a, U_e and a_e depend on x_1 .

The variables U_e and a_e hold in an arbitrary coordinate x_1 , where they denote the equilibrium flowvelocity and waterdepth. Once U_1 becomes U_e and a becomes a_e the dune propagation stops and $K = 0$.

So K is large as U_1 and a differ much from U_e and a_e .

In this way a stable dune shape and position can exist after some time, but now the conveyor belt velocity c_b is a function of x_1 , so c_b is not constant along the dune.

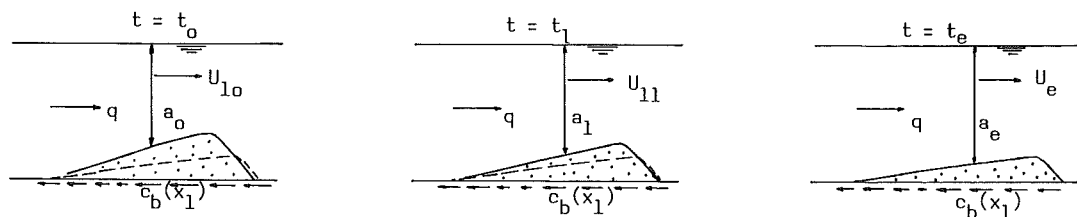


Figure 2.16: Development of a dune according to eq. (2-64) and (2-66).

Both expressions for K , (2-65) and (2-66), can not describe the dune propagation sufficiently with respect to the demands: a constant dune propagation velocity and dune height.

A more detailed description for S must be chosen, because the expression (2-58) is in fact a relation set up for the overall transport.

2.3.4 A comprehensive transport equation

The description of the sediment transport by equation (2-58) is not sufficient as pointed out in the previous sub-section.

So the relation is extended by dependence of S of the x_1 -coordinate:

$$S = f(U_1, x_1) \quad (2-67)$$

Reasons for making S dependent of x_1 are:

- A part of the mean flowvelocity U_1 is important for the transport, say: $p U_1$. In this way the boundary layer thickness above the dune can be taken into account.

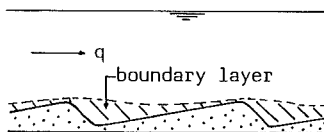


Figure 2.17: Boundary layer above a dune.

- The factor $p = p(x_1)$ is only a function of x_1 , not of U_1 and is independent of changes of the dune shape. The factor p belongs to one equilibrium dune shape. In this way the influence of position along the dune and the flowvelocity are separate.

So equation (2-67) can be written as:

$$S = f(U_1, p(x_1)) \quad (2-68)$$

Using equation (2-68) in equation (2-57) this results, after averaging over a period T, and with:

$$\frac{\partial S}{\partial x_1} = \frac{\partial S}{\partial U_1} \cdot \frac{\partial U_1}{\partial x_1} + \frac{\partial S}{\partial p} \cdot \frac{\partial p}{\partial x_1} ,$$

in:

$$\frac{\partial S}{\partial U_1} \cdot \frac{\partial U_1}{\partial x_1} + \frac{\partial z_b}{\partial t} - c_b \cdot \frac{\partial z_b}{\partial x_1} = - \frac{\partial S}{\partial p} \cdot \frac{\partial p}{\partial x_1} \quad (2-69)$$

The terms on the left hand side also occur in equation (2-57), the term on the right hand side, however, is added with respect to (2-57) and denotes the local influence on the transport.

A model is chosen for which S reads:

$$S = m \cdot (p \cdot U_1)^n \quad (2-70)$$

In which $p = p(x_1)$ includes the initiation of sediment transport, $S = 0$ for $p = 0$.

Remark: in the previous sub-section all variables were expressed in $a(x_1, t)$, in this sub-section, however, $z_b(x_1, t)$ is used.

In fact nothing changes because $h = a + z_b = \text{constant}$.

Equation (2-70) is used to determine the function p.

In a situation of equilibrium the shape of the dune does not change and it propagates with a constant velocity c_b , so $\partial z_b / \partial t = 0$ and equation (2-57) reduces to: $S_e = c_b \cdot z_b = m \cdot p^n \cdot U_1^n$.

With $q = U_1 \cdot a = U_1 \cdot (h - z_b)$ this yields:

$$z_b \cdot (h - z_b)^n = \frac{m \cdot q^n}{c_b} \cdot p^n ,$$

or:

$$p = (z_b / M)^{1/n} \cdot (h - z_b) \quad (2-71)$$

with $M = \frac{m \cdot q^n}{c_b}$, and z_{be} is the equilibrium dune height.

Equation (2-71) is zero for: $z_{be} = 0$ and for: $z_{be} = h$ (which is not relevant).

A maximum value for p appears for: $z_{be} = h / (n + 1)$.

Knowing the constants M and h and the shape of the dune, $z_{be}(x_1)$, the function p can be calculated for that particular shape.

The general shape of p for an arbitrary dune is sketched in figure 2.18.

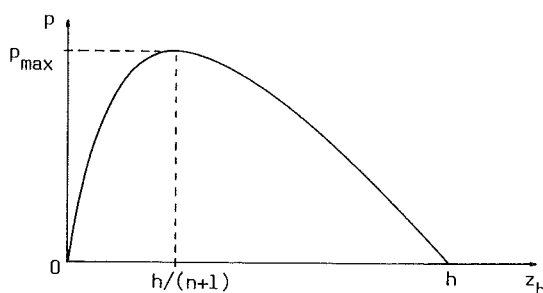


Figure 2.18: General shape of the function p.

The terms $\frac{\partial S}{\partial U_1} \cdot \frac{\partial U_1}{\partial x_1}$ and $\frac{\partial S}{\partial p} \cdot \frac{\partial p}{\partial x_1}$ in equation (2-69) will be treated separately and be expressed in z_b , z_{be} and derivatives.

The term $\frac{\partial S}{\partial U_1} \cdot \frac{\partial U_1}{\partial x_1}$: The derivative of equation (2-70) reads: $\frac{\partial S}{\partial U_1} = m \cdot n \cdot p^n \cdot U_1^{n-1}$.
 It holds that $q = U_1 \cdot (h - z_b)$, so: $\frac{\partial U_1}{\partial x_1} = \frac{q}{(h - z_b)^2} \cdot \frac{\partial z_b}{\partial x_1}$.

This results in:

$$\frac{\partial S}{\partial U_1} \cdot \frac{\partial U_1}{\partial x_1} = \frac{m \cdot n \cdot q \cdot p^n}{(h - z_b)^2} \cdot U_1^{n-1} \cdot \frac{\partial z_b}{\partial x_1} \quad (2-72)$$

The term $\frac{\partial S}{\partial p} \cdot \frac{\partial p}{\partial x_1}$: The derivative of equation (2-70) reads: $\frac{\partial S}{\partial p} = m \cdot n \cdot U_1^n \cdot p^{n-1}$.
 With equation (2-71) it follows:

$$\frac{\partial p}{\partial x_1} = \frac{(h - z_{be})}{n \cdot M} \cdot (z_{be}/M)^{\frac{1-n}{n}} \cdot \frac{\partial z_{be}}{\partial x_1} - (z_{be}/M)^{1/n} \cdot \frac{\partial z_{be}}{\partial x_1}$$

This results in:

$$K'' = \frac{\partial S}{\partial p} \cdot \frac{\partial p}{\partial x_1} = \left[\frac{m \cdot p^{n-1} \cdot U_1^n \cdot (h - z_{be})}{M} \cdot (z_{be}/M)^{\frac{1-n}{n}} - m \cdot n \cdot U_1^n \cdot p^{n-1} \cdot (z_{be}/M)^{1/n} \right] \frac{\partial z_{be}}{\partial x_1} \quad (2-73)$$

Equation (2-69) can now be rewritten in the same form as equation (2-62), and after some rearrangement:

$$\frac{\partial z_b}{\partial t} + K' \cdot \frac{\partial z_b}{\partial x_1} = K'' \quad (2-74)$$

with:

$$K' = \frac{m \cdot n \cdot q \cdot p^n \cdot U_1^{n-1}}{(h - z_b)^2} - c_b \quad (2-75)$$

and K'' is equation (2-73).

In the situation of equilibrium, $\frac{\partial z_b}{\partial t} = 0$, but K' is not zero. The term $K' \cdot \frac{\partial z_b}{\partial x_1}$ is compensated by the term K'' so an equilibrium situation can occur.

With this model no equilibrium shape of a dune can be predicted, the equilibrium shape must be known to determine the function p. But the model can be used to estimate the time needed for an arbitrary shape of the dune to reach the equilibrium shape.

This holds even when is started with a horizontal bed situation.

Some remarks can be made upon the function p.

According to Fredsøe (1982) the results of two interesting experiments are treated.

An experiment by Bradshaw and Wong in air, measurements of shearstresses above a triangular bottom step in a boundary layer.

Another experiment by Smith, in water, measurements of shearstresses above a triangular shape.

The set up of the experiments is sketched in figure 2.19, also some dimensions and flow conditions are given.

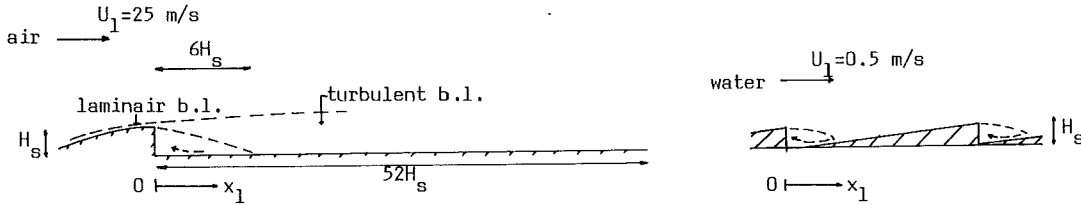


Figure 2.19: Definition of geometry in experiments by Bradshaw and Wong (left) and Smith (right).

The shearstress was measured just above the bottom and expressed in a dragforce coefficient:

$$c_f = \frac{\tau}{\frac{1}{2} \cdot \rho \cdot U_1^2}$$

The results are given in figure 2.20.



Figure 2.20: Results from experiments by Bradshaw and Wong (left) and Smith (right), from Fredsøe (1982).

In the experiment of Bradshaw and Wong the value of c_f remains nearly constant after $x_1/H_s = 16$.

In the experiment of Smith a local maximum value of c_f appears at $x_1/H_s = 16$, the increase of c_f after this coordinate is an effect of the shape of the bottom, on the convergence of the flow.

Comparing the triangular shape with a general shape of a dune, it appears that the dune is almost horizontal near the top, so no convergence of the flow occurs in that region and c_f does not increase after the local maximum.

The shape of c_f in both experiments, after adjusting for a general dune shape, is identical, as well as the shape of the function p from figure 2.18, when the part $z_b > \frac{1}{2}h$ of p is not taken into account.

After some rearrangement c_f and p can be compared. In general it holds that $S = f(\tau) = f(c_f \cdot \frac{1}{2} \cdot \rho \cdot U_1^2)$. So $S \sim (\sqrt{c_f} \cdot U_1)^2$.

From equation (2-70) it follows that $S \sim (\rho \cdot U_1)^n$. So for a constant value of n , it holds that $p \sim \sqrt{c_f}$.

One should be careful with the comparison of p and c_f , because $p = f(z_{be}(x_1))$ and $c_f = f(x_1/H_s)$, so p is an implicit function of x_1 and c_f is an explicit function of x_1 .

Furthermore c_f is related to a bottom step upstream and p is related to the shape of a dune.

Resulting it can be stated that both p and c_f have surprisingly identical shapes, both express the influence of the flow on the bottom shearstress and through this the sediment transport is influenced along the shape of the bottom.

3. Experiments

3.1 Introduction

In cases where no analytical solution of the hydrodynamic equations can be found, numerical solutions can be calculated and physical experiments can be carried out.

Experiments can be used to test the theoretical model and give insight in the physical phenomena.

For the simple flowconditions, as a part of the investigation, analytical solutions are found, which are compared with results of experiments.

For the flowconditions in case of a solitary dune, numerical solutions are calculated, which are compared with results of experiments.

In the solitary dune situation sediment particles are transported along the surface of the dune, this effect affects the flowfield near the surface of the dune.

The numerical solution does not include moving sediment particles, so comparing both cases should be done with care.

In this chapter the flowconditions, the measuring method and the processing of data are described.

3.2 Experimental facilities

The flume:

The experiments are carried out in a straight flume, with a total length of 24.0 m and a cross-section of $0.5 \times 0.5 \text{ m}^2$.

The bottom of the flume is horizontal and consists of very smooth concrete elements, with a length of 1.5 m. Between the elements there is a 0.5 cm wide joint filled with silicon.

The walls of the flume are vertical and consists of 1.5 m long glass plates (thick 9 mm.) and the joint between the plates is 0.5 cm wide and filled with silicon.

The joints affect the roughness of bottom and walls.

Water is withdrawn from a reservoir in which the waterlevel is constant and led through a pipe with a diameter of 0.15 m at the inflow of the flume.

The water flows into the flume via a stilling basin and damping is brought into the flume at the inflow to reduce translatory waves travelling up and down the flume.

The discharge is measured by an orifice in the pipe.

At the end of the flume a weir controls the waterdepth and the slope of the watersurface in the flume.

The complete installation of the flume is sketched in figure 3.1, in which the coordinate system is given as well. Just after the inflow $x_1 = 0$, in the flume axis $x_2 = 0$ and $x_3 = 0$ at the bottom of the flume.

The measuring section is situated from $x_1 = 15.0$ to $x_1 = 17.0$ m.

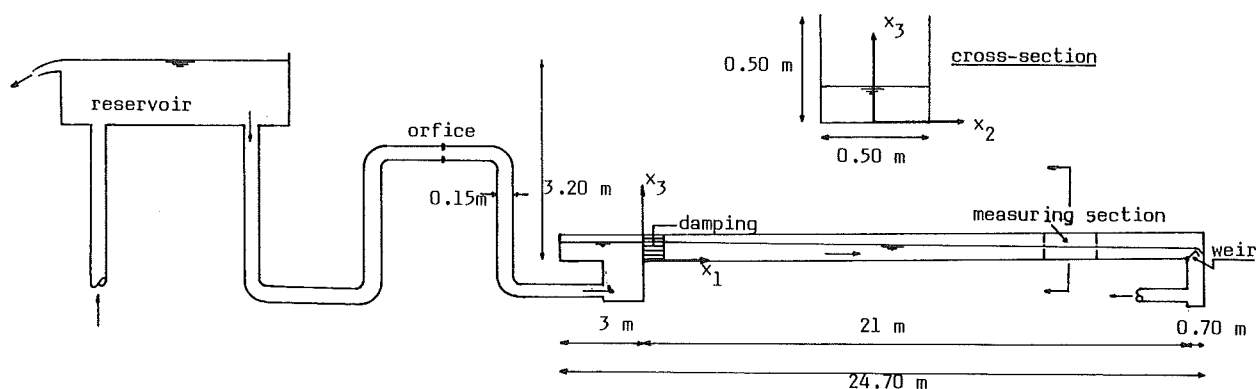


Figure 3.1: The flume.

Measuring the instantaneous flowvelocity:

A Laser Doppler Anemometer (LDA), heterodyne system, is used to measure the instantaneous flowvelocity. The working principle of the LDA is described in appendix A.

A great advantage of the LDA is that the flow is not affected by any measuring device and measurements carried out close to the surface of the solitary dune, where the transport takes place, do not disturb the sediment transport.

In the water a measuring volume is created through intersecting laser beams.

The measuring volume is adjustable and can be made smaller than 1 mm^3 . In the measuring volume the flowvelocity is measured, small particles in the water are illuminated by the laser beams and reflect the light.

Due to the velocity of the particles a doppler shift occurs in the frequency of the reflected light, compared with the frequency of the light leaving the laser.

The frequency shift is a direct measure for the velocity of the particles and so a measure for the flow-velocity of the water, if the particles move in the same way as the water does.

The frequency shift is transferred by a tracker into a voltage which can be translated into a flowvelocity.

The tracker can follow, within a certain range, the fluctuations of the flowvelocity, so the instantaneous flowvelocity of the water is measured.

The instantaneous flowvelocity is transferred from analog to digital information and stored on tape.

The stored data can be processed by a computer.

The instantaneous flowvelocity can be decomposed into a mean flowvelocity and a fluctuating flowvelocity, Reynoldsdecomposition.

Turbulent quantities (energy, shearstress) can be calculated now, see sub-section 2.1.2.

With the LDA system used in the experiments two flowvelocity components in the measuring volume can be measured at the same time.

These components lie in a vertical plane parallel to the flume axis, the plane in which the main flow-directions lie.

After the tracker an analog filter is used to reduce noise and the frequency peak of 48.5 Hz. generated by the rotating grating (see appendix A).

The complete LDA system used in the experiments can be seen on pictures at the end of appendix A.

The measuring frame:

The LDA equipment is placed on a frame which is placed over the flume.

The measuring frame consists of a bridge with plateaus on both sides of the flume.

On one plateau the laser and optics are placed on the other plateau the photodetectors. The frame can be moved in the x_1 - and x_3 -direction.

The optics of the LDA are placed on a special base plate on the plateau. The base plate can be moved in the x_2 -direction.

The measuring frame is sketched in figure 3.2.

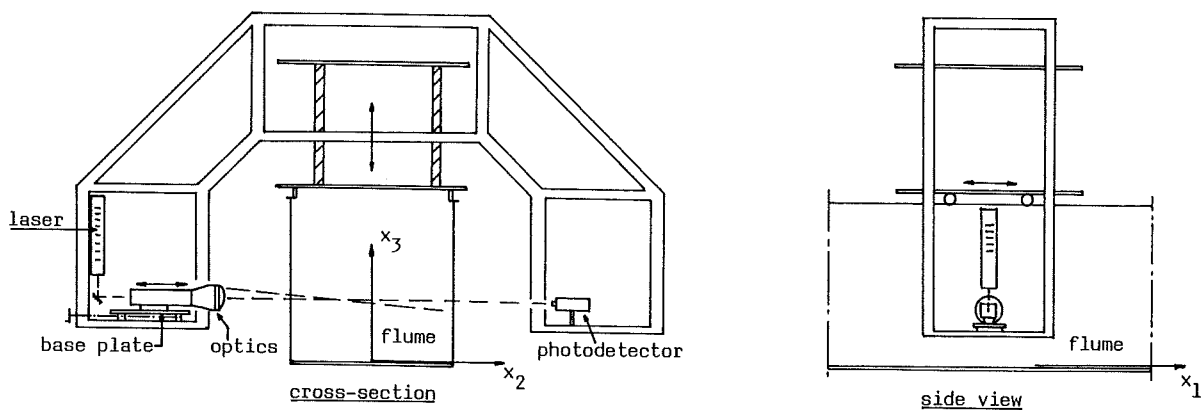


Figure 3.2: The measuring frame.

The coordinates of the measuring volume can be measured with the following accuracies:

- x_1 -direction : 0.5 mm.
- x_2 -direction : 1.0 mm.
- x_3 -direction : 0.5 mm.

The x_1 -coordinate is related to the flume, the x_3 -coordinate is related to the flume bottom. The x_2 -coordinate is related to the position of a thin perspex plate which is placed vertically into the flume.

The perspex plate is placed in the right x_2 -coordinate and then the optics on the base plate is moved in the x_2 -direction until the measuring volume is placed in the perspex plate.

The doppler bursts are maximal, because particles in the perspex remain at their position and the signal remains maximal.

Furthermore the velocity of the particles in the perspex is zero, so the offset voltage in the tracker can be adjusted to zero.

A photo of the measuring frame can be seen at the end of appendix A.

The conveyor:

In order to reduce the celerety of the dune to zero, a conveyor is built into the bottom of the flume.

The length of the conveyor is 2 m and its wide is 39.5 cm , the height is 6 cm.

The conveyor belt is driven by a spindle which is driven by an electric engine. The conveyor belt can be stretched.

The speed of the conveyor belt is continuously adjustable between 0.0 and 10.0 m/h.

The conveyor is fixed to the bottom by two vertical rods, which are placed near the walls of the flume, but influence the flow a little. The rods are placed, however, downstream the dune.

The belt to drive the spindle is placed near a wall but too influences the flow downstream the dune.

The conveyor is sketched in figure 3.3.

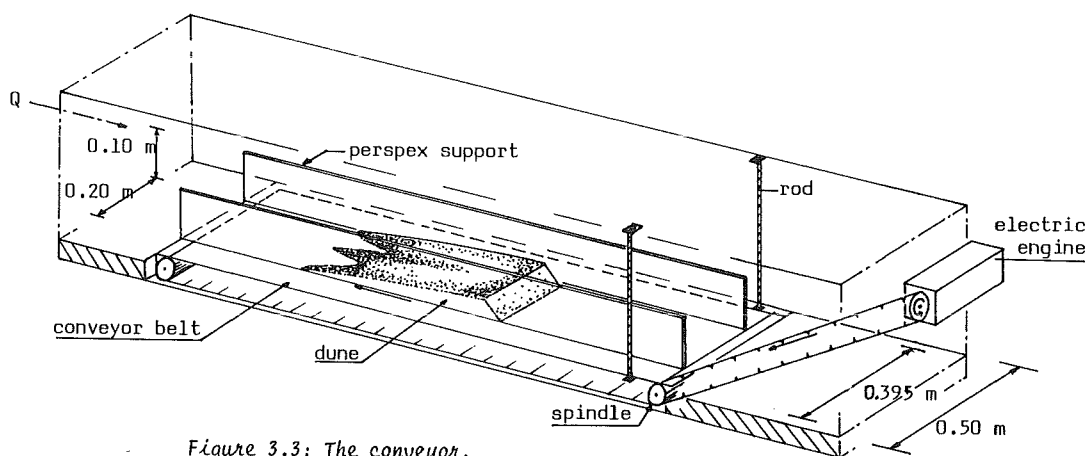


Figure 3.3: The conveyor.

To support the dune two perspex supports are placed on the conveyor, see figure 3.3. The supports are fixed to the walls of the flume and do not rest on the conveyor belt. There is a small space between support and belt, but no sediment particles can get inbetween.

The reasons for the perspex supports are (see also appendix B):

- near the wall of the flume the flowvelocity is too small to transport sediment, so only the centre part of the flume is used,
- a dune as wide as the flume, 0.50 m , is strongly three-dimensional of shape,
- no sediment particles may be lost in either direction.

3.3 Flowconditions

3.3.1 General

Measurements in two different flowsituations are carried out:

- a horizontal bed situation, set up to test the adapted LDA system,
- a solitary dune situation, for the investigation of the flow over a dune.

3.3.2 Horizontal bed situation

In this situation the bottom of the flume is horizontal and the width of the flume is 0.50 m.

The slope of the watersurface is: $\partial a / \partial x_1 = 0.992 \cdot 10^{-3} \pm 0.01 \cdot 10^{-3}$, except for a small region at the inflow of the flume and a small region at the outflow.

The discharge through the flume is: $Q = 24 \cdot 10^{-3} \pm 0.1 \cdot 10^{-3} \text{ m}^3/\text{s}$ and is constant.

The LDA-measurements are carried out at $x_1 = 16.0 \text{ m}$, in three verticals: $x_2 = 0.0$, $x_2 = 0.02 \text{ m}$ and $x_2 = -0.02 \text{ m}$. The waterdepth at these positions is: $a = 0.093 \pm 0.001 \text{ m}$ and is constant.

The mean flowvelocity over the cross-section at $x_1 = 16.0 \text{ m}$ is: $\bar{U}_1 = 0.516 \pm 0.008 \text{ m/s}$.

The mean temperature of the water during the measurements is: $T = 19.5 \pm 0.5 \text{ }^\circ\text{C}$, and the density of the water is: $\rho_w = 1000 \text{ kg/m}^3$.

So the kinematic viscosity of the water is: $\nu = 1.017 \cdot 10^{-6} \pm 0.012 \cdot 10^{-6} \text{ m}^2/\text{s}$.

The overall Reynoldsnumber is: $Re \cong 47000$.

The roughness of the glasswalls is: $k_w = 0.3 \cdot 10^{-3}$ to $0.4 \cdot 10^{-3} \text{ m}$ and the concrete bottom has a roughness: $k_b = 0.2 \cdot 10^{-3}$ to $0.5 \cdot 10^{-3} \text{ m}$.

3.3.3 Solitary dune situation

In the situation with the solitary dune the conveyor is situated between $x_1 = 15.0$ and $x_1 = 17.0 \text{ m}$.

Upstream and downstream the conveyor the bottom of the flume is horizontal.

The slope of the watersurface is: $\partial a / \partial x_1 = 0.475 \cdot 10^{-3} \pm 0.02 \cdot 10^{-3}$, except for a region at the inflow and the outflow of the flume

The discharge through the flume is: $Q = 58 \cdot 10^{-3} \pm 0.1 \cdot 10^{-3} \text{ m}^3/\text{s}$ and is constant.

Measurements with the LDA are carried out from $x_1 = 15.0$ to $x_1 = 17.0 \text{ m}$ in several verticals at $x_2 = 0$, the axis of the flume.

The undisturbed waterdepth just upstream the dune, at $x_1 = 15.00 \text{ m}$ is: $a = 0.234 \pm 0.001 \text{ m}$.

So the mean flowvelocity in that cross-section is: $\bar{U}_1 = 0.496 \pm 0.008 \text{ m/s}$.

The mean temperature of the water during the experiments is: $T = 19.0 \pm 0.5 \text{ }^\circ\text{C}$, and the density of the water is: $\rho_w = 1000 \text{ kg/m}^3$.

The kinematic viscosity of the water is: $\nu = 1.029 \cdot 10^{-6} \pm 0.013 \cdot 10^{-6} \text{ m}^2/\text{s}$.

The waterdepth and the shape of the solitary dune are given in chapter 4.

An impression of the solitary dune on the conveyor is given in figure 3.4.

Over the dune the flow accelerates and furthermore the width of the dune is only 0.20 m, while the width of the flume is 0.50 m.

The dune is supported at the sides by perspex walls.

Due to the perspex walls the flow near the bottom is divided into three sections.

The height of the perspex walls is 0.10 m., while the waterdepth is more than 0.20 m, so the supports remain under water.

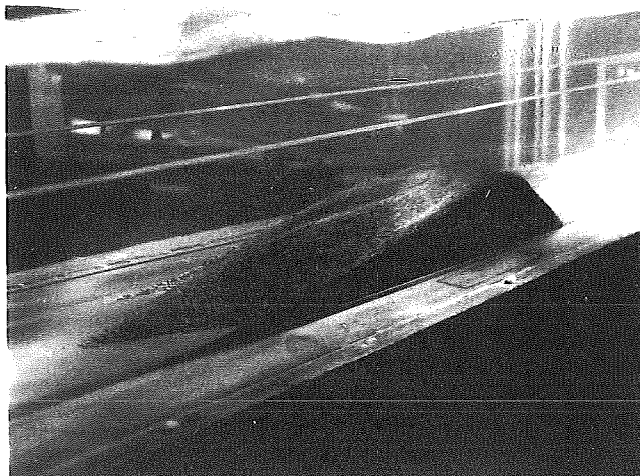


Figure 3.4: The solitary dune inbetween the perspex supports.

The flowfield is disturbed by the perspex supports, but only through the supports the creation of a nearly two-dimensional stationary dune is possible.

No mean flowvelocity or Reynoldsnumber over the dune is given, because the complete flowfield in the three sections is not measured.

The roughness of the glass walls of the flume and the perspex supports is: $k_w = 0.3 \cdot 10^{-3}$ to $0.4 \cdot 10^{-3}$ m. The roughness of the concrete bottom of the flume and the conveyor belt is: $k_b = 0.3 \cdot 10^{-3}$ to $0.5 \cdot 10^{-3}$ m. The sand used for the dune has a uniform diameter of 10^{-3} m and its density is: $\rho_s = 2650$ kg/m³. The total weight of the sand on the conveyor is: 5.2 kg (dry weight).

3.4 Measurements

3.4.1 General

The measurements of instantaneous flowvelocities is carried out with the Laser Doppler Anemometer (LDA). The principle of the LDA is treated in section 3.2, a more extensive treatment is given in appendix A. The sedimenttransport can be easily determined when the conveyor belt velocity and the local dune height are known.

In this section the measured quantities of water and sediment are treated, also the influence of the size of the measuring volume is regarded.

3.4.2 Measured quantities

Watermovement:

The quantities measured with the LDA are two instantane perpendicular flowvelocity vectors in a vertical plane. When possible, flowvelocities are measured with the 45°-configuration of the laser beams (see appendix A). With this configuration measurements close to a wall or watersurface can be carried out.

Because the reference beams are in a horizontal plane and can reach the photodetectors on the other side of the flume when the 45°-configuration is used.

When the bottom is not horizontal, the beam configuration must be changed so that the reference beams lie in a plane parallel to the bottom.

Near the watersurface the configuration is rotated 180°, the illumination beam does not intersect the watersurface before reaching the measuring volume.

The watersurface is not complete at rest, so due to refraction of the beam the position of the illuminating beam intersecting the surface is not constant when the 45°-configuration should be used near the surface.

In figure 3.5 the different configurations are sketched.

In general the measured flowvelocity vectors make an angle $\alpha + \beta$ with the horizontal plane.

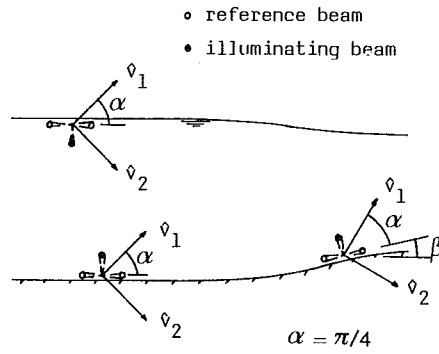


Figure 3.5: Beam configurations, in practice and definition.

The rotating grating in the LDA generates a frequency in the doppler signal of 48.5 Hz. So an analog low pass filter (LPF) is used with boundaries 0 to 45 Hz. The upper boundary is required to reduce the 48.5 Hz component sufficiently, it will be shown that after 45 Hz no important contributions to the signals occur. This is investigated by a measurement with LPF boundaries 0 to 200 Hz. Sample intervals for the A/D conversion are chosen in a way aliasing is prevented. In the case of LPF boundaries 0 to 45 Hz the sample interval is: $f_s = 100$ Hz, in the case of 0 to 200 Hz, the sample interval is: $f_s = 500$ Hz. The duration of the measurements is 8 minutes and in some cases 15 minutes. An overview of measurements is given in table 3.A.

Table 3.A			
	measuring time (s)	f_s (Hz)	LPF boundaries (Hz)
horizontal bed	480	100	0 to 45
	900	500	0 to 200
solitary dune	240	100	0 to 45

Measurements with a duration of 4 minutes (240 s) appeared to be long enough, compared to the results of measurements of 8 minutes (480 s) only slight differences occurred (see sub-section 4.2.2). The processing of the measured instantaneous flow velocities is treated in section 3.5.

Sedimenttransport:

The local sedimenttransport is calculated from the conveyor belt velocity and the local dune height, $S(x_1) = c_b \cdot z_b(x_1)$, the relation will be derived in chapter 4. Only in the axis of the flume the dune height is measured. The conveyor belt velocity is adjusted with an accuracy of 0.005 m/h, and is chosen so that the dune remains for several hours in the same position.

The dune height is determined with the LDA.

The measuring volume is moved vertically so that the reference beams of the LDA just intersect the dune surface, the presence of the signals on the tracker becomes zero.

The x_3 -coordinate of the measuring volume, now, is defined as the dune height at this x_3 -coordinate. The accuracy of the dune height determination in this way is: $0.5 \cdot 10^{-3}$ m.

3.4.3 Influence of the measuring volume

As derived in appendix A, the dimensions of the measuring volume in water read:

$$\Delta x_1 = 4 \cdot \lambda_0 \cdot f_3 / (\pi \cdot d_1 \cdot \cos \theta) ; \Delta x_2 = 4 \cdot \lambda_0 \cdot f_3 \cdot n / (\pi \cdot d_1 \cdot \sin \theta) ; \Delta x_3 = 4 \cdot \lambda_0 \cdot f_3 / (\pi \cdot d_1) \quad (3-1)$$

with:

- λ_0 : the wavelength of the laserlight in air (m)
- f_3 : focus length, of the lens just before the measuring volume (m)
- d_1 : the beam diameter after the rotating grating (m); $d_1 = d_0 \cdot f_2 / f_1$.
- d_0 : the beam diameter leaving the laser (m)
- f_1, f_2 : focus lengths, see figure 3.6.
- 2θ : angle between the illuminating and reference beam in air.
- n : refraction index between air and water.

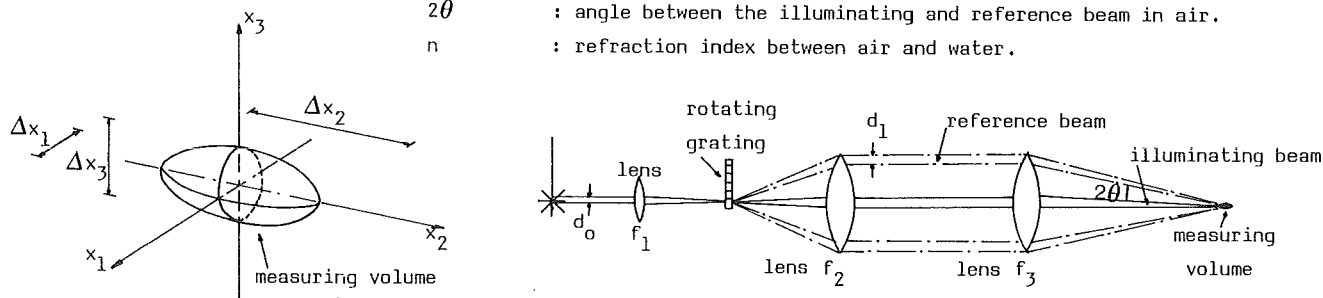


Figure 3.6: Measuring volume and definitions.

In the horizontal bed situation two dimensions of the measuring volume are tested, in the solitary dune situation one dimension is used.

The measuring volume can be made smaller by choosing lenses with different focus lengths.

To create a small measuring volume at some distance from the wall of the flume, the flume axis, the angle 2θ must be large and so the diameter of the lens f_3 must be large.

The measuring volumes used in the experiments are given in table 3.B, with the constants:

$$\lambda_0 = 632.8 \cdot 10^{-9} \text{ m} , d_0 = 10^{-3} \text{ m} \text{ and } n = 1.333 .$$

configuration:	Horizontal bed situation		Solitary dune situation		
	L1	L2	L2		
f_1	50 mm	120 mm	120 mm		
f_2	250 mm	250 mm	250 mm		
f_3	330 mm	330 mm	330 mm		
θ	5.25°	5.13°	5.20°		
d_1	5 mm	2 mm	2 mm		
Δx_1	0.05 mm	0.13 mm	0.13 mm		width
Δx_2	0.77 mm	1.98 mm	1.96 mm		length
Δx_3	0.05 mm	0.13 mm	0.13 mm		thickness
K_0	289373	282675	286722		

To measure small scale turbulence, which contains most of the turbulent energy, the measuring volume has to be so small, that the eddy sizes of importance are detectable.

The instantaneous flow velocity measured by the LDA is a mean value over the measuring volume.

When the measuring volume is relative large compared to the size of the eddies, the LDA does not detect the smaller eddies inside the measuring volume so the large volume is like a filter.

The mean flow velocity is not much influenced by a relative large measuring volume, but the turbulent quantities are affected by the relative large measuring volume, the measured values are smaller than expected.

In the experiments the turbulent quantities, $\overline{u_1^2}$, $\overline{u_3^2}$ and $\overline{u_1 u_3}$ are interesting. These quantities are mainly dominated by the Prandtl integral scale $l = \kappa \cdot x_3$ (Hinze, 1975). Eddies with this size and larger contribute mainly to the mentioned turbulent quantities. The Prandtl integral scale is only valid close to the wall, there also the smallest energy containing eddies occur.

From table 3.B it is clear that the principle dimension of the measuring volume is its length, which is directed in the x_2 -direction.

The main direction of the flow is in the x_1 - x_3 -plane, but turbulence is three-dimensional, so the x_2 -direction is of importance, and the length of the measuring volume as well.

The length of the measuring volume of the configuration L1 and L2 is, 1 mm respectively 2 mm.

So with the Prandtl integral scale $l = 0.4 \cdot x_3$ an estimate can be made for the distance from the wall at which the LDA does not detect the energy containing eddies very well.

With l is 1 mm respectively 2 mm, the distances from the wall are 2.5 mm, respectively 5 mm.

From the bottom to 2.5 mm, respectively from the bottom to 5 mm (L1 respectively L2) poor results of the turbulent quantities can be expected.

The influence of the size of the measuring volume is sketched in figure 3.7.

Near the watersurface the influence of the size of the measuring volume is much less, because the energy containing eddies are much larger in that area.

Figure 3.7 is an indication of the effect, results from preliminary measurements and experiments by the DHL are interpreted.

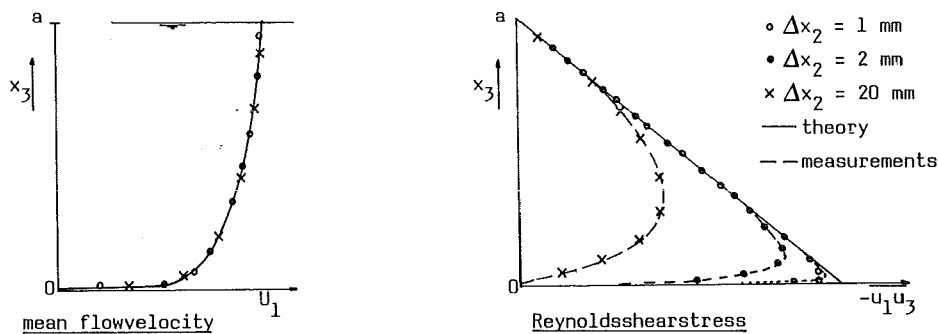


Figure 3.7: Effect of the size of the measuring volume on turbulent quantities, principle.

3.5 Processing of measured data

Mean flowvelocity:

As already mentioned in sub-section 3.4.2, two perpendicular flowvelocity vectors in a vertical plane are measured instantaneously by the LDA.

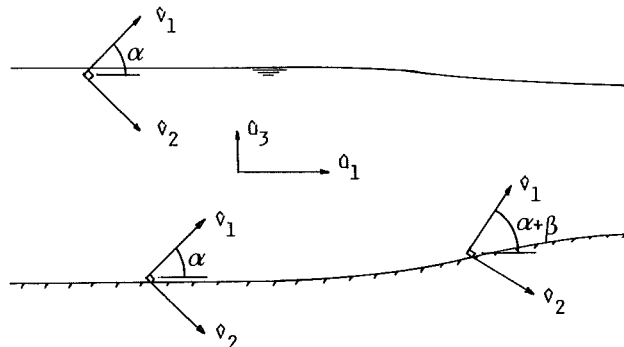


Figure 3.8: Measured flowvelocity vectors.

The flowvelocity vectors \hat{v}_1 and \hat{v}_2 are transformed to flowvelocity vectors \hat{u}_1 and \hat{u}_3 . In general the angle between \hat{v}_1 and \hat{v}_2 is $\alpha = \pi/4$, in the experiments.

But near the surface of the dune sometimes a different angle is used, when the shape of the dune blocks one of the beams ($\alpha + \beta$).

The instantaneous flowvelocity vectors \hat{v}_1 and \hat{v}_2 are transformed to \hat{u}_1 and \hat{u}_3 as follows:

$$\begin{aligned}\hat{u}_1(t) &= \hat{v}_1(t) \cdot \cos\alpha + \hat{v}_2(t) \cdot \sin\alpha \\ \hat{u}_3(t) &= \hat{v}_1(t) \cdot \sin\alpha - \hat{v}_2(t) \cdot \cos\alpha\end{aligned}\quad (3-2)$$

The measured data are stored digitally on tape, so the flowvelocities in the equations (3-2) are not continuous but discrete.

The flowvelocities read in a discrete form: $\hat{u}_1(t) = \hat{u}_{1j}$; $\hat{u}_3(t) = \hat{u}_{3j}$; $\hat{v}_1(t) = \hat{v}_{1j}$; $\hat{v}_2(t) = \hat{v}_{2j}$, with $j = 1, 2, \dots, N$.

The local mean flowvelocities are calculated as follows:

$$\begin{aligned}U_1 &= \frac{1}{N} \sum_{j=1}^N \hat{u}_{1j} \\ U_3 &= \frac{1}{N} \sum_{j=1}^N \hat{u}_{3j}\end{aligned}\quad (3-3)$$

The local turbulent fluctuations of the flow read (Reynoldsdecomposition):

$$\begin{aligned}u_{1j} &= \hat{u}_{1j} - U_1 \\ u_{3j} &= \hat{u}_{3j} - U_3\end{aligned}\quad (3-4)$$

This relation holds that: $\bar{u}_{1j} = \bar{u}_{3j} = 0$.

Turbulent energy:

The turbulent energy per unit mass can be estimated from the standard deviation of the fluctuations of the flowvelocity, this reads:

$$\begin{aligned}\overline{u_1^2} &= \frac{1}{N-1} \sum_{j=1}^N u_{1j}^2 \\ \overline{u_3^2} &= \frac{1}{N-1} \sum_{j=1}^N u_{3j}^2\end{aligned}\quad (3-5)$$

The Reynoldsstress per unit mass, $-\overline{u_1 u_3}$, is estimated from the correlation between u_1 and u_3 and reads:

$$-\overline{u_1 u_3} = \frac{1}{N-1} \sum_{j=1}^N u_{1j} u_{3j}\quad (3-6)$$

The correlation coefficient between u_1 and u_3 is defined as (see Tennekes, 1977):

$$c = \frac{-\overline{u_1 u_3}}{(\overline{u_1^2} \cdot \overline{u_3^2})^{1/2}}\quad ((3-7)$$

The transformation of the equations from an arbitrary coordinate system to the x_1 - x_3 -coordinate system, is treated in appendix A.

The equations (3-5) and (3-6) can be extended to a more general form, the correlation functions. These functions show the correlation as a function of time between u_{1j} and itself, or u_{3j} and itself, auto-correlation functions, or u_{1j} and u_{3j} , cross-correlations functions.

One of the two signals is delayed with respect to the other, over a time $t = n \cdot \Delta t$, in which Δt is the sample interval and $n = 1, 2, \dots$

Then a multiplication over the complete time interval is carried out.

In figure 3.9 an example of the cross-correlation function is given.

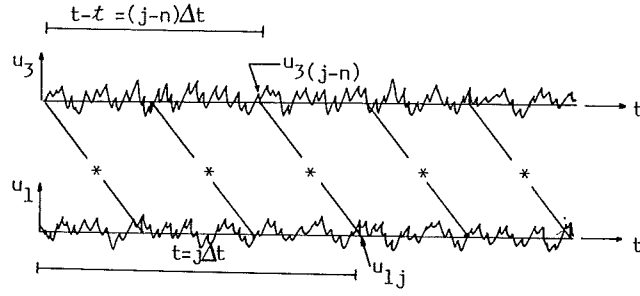


Figure 3.9: Principle of cross-correlation of u_{1j} and $u_3(j-n)$.

The auto-correlation functions read:

$$c_1(t) = \frac{\overline{u_1(t) \cdot u_1(t-t)}}{u_1^2}, \text{ or discrete: } c_1(n, \Delta t) = \frac{1}{N-1} \frac{\sum_{j=1}^N u_{1j} \cdot u_{1(j-n)}}{u_1^2} \quad (3-8)$$

$$c_3(t) = \frac{\overline{u_3(t) \cdot u_3(t-t)}}{u_3^2}, \text{ or discrete: } c_3(n, \Delta t) = \frac{1}{N-1} \frac{\sum_{j=1}^N u_{3j} \cdot u_{3(j-n)}}{u_3^2}$$

The cross-correlation function reads:

$$c_{13}(t) = \frac{\overline{-u_1(t) \cdot u_3(t-t)}}{(\overline{u_1^2} \cdot \overline{u_3^2})^{1/2}}, \text{ or discrete: } c_{13}(n, \Delta t) = \frac{1}{N-1} \frac{\sum_{j=1}^N u_{1j} \cdot u_{3(j-n)}}{(\overline{u_1^2} \cdot \overline{u_3^2})^{1/2}} \quad (3-9)$$

It is clear that for $t = 0$, the equations (3-8) and (3-9) read: $c_j(0) = c_3(0) = 1$ and $c_{13}(0) = \overline{-u_1 u_3} / (\overline{u_1^2} \cdot \overline{u_3^2})^{1/2}$. The general shape of a correlation function for stochastic signals, is given in figure 3.10.

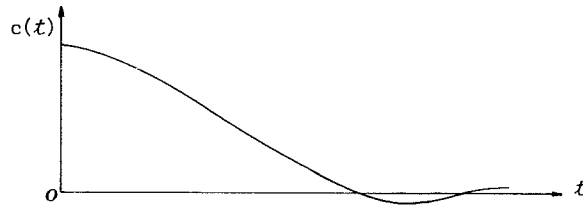


Figure 3.10: General shape of a correlation function.

The correlation function does not in general cross the time axis, this depends on the signal (Tennekes, 1977). From the correlation function the decay of the correlation with time can be estimated. From the viewpoint of turbulence the following deviation is added (see Hinze, 1975):

The Euler integral scale time is defined as:

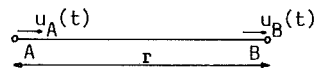
$$T_E = \int_0^{\infty} c(t) dt \quad (3-10)$$

and the Euler dissipation time scale reads:

$$D_E = \left[-\frac{1}{2} \frac{\partial^2 c(t)}{\partial t^2} \right]_{t=0}^{-1/2}$$

Also a spatial correlation can be defined as:

$$f(r) = \frac{\overline{u_A(t) \cdot u_B(t)}}{(\overline{u^2})}$$



The integral scale (Prandtl) reads:

$$L_f = \int_0^{\infty} f(r) dr \quad (3-11)$$

and the dissipation scale reads:

$$D_f = \left[-\frac{1}{2} \frac{\partial^2 f(r)}{\partial r^2} \right]_{r=0}^{-1/2}$$

For a flowfield with a mean uniform flow velocity $\bar{U}_1 \ll u_1$ a simple relation between T_E and L_f holds, with the aid of $x_1 = \bar{U}_1 \cdot t$:

$$L_f = \bar{U}_1 \cdot T_E \tag{3-12}$$

and so: $f(x_1) = c(t) \tag{3-13}$

Equation (3-13) means that the spatial and time correlations are equal. The turbulence is isotropic and homogeneous ($u_1^2 = u_2^2 = u_3^2 = \text{constant}$ throughout the fluid).

And from equation (3-12) and the time correlation function, the integral scale L_f can be estimated.

Power spectra:

To investigate the turbulent energy in detail, power spectra are useful .

The power spectra are calculated numerically with a Fast Fourier Transform (FFT) computer routine.

The Fourier Transformation for a discrete finite signal f_{j+1} reads:

$$F_{k+1} = \sum_{j=0}^{N-1} f_{j+1} e^{-i(2\pi \cdot j \cdot k/N)} \quad ; \quad \begin{cases} k = 0, 1, \dots, N-1 \\ i = \text{complex number.} \end{cases} \tag{3-14}$$

The signal f_{j+1} can be any desired signal.

In the case of power spectra from turbulent quantities, the following expressions are used (Blackman, 1958):

E_1 : power spectrum of u_1	$f_{j+1} = c_1(t)$, see equation (3-8)
E_3 : power spectrum of u_3	$f_{j+1} = c_3(t)$, see equation (3-8)
E_{13} : power spectrum of $-u_1 u_3$	$f_{j+1} = c_{13}(t)$, see equation (3-9)

The power spectra are usually plotted on logarithmic scales and the frequency axis is often transformed to a wavenumber axis, via the relation:

$$k_1 = \frac{2 \cdot \pi \cdot \nu}{U_1} \quad (L^{-1}) \tag{3-15}$$

With ν as the frequency in Hz and U_1 is the local mean flowvelocity.

The power spectra E_1 , E_3 and E_{13} ($L^3 T^{-2}$) are plotted as a function of k_1 .

The power spectra given in this report, are one-dimensional spectra, in fact only a three-dimensional spectrum of the turbulent energy k is correct, because turbulence is three-dimensional.

But in the experiments only the flowvelocity vectors in the x_1 - and x_3 -direction could be measured instantaneously, so the power spectra of u_1 and u_3 are treated separately as one-dimensional spectra.

A three-dimensional power spectrum is shaped as sketched in figure 3.11, the scales are logarithmic.

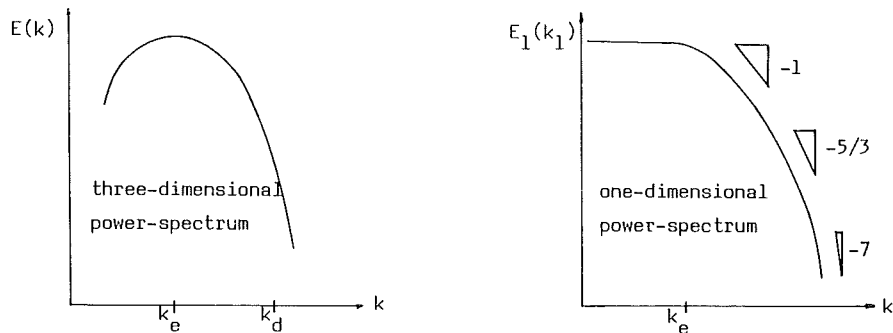


Figure 3.11: General shape of power spectra.

The wavenumber for which the viscosity becomes important is $k_d = \eta^{-1}$ (Hinze, 1975), with η as Kolmogorov-scale. The maximum of the spectrum lies around k_e , where $k_e \cdot \eta \approx 0.1$ (theoretically 0.09).

This spectrum is valid for the inertial sublayer in boundary layer flows and because no measurements could be carried out in the viscous layer but only in the inertial sublayer and the outer region, the calculated spectra from measurements are shaped as in figure 3.11.

Because the total turbulent energy could not be measured, one-dimensional spectra are calculated which are shaped as presented in figure 3.11.

The extra contribution to the $E_1(k_1)$ spectrum for low wavenumbers is due to flow movements in the two other directions (x_2 and x_3).

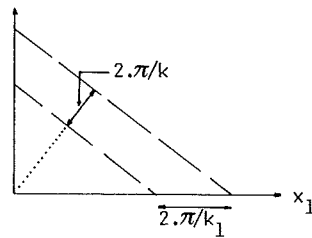


Figure 3.12: Contribution of waves in other directions to $E_1(k_1)$.

Wavenumbers $k \geq k_1$ in other directions than strictly x_1 , contribute to the one-dimensional spectrum, so extra energy with small wavenumbers is added to the spectrum.

The effect, sketched in figure 3.12, is important, because the turbulent energy for small wavenumbers should become zero.

Therefore the region of the power spectrum, with small wavenumbers should be omitted when results are interpreted.

The shape of the one-dimensional power spectrum can be considered in more detail, see figure 3.11.

Near the wall a strong production of turbulence takes place which means a strong interaction between mean and turbulent flow; further away from the wall this interaction decays.

In Hinze (1975) a complete derivation is given on the shape of the one-dimensional spectrum, here only the results are given.

According to Tchen, the slope of the spectrum is -1 for a wide range of wavenumbers.

In the case of small interaction of turbulent and mean flow, Kolmogorov's law holds, which says that the slope of the spectrum is -5/3, for a wide range of wavenumbers.

Panchev extended the theory of Tchen and derived, in case of a strong interaction between turbulent and mean flow, that the slope is -1 and changes continually to -7, for wavenumbers near infinity.

In the experiments described in this report, the maximum value of the wavenumber is about 1000.

So near the wall, where a strong interaction occurs between turbulent and mean flow, the slope of the spectrum is about -1, which decreases via -5/3 to even smaller values. This is an effect of the analog filter, which removes all frequencies above 45 Hz.

Further from the wall, the interaction between turbulent and mean flow decreases, and the slope of the spectrum is -5/3 in a region $50 < k < 500$ (according to Hinze, 1975).

The interesting part of the one-dimensional spectrum starts at the point where the spectrum has its maximum value. For smaller wavenumbers the spectrum should be omitted due to contributions of other directions, as pointed out before.

Finally the following relations hold for the power spectra:

$$\int_0^{\infty} E_1(k_1) dk_1 = \overline{u_1^2} \tag{3-16}$$

$$\int_0^{\infty} E_{13}(k_1) dk_1 = -\overline{u_1 u_3}$$

The surface of the spectrum can be integrated and compared with the turbulent quantities, to check the numerical routine.

Filtering:

In some cases it is convenient to have only the fluctuations of the flow velocity for further treatment directly, instead of the complete instantaneous flow velocity.

This can be achieved using an analog band pass filter (BPF) after the tracker.

The upper boundary can be chosen according to the noise level in the signal or to reduce the frequency due to the rotating grating.

The problem is, however, how to choose the lower boundary of the BPF. Because in fact the demand is to remove the mean flowvelocity component, but no turbulent fluctuations with low frequencies. This is important because the low frequencies of the turbulence contain most of the energy.

To investigate the effect of the lower boundary of the BPF, a digital filtering process with the aid of the computer is used.

The complete signal, mean and fluctuating flowvelocity, is transformed into a signal spectrum (an amplitude and phase spectrum).

Now the amplitudes and phases with low frequencies from zero to a certain value f_1 are made zero.

The filtered signal spectrum is transformed to the time domain, so a filtered signal remains.

The process is presented in figure 3.13.

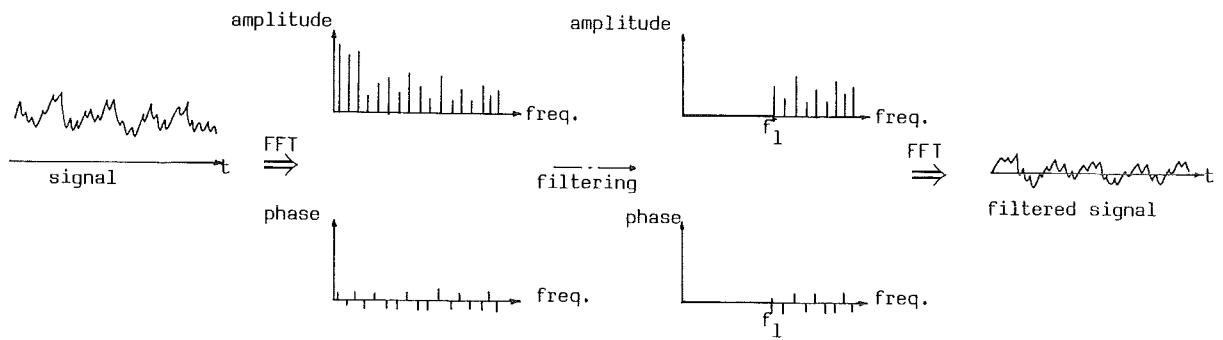


Figure 3.13: Principle of digital filtering process.

The value of f_1 can be varied, through which the influence of the lower frequencies on the turbulent quantities can be determined.

The main reason for the filtering is to investigate the influence of f_1 on the Reynolds shearstress, after filtering the shearstress is calculated again and can be compared to the not filtered shearstress.

The value of f_1 is varied from 0.1 to 20 Hz, with intervals of 0.2 Hz.

4. Results

4.1 Introduction

In this chapter the results of the experiments are given and are compared with analytical and numerical solutions of the flowfield.

In the horizontal bed situation the results are compared with an analytical solution.

In the solitary dune situation, no analytical solution is found, but the results are compared with a numerical solution of the flowfield. In this situation the sediment transport is determined.

The sediment transport and the local flowfield over the dune near the dunesurface are related.

Numerical values of measured flowquantities, plotted in the figures, can be found in tables in appendix C.

4.2 Watermovement

4.2.1 General

In the horizontal bed situation the measured mean flowvelocity and Reynoldsshearstress are compared with analytical solutions of these flowquantities.

The turbulent energy is considered and correlation functions and power spectra are calculated from the measured turbulent quantities.

Results are given for measurements with two different sizes of the measuring volume of the Laser Doppler Anemometer (LDA).

In the solitary dune situation the mean flowvelocity, Reynoldsshearstress and turbulent energy are compared with numerical solutions calculated with the ODYSSEE program (Alfrink, 1983).

The local Reynoldsshearstress near the surface of the dune is interesting because of the relation with the local sediment transport.

Correlation functions and power spectra are not calculated for this flowsituation.

The measurements in the solitary dune situation are carried out with the measuring volume which gives the best results in the horizontal bed situation.

4.2.2 Horizontal bed situation

The following flowquantities and data treatments are given in this sub-section:

mean flowvelocity profile, Reynoldsshearstress profile, turbulent energy, correlation functions, power spectra, the contribution of low frequencies to the Reynoldsshearstress, side wall effects, length of measuring time. All for the measuring volume L2 (see sub-section 3.4.3).

Finally the results of mean flowvelocity profile, Reynoldsshearstress profile and turbulent energy are given for the measuring volume L1; these results are not as satisfactory as expected.

Mean flowvelocity profile:

The flowfield in this situation is slightly convergent and stationary (sub-section 3.3.2), the conservation of momentum equation reduces to equation (2-14), derived in sub-section 2.2.2 and reads:

$$u_1 \frac{\partial u_1}{\partial x_1} = -g \frac{\partial a}{\partial x_1} + \frac{1}{\rho} \frac{\partial \tau}{\partial x_3} \quad (4-1)$$

The driving force per unit mass $g \cdot \partial a / \partial x_1$, is distributed over the shearstress term and the convection term.

The shearstressvelocity u_* is calculated from:

$$u_* = (g \cdot a \cdot i_c)^{\frac{1}{2}} \quad (4-2)$$

i_E is the energy slope. This slope is derived in sub-section 2.2.4 and reads:

$$i_E = \frac{\partial a}{\partial x_1} \cdot (1 - Fr^2) \quad , \quad Fr^2 = \frac{\bar{U}_1^2}{g \cdot a}$$

The shearstressvelocity is calculated for a very wide flume, because in the axis of the flume no effects from the side walls are noticed. This assumption is valid for this particular situation as will be pointed out in the part 'side wall effects' at the end of this sub-section.

With $\bar{U}_1 = 0.516$ m/s, $a = 0.093$ m, $\partial a / \partial x_1 = 0.992 \cdot 10^{-3}$ and $g = 9.81$ m/s² (from sub-section 3.3.2) equation (4-2) can be solved, so $u_* = 0.0253$ m/s.

The mean flowvelocity profile shows higher flowvelocities at some distance from the bottom to the water-surface due to convection, as pointed out in sub-section 2.2.4.

A logarithmic flowvelocity profile can be determined from the measured values in the area $0 < x_3^+ \leq 725$ for $Re \approx 10^4$ (Hinze, 1975)

In the area $x_3^+ \geq 725$ a wake function should be added to the logarithmic flowvelocity profile, the wake function is given in sub-section 2.2.4, equation (2-31) and reads:

$$W(x_3/a) = \frac{1}{2}(\sin(x_3/a - \frac{1}{2}) + 1)$$

In figure 4.1 the flowvelocity profile is presented in two ways, linear plot and logarithmic plot.

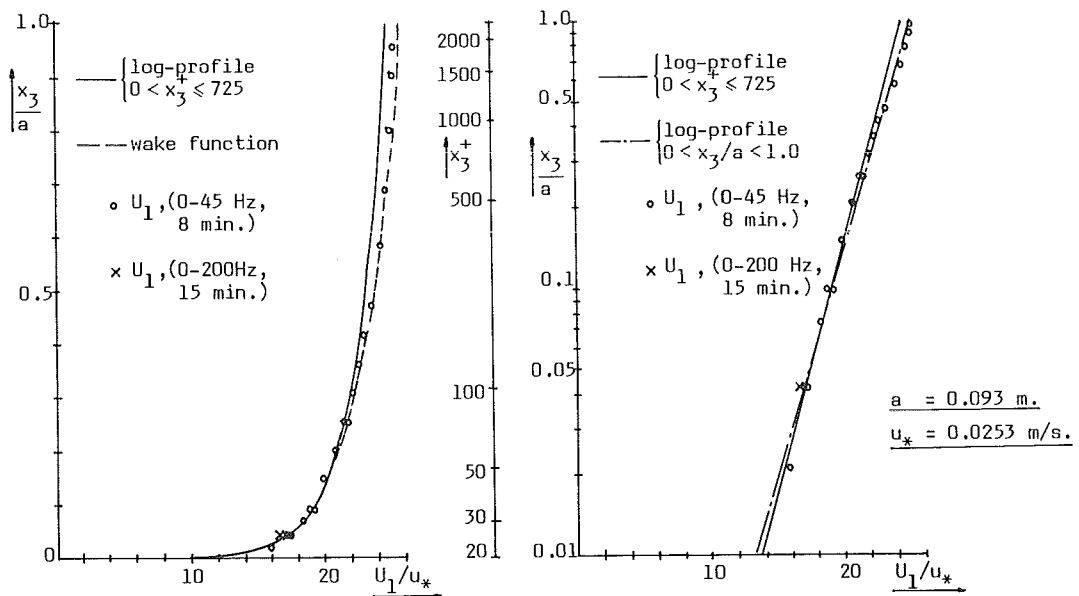


Figure 4.1: Measured mean flowvelocity profile, linear plot (left), logarithmic plot (right).

In general the logarithmic flowvelocity profile reads:

$$\frac{U_1}{u_*} = a_1 \cdot \ln\left(\frac{x_3 \cdot u_*}{\nu}\right) + a_2 \quad (4-3)$$

The coefficient a_1 and a_2 are calculated from all measured values by linear regression and, because the flow is convergent, also from measured values between $0 < x_3^+ \leq 725$.

Both results are compared with values for a_1 and a_2 which are generally accepted.

		a ₁	difference	a ₂	
P _c	complete profile	2.678	7%	4.674	
P _p	values 0 < x ₃ ⁺ ≤ 725	2.473	1%	5.722	
P ₁	from literature	2.5		5 to 8	(smooth/rough)

The profile P_p fits P₁ the best, the coefficient a₂ of P_p shows that the bottom of the flume is rather smooth.

The coefficient a₂ for the profile P_c is too small, due to the too high flow velocities near the watersurface. The profile P_c is calculated to demonstrate the effect of convection on the coefficients.

The mean flow velocity profile is also described by (see sub-section 2.2.3):

$$U_1 = \frac{u_*}{\kappa} \cdot \ln\left(\frac{x_3}{z_0}\right) \quad (4-4)$$

in which $\kappa = 0.4$, the von Kármán constant and z_0 is the wall roughness.

The complete flow velocity profile and values only near the bottom are used to calculate u_* and z_0 .

The results from a linear regression calculation are presented in table 4.B.

		u* (m/s)	difference	z ₀ (m)	difference
P _c	complete profile	0.0271	7%	7*10 ⁻⁶	75%
P _p	values 0 < x ₃ ⁺ ≤ 725	0.0250	1%	4*10 ⁻⁶	0%
P ₁	from theory	0.0253		4*10 ⁻⁶	

The theoretical value of z_0 is calculated from the Chézy equation: $Q/(B.a) = \bar{U}_1 = C.(R.i_E)^{1/2}$, with $C = 18 \log(12.R/(k + \delta/3.5))$ and $\delta = 11.6 * \nu / u_*$. The expression for z_0 reads: $z_0 \cong k/32$ (see de Vries, 1979). The value for z_0 calculated in this way is an overall value for the complete cross-section of the flume, the values for z_0 calculated from the measurements hold for the axis of the flume. So both values can not be compared in fact, however, the theoretical value of z_0 is used as an estimated value.

Here too, the profile P_p fits P₁ the best. The difference in z_0 between P_c and P₁ is flattering, because the values of z_0 in both cases are of the same order.

Again P_c is calculated to show the difference due to convection.

The wake function is plotted in figure 4.1 and it is striking that the measured flow velocities for $x_3^+ > 725$ fit the profile with the added wake function very well.

It shows that the assumptions for the influence of the convection on the mean flow velocity profile hold in this case.

Reynoldsshearstress profile:

From the measured instantaneous flow velocities, the cross-correlation of the fluctuating flow velocity components, u_1 and u_3 , is calculated, which is called the Reynoldsshearstress.

The total shearstress consists of a turbulent part and a molecular viscous part (see sub-section 2.2.2) and reads:

$$\frac{1}{\rho} \tau_{13}(x_3) = -\overline{u_1 u_3} + \nu \frac{\partial u_1}{\partial x_3} \quad (4-5)$$

The viscous part is only of importance close to the bottom, $x_3^+ < 30$, the derivative of u_1 can be calculated from the logarithmic flow velocity profile.

Theoretically the distribution of the total shearstress is linear from bottom to surface, in case of a stationary flow without convection and a completely developed boundary layer.

In case of a slight convection the profile can still be estimated with a linear profile, but the shearstress at the bottom reads, due to convection:

$$\tau_{13}(0) = \rho \cdot g \cdot a \cdot \frac{\partial a}{\partial x_1} \cdot (1 - Fr^2) \quad (4-6)$$

This equation holds for a very wide flume where no side wall effects occur in the axis of the flume, this holds for the experiment as well, which will be confirmed later.

The shearstress at the bottom in the axis of the flume reads, using the results:

$$\frac{1}{\rho} \tau_{13}(0) = u_*^2 = 6.40 \cdot 10^{-4} \text{ m}^2/\text{s}^2, \quad \text{and} \quad u_* = 0.0253 \text{ m/s.}$$

In figure 4.2 the measured Reynolds shearstresses are presented and also the linear theoretical shearstress profile. The viscous shearstress is calculated with the aid of the measured mean flowvelocity profile and is sketched in figure 4.2.

Also the shearstress profile in a developing boundary layer is presented in figure 4.2, see sub-section 2.2.4, the state of the development of the boundary layer in the experiment is regarded later.

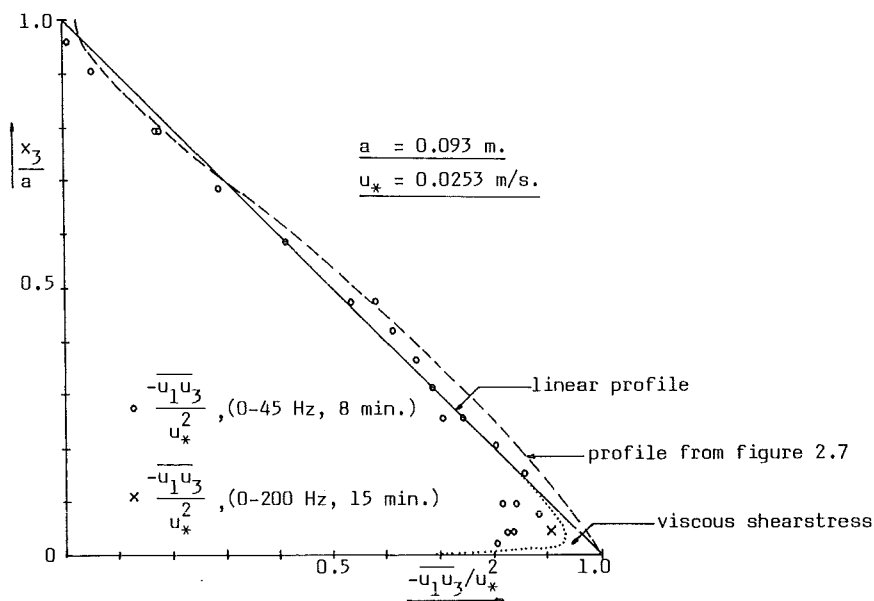


Figure 4.2: Measured Reynolds shearstresses.

The measured values fit the linear profile very well in general.

For the region $0.7 < x_3/a < 1.0$, the measured values are clearly smaller than the theoretical values (10% to 50%). This can be an effect of the free surface in the experiment, where due to air resistance a 'negative' shearstress is developed.

It can also be an effect of convection, because in this region convection has its greatest influence (see the mean flowvelocity profile). The term $g \cdot \partial a / \partial x_1$ from equation (4-1) is driving in this region for a great part the convection, so the shearstress must be less.

Near the bottom $0 < x_3/a < 0.1$, the measured Reynolds shearstress is too small, compared with the theoretical Reynolds shearstress (the dotted line in figure 4.2).

This is an effect of the size of the measuring volume of the LDA.

As pointed out in sub-section 3.4.3, small eddies near the bottom are too small to be noticed in the measuring volume by the LDA. These small eddies contain an important part of the turbulent energy contributing to the Reynolds shearstress.

In sub-section 3.4.3 the distance from the wall at which this effect should be noticed, is estimated for the L2 measuring volume and reads: $x_3/a = 0.054$.

From figure 4.2 it is clear that the effect due to the size of the measuring volume, occurs from $x_3/a < 0.1$. Although the difference seems to be large, the values are of the same order and the estimate is calculated from ideal data.

The value of $\tau_{13}(0)/\rho$ extrapolated from the measured Reynolds shearstresses is: $6.40 \cdot 10^{-4} \text{ m}^2/\text{s}^2$, so $u_* = 0.0253 \text{ m/s}$, which is equal to the theoretical value calculated from equation (4-2).

One measurement is carried out where all frequencies from zero to 200 Hz pass the Low Pass Filter (LPF), $x_3/a = 0.043$.

The value of $-\overline{u_1 u_3}$ is larger than the values measured in case all frequencies between zero and 45 Hz pass. This is an effect of the 48.5 Hz component in the signal due to the rotating grating and is definitely not turbulence.

So, however, the value fits theory better, it should be omitted.

The influence of the rotating grating is absent in the mean flow velocity (see figure 4.1), because the mean value of the 48.5 Hz component is zero.

The influence of the rotating grating is also shown in the part of the power spectra in this sub-section.

An estimate of the state of the boundary layer development can be made using equation (2-33).

With $U_0 \cong 0.516$ m/s and $u_* = 0.0253$ m/s (value at $x_1 = 16.0$ m) the angle of the development of the layer is $\alpha_b = 0.0156$ rad (0.9°).

So for a waterdepth of $a = 0.1$ m, the boundary layer is completely developed, from bottom to watersurface after: $0.1/\tan 0.9^\circ = 6.5$ m. The measurement are carried out at $x_1 = 16.0$ m.

Two remarks can be made.

Equation (2-33) is derived for a boundary layer in an infinite outer layer, here a free watersurface occurs, so does equation (2-33) hold? As a first estimate it will be sufficient.

Furthermore the boundary layer is completely developed after 6.5 m and measurements are carried out at $x_1 = 16.0$ m, but does the boundary layer start at $x_1 = 0.0$ m at the inflow? It can be reasonably stated that it does.

So regarding figure 4.2 it can be concluded that the boundary layer is completely developed and the measured values fit the theoretical linear profile very well.

Finally the parameter Π from equation (2-28) is calculated using equation (2-29) and figure 4.1.

$\Delta \cong 0.10$ m, $u_* = 0.0253$ m/s and $\partial U_0 / \partial x_1 \cong \Delta U_0 / \Delta x_1 = 0.05/1 = 0.05$ (from the surface slope)

So $\Pi \cong -0.2$ and is not equal to zero, for which equation (2-33) and figure 2.7 hold.

But Π is close enough to zero to use the equation and figure carefully.

Turbulent energy:

From the measured fluctuating flow velocities u_1 and u_3 , auto-correlations and cross-correlations are calculated.

These correlations can be interpreted as turbulent energies.

The total mean turbulent energy in an arbitrary point in the fluid is defined as: $k = \frac{1}{2}(\overline{u_1^2} + \overline{u_2^2} + \overline{u_3^2})$.

In the experiment, however, the flow velocity in the x_2 -direction is not measured, due to limitations of the LDA. So the u_2 -component of the fluctuating flow velocity vector is unknown.

It can be assumed that $u_2 \cong u_3$ (u_1 is the main direction), so that $k \cong \frac{1}{2}(\overline{u_1^2} + 2\overline{u_3^2})$, but this is not true in this case.

Near the wall the turbulence intensity is not equal in the x_2 - and x_3 -direction.

This follows from the general accepted values for u_2 and u_3 near the wall; $u_2 \cong 1.4 \cdot u_*$ and $u_3 \cong 0.8 \cdot u_*$.

Far from the wall isotropic turbulence could occur so $u_1 \cong u_2 \cong u_3$, but from the results presented in figure 4.3 it can be seen that this does not hold ($\overline{u_1^2} > \overline{u_3^2}$).

For these reasons no estimate for k is made from the results, only the $\overline{u_1^2}$ and $\overline{u_3^2}$ measured profiles are given.

Near the bottom, in the inertial layer, $x_3^+ > 30$, the following relations hold (see Tennekes, 1977):

$$\begin{aligned} u_1 &\cong 2 u_* & \overline{u_1^2} &\cong 4 u_*^2 \\ u_3 &\cong 0.8 u_* & \overline{u_3^2} &\cong 0.64 u_*^2 \\ k &\cong 3.5 u_*^2 \end{aligned}$$

The relations for $\overline{u_1^2}$ and $\overline{u_3^2}$ hold very well for the measured energies.

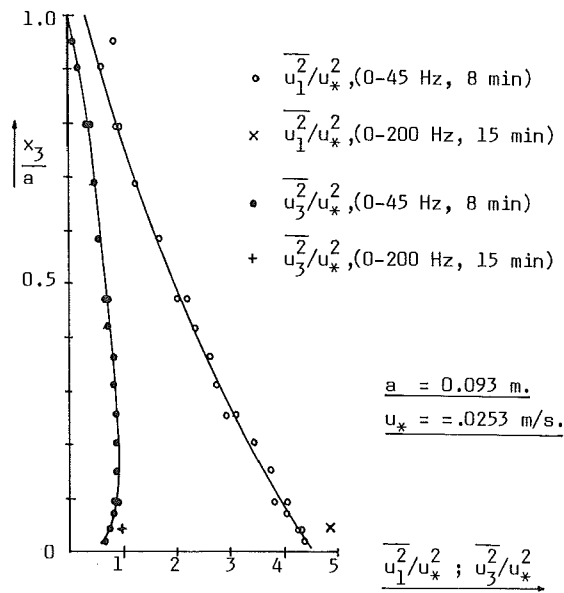


Figure 4.3: Measured turbulent energy, u_1^2 and u_3^2 .

The turbulent energy k is for slightly convergent flow almost linear from bottom to surface, because $\tau_{13}(x_3)$ is linear and $\tau_{13}(x_3) \sim u_*^2$, $k \sim u_*^2$, so $\tau_{13}(x_3) \sim k$. The linearity of k , mainly consisting of the u_1^2 -component, is not contradicted by the results presented in figure 4.3.

The measurement with frequencies from zero to 200 Hz, containing the 48.5 Hz component of the rotating grating, shows higher values of u_1^2 and u_3^2 , than the measurements with frequencies from zero to 45 Hz. The reason for this effect is already pointed out in the part of the Reynolds shear stresses.

Correlation functions:

For some points, where measurements are carried out, correlation functions are made of u_1 and u_3 . The functions: $\overline{u_1(t) \cdot u_1(t-\tau)} = \overline{u_1^2(t)}$, auto-correlation function of u_1 and $-\overline{u_1(t) \cdot u_3(t-\tau)} = -\overline{u_1 u_3(t)}$, cross-correlation function of u_1 and u_3 , are calculated in the vertical coordinates: $x_3 = 2, 4$ and 44 mm ($x_3/a = 0.0215, 0.043$ and 0.4731).

The results are presented in figure 4.4.

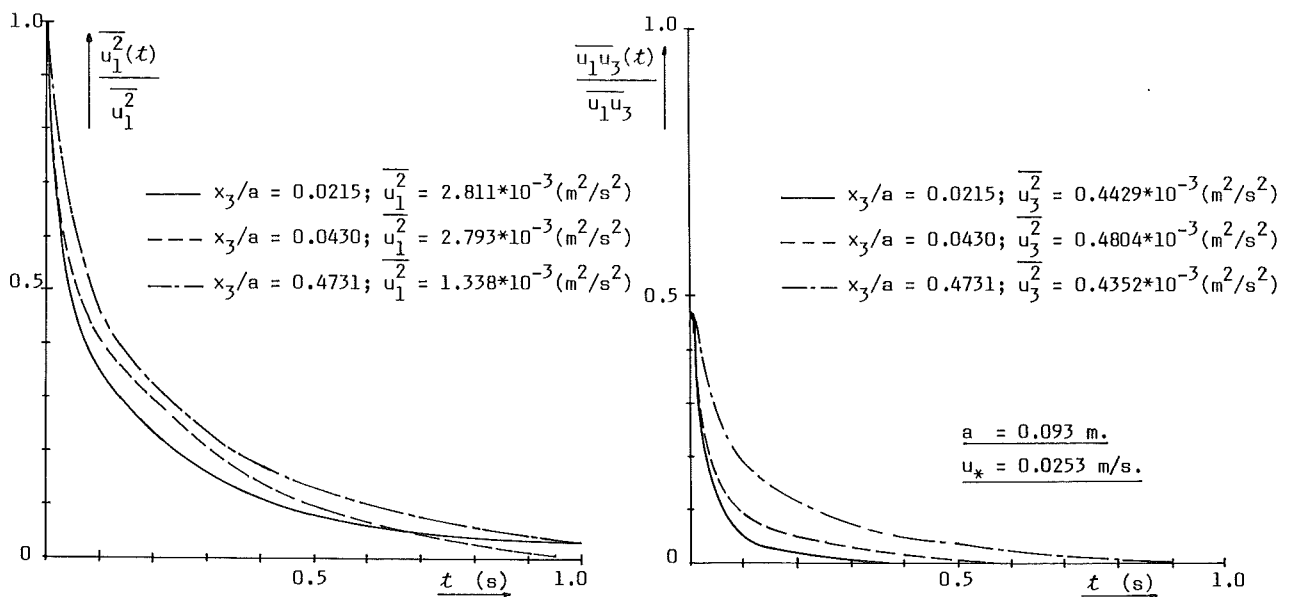


Figure 4.4: Auto-correlation function $\overline{u_1^2}$ (left), cross-correlation function $-\overline{u_1 u_3}$ (right).

The auto-correlation function of u_1 , shows that the correlation time is about 1 second and the correlation time of the cross-correlation function is about 0.5 second.

In both functions the correlation time for a point at some distance from the bottom ($x_3/a = 0.4731$) is longer than for a point close to the bottom ($x_3/a = 0.0215$ and 0.043).

This effect can be explained by the size of the eddies.

Near the wall the eddies are small due to the strong flowvelocity gradient and far from the wall eddies are larger.

So further from the wall turbulent fluctuations in the flowvelocity are correlated over a larger area than close to the wall through which the correlation time in a fixed point, further from the wall, increases.

Ofcourse the auto-correlation function for $t=0$ is one, due to the definition $\overline{u_1^2}(0) = \overline{u_1^2}$.

The cross-correlation function for $t=0$ is $-\overline{u_1 u_3}(0) \cong -0.45 \overline{u_1 u_3}$, in Tennekes (1977) the generally accepted value of the coefficient is 0.4, so the results from the measurements agree very well with results given in literature.

Power spectra:

For some points in the fluid, where measurements are carried out, one-dimensional power spectra are calculated ($x_3/a = 0.0215, 0.043$ and 0.4731).

With an analog low pass filter all frequencies higher than 45 Hz are removed from the instantaneous flowvelocity. The measuring time is about 8 minutes and the resolution of the spectrum is $(460.8)^{-1} = 0.00217$ Hz.

In one case ($x_3/a = 0.4731$) also another upper boundary of the filter is used, all frequencies higher than 200 Hz are removed from the signal, to investigate the effect of the 48.5 Hz component due to the rotating grating.

The measuring time in that particular case is about 15 minutes and the resolution of the spectrum is $(890)^{-1} = 0.00112$ Hz.

The power spectra are calculated with the aid of a Fast Fourier Transform (FFT) routine, see also section 3.5. The power spectra and auto- and cross-correlation are related as follows (see Hinze, 1975):

$$\int_0^{\infty} E_1(k_1) dk_1 = \overline{u_1^2} \quad \text{and} \quad \int_0^{\infty} E_{13}(k_1) dk_1 = -\overline{u_1 u_3}, \quad \text{with} \quad k_1 = \frac{2 \cdot \pi \cdot \nu}{U_1},$$

in which ν is the frequency and U_1 is the local mean flowvelocity.

The power spectra $E_1(k_1)$ and $E_{13}(k_1)$ in $x_3/a = 0.0215, 0.043$ and 0.4731 are presented in figure 4.5.

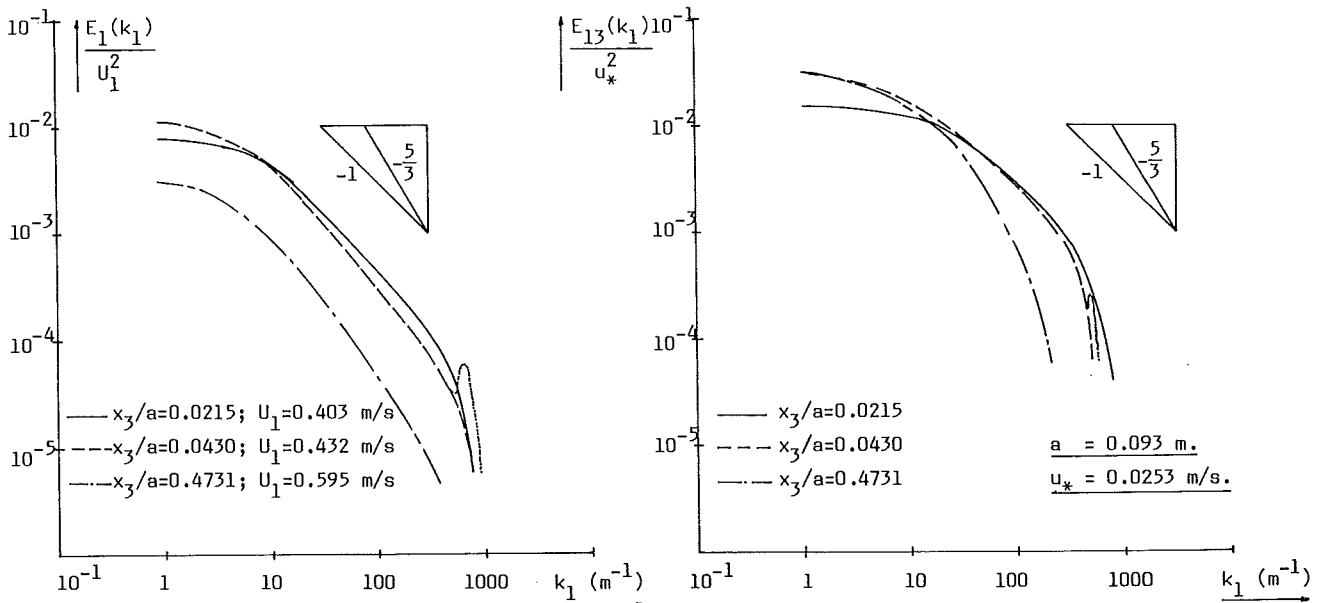


Figure 4.5: Power spectra, $\overline{u_1^2}$ (left) and $\overline{u_3^2}$ (right).

For $k_1 \leq 1$, the spectra are not interesting because the one-dimensional spectrum has no physical meaning in this region, as pointed out in section 3.5 .

The maximum for both spectra lies near $k_1 \cong 3$.

The $E_1(k_1)$ -spectrum has a slope -1 for $k_1 > 10$, for points near the wall ($x_3/a = 0.0215$ and 0.043) according to theory (section 3.5).

For $k_1 > 250$ the slope becomes steeper. For $x_3/a = 0.4731$, the $E_1(k_1)$ -spectrum has approximately a slope -5/3 in the region $30 \leq k_1 \leq 300$, according to theory for points at some distance from the wall.

A power spectrum is calculated for $x_3/a = 0.043$ with frequencies in the range of zero to 200 Hz.

In the results the 48.5 Hz component ($k_1 = 705$) can be seen.

The shape of the spectrum is not affected in the region $k_1 < 445$, whether the upper boundary of the filter removes frequencies higher than 45 Hz or 200 Hz.

So the choice of 45 Hz as upper boundary is satisfactory, because frequencies higher than, say 45 Hz do not contribute noticeable energy to the turbulent energy u_1^2 .

The contribution of the region $k_1 > 700$ is about 250 times less than the contribution in the region $1 < k_1 < 10$. Furthermore the 48.5 Hz component is no effect of turbulence and must be removed.

The most important frequencies contributing to turbulent energy lie in the region $1 < k_1 \leq 300$.

The values of $E_1(k_1)$ for $x_3/a = 0.4731$ are smaller than those for the points $x_3/a = 0.0215$ and 0.043 , because the total turbulent energy near the wall is higher than at some distance from the wall.

The total turbulent energy is the integral of the power spectrum over k_1 , these integrals are calculated and are compared with the theoretical result u_1^2 in table 4.C.

x_3/a	U_1 (m/s)	$\sum E_1(k_1)$	$\overline{u_1^2}$ (m ² /s ²)	difference	$\sum E_{13}(k_1)$	$-\overline{u_1 u_3}$ (m ² /s ²)	difference
0.0215	0.403	$2.795 \cdot 10^{-3}$	$2.810 \cdot 10^{-3}$	-0.5%	$0.503 \cdot 10^{-3}$	$0.517 \cdot 10^{-3}$	3%
0.0430	0.432	$2.864 \cdot 10^{-3}$	$2.891 \cdot 10^{-3}$	-0.9%	$0.542 \cdot 10^{-3}$	$0.550 \cdot 10^{-3}$	1.5%
0.4731	0.595	$1.326 \cdot 10^{-3}$	$1.392 \cdot 10^{-3}$	-5%	$0.343 \cdot 10^{-3}$	$0.359 \cdot 10^{-3}$	4.5%

The $E_{13}(k_1)$ -spectrum is less steep than the $E_1(k_1)$ -spectrum.

Near the wall, $x_3/a = 0.0215$ and 0.043 , the slope of the spectrum is -1, in the region $30 \leq k_1 \leq 300$ and becomes steeper in the region $k_1 > 300$.

For $x_3/a = 0.4731$ the slope of the spectrum is -5/3 in the region $30 \leq k_1 \leq 100$.

The power spectrum for $x_3/a = 0.043$ with frequencies from zero to 200 Hz, shows also a maximum value for $k_1 = 705$ (48.5 Hz component). Although it is less pronounced than in the $E_1(k_1)$ -spectrum.

For the three points ($x_3/a = 0.0215, 0.043$ and 0.4731) the values of $E_{13}(k_1)$ are almost equal in the region $1 < k_1 < 10$.

For higher values of k_1 the spectrum for $x_3/a = 0.4731$ shows lower values of $E_{13}(k_1)$, due to the minor importance of high frequencies at some distance from the wall.

The integrated power spectra over k_1 compared with the theoretical result $-\overline{u_1 u_3}$, is presented in table 4.C .

From the power spectra $E_1(k_1)$ and $E_{13}(k_1)$ it is clear that near the wall higher frequencies contribute also an important part to the turbulent energy, the region which contain important turbulent energy is $1 < k_1 < 300$.

Further from the wall the higher frequencies become less important and do not contribute any energy of importance to the turbulent energy, The important region is $1 < k_1 < 100$.

Contribution of low frequencies to Reynolds shear stresses:

The influence of low frequencies $0 < f_1 < 10$ Hz on the Reynolds shear stress (cross-correlation of u_1 and u_3) can be determined from the power spectra.

However, this is not done here, the influence is determined with the aid of a numerical filtering process in the frequency domain, see section 3.5 .

The results of the filtering are presented in figure 4.6, in which τ_{fil} / τ_0 is plotted versus f_1 .

τ_{fil} is the Reynolds shear stress calculated after filtering, τ_0 is the Reynolds shear stress before filtering, and f_1 is the upper boundary of the frequencies which are removed between zero and f_1 . The f_1 -axis is a logarithmic plot.

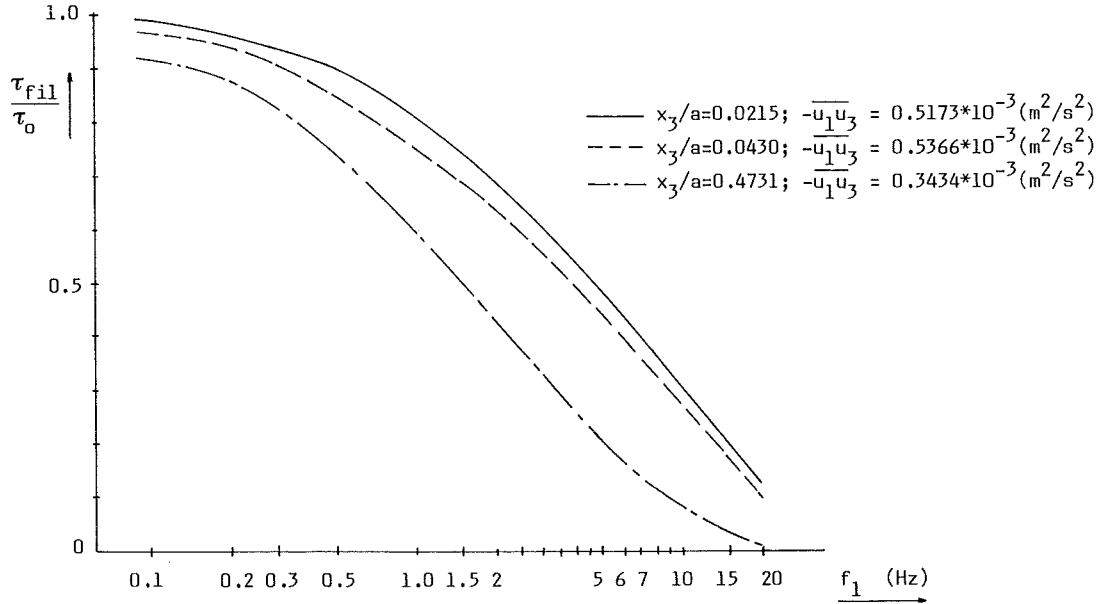


Figure 4.6: Influence of low frequencies on Reynolds shear stress.

The frequencies up to 15 Hz are of importance for $-\overline{u_1 u_3}$ for point near the wall, $x_3/a = 0.0215$ and 0.043 , as shown in figure 4.6 .

Further from the wall $x_3/a = 0.4731$ frequencies up to 6 Hz are of importance for $-\overline{u_1 u_3}$.

It is interesting to see if the burst frequency of the turbulence plays a role of importance.

The burst frequency reads (see Dronkers, 1983):

$$f_B = \frac{\overline{U}_1}{C_B \cdot a} \quad (4-7)$$

with $C_B = 3$ to 7 . The waterdepth is $a = 0.093$ m and $\overline{U}_1 = 0.516$ m/s, so in this flowfield $f_B = 0.8$ to 2 Hz.

For $x_3/a = 0.0215$ and 0.043 the shear stress decreases rapidly for $f_1 > 1.5$ Hz.

This is an indication that the burst frequency is of importance, higher frequencies (higher than 2 Hz) contribute considerably less to the shear stress.

Further from the wall the burst frequency is of less importance, because part of the energy of the bursts is already used.

So for $x_3/a = 0.4731$, τ_{fil}/τ_0 decreases gradually with f_1 which starts already from $f_1 = 0.2$ Hz.

The dependance of the Reynolds shear stress with f_1 is also given by Dronkers (1983) for measurements in situ. In that case the Reynolds shear stress also decreases rapidly for frequencies higher than the burst frequency.

Side wall effects:

The influence of side wall on the mean bottom shear stress can be estimated with the analytical method of Einstein and the graphical method of Knight (see sub-section 2.2.6).

With the Method of Einstein the following equation has to be satisfied:

$$\frac{1}{C_w^2 \cdot R_w} = \frac{1}{C_b^2 \cdot R_b} \quad (4-8)$$

The estimated roughness for wall and bottom is $k_w = k_b = 1.3 \cdot 10^{-4}$ m. With $\overline{U}_1 = 0.516$ m/s, $B = 0.50$ m, $i_E = 7.025 \cdot 10^{-4}$, $a = 0.093$ m and $\nu = 1.017 \cdot 10^{-6}$ m²/s, the hydraulic radius of wall and bottom are: $R_w = 0.067$ m and $R_b = 0.068$ m.

The mean shearstress for the wall or the bottom can be calculated with:

$$\tau = \rho \cdot g \cdot R \cdot i_E \quad (4-9)$$

So the mean wall shearstress is $\overline{\tau}_w/\rho = 4.617 \cdot 10^{-4} \text{ m}^2/\text{s}^2$ and the mean bottom shearstress is $\overline{\tau}_b/\rho = 4.686 \cdot 10^{-4} \text{ m}^2/\text{s}^2$.
The total shear force per unit mass is:

$$T_E = \frac{1}{\rho}(\overline{\tau}_w \cdot 2a + \overline{\tau}_b \cdot B) = 3.20 \cdot 10^{-4} \text{ m}^2/\text{s}^2$$

With the method of Knight the mean wall shearstress and the mean bottom shearstress, for $k_b/k_w = 1$ and $B/a = 5$, can be determined from figure 2.11 in sub-section 2.2.6 .

$\overline{\tau}_w/(\rho \cdot g \cdot a \cdot i_E) = 0.65$ and $\overline{\tau}_b/(\rho \cdot g \cdot a \cdot i_E) = 0.74$, so $\overline{\tau}_w/\rho = 4.166 \cdot 10^{-4} \text{ m}^2/\text{s}^2$ and $\overline{\tau}_b/\rho = 4.743 \cdot 10^{-4} \text{ m}^2/\text{s}^2$.
The total shear force per unit mass is:

$$T_K = \frac{1}{\rho}(\overline{\tau}_w \cdot 2a + \overline{\tau}_b \cdot B) = 3.15 \cdot 10^{-4} \text{ m}^2/\text{s}^2$$

The bottom shearstress is equal to $\rho \cdot u_*^2$, so u_* can be calculated.

Also u_* is extrapolated from the measured Reynolds-shearstress profile and u_* is calculated from the logarithmic part of the flowvelocity profile.

Comparing of the values of u_* calculated in different ways is done in table 4.D.

Table 4.D	u_* (m/s)	total shear-force per unit mass.	
extrapolated from measured Reynolds-shearstress profile.	0.0253		
calculated from flowvelocity profile $x_2^+ \leq 725$.	0.0250		local bottom shearstress
calculated from $u_*^2 = g \cdot a \cdot i_E (B \rightarrow \infty)$	0.0253		
calculated from $u_*^2 = g \cdot R \cdot i_E$, with $R = a \cdot B / (2a + B)$.	0.0216	$3.20 \cdot 10^{-4}$	
calculated with the method of Einstein.	0.0216	$3.20 \cdot 10^{-4}$	mean bottom shearstress
calculated with the method of Knight.	0.0218	$3.15 \cdot 10^{-4}$	

The situation in the axis of the flume is best described with the equations as if the flume is very wide. The values of u_* , as local shearstress velocity, from shearstress profile, flowvelocity profile and calculated for a very wide flume, agree very well.

The values of u_* calculated for a mean shearstress velocity also agree very well, however, they are less important because no complete shearstress distribution over the cross-section of the flume is measured, so no measured total shear force is known.

To confirm the absence of side wall effects near the axis of the flume, measurements are carried out in two verticals $x_2 = 0.025 \text{ m}$ and $x_2 = -0.025 \text{ m}$ at $x_1 = 16.0 \text{ m}$.

Mean flowvelocities, Reynolds-shearstresses and turbulent energies are measured in some points and are compared with measured profiles in the vertical $x_2 = 0$.

The results are presented in figure 4.7.

The mean flowvelocities fit the profile in the axis of the flume very well.

The Reynolds-shearstresses and the turbulent energies in $x_2 = \pm 0.025 \text{ m}$ fit the profile at $x_2 = 0$ also very well.

Only a slight asymmetric effect can be seen for all measured quantities, values at $x_2 = 0.025 \text{ m}$ are a little higher than those at $x_2 = -0.025 \text{ m}$.

Generally it can be stated that at least in a region $-0.025 \leq x_2 \leq 0.025 \text{ m}$ the values of U_1 , u_1^2 , u_2^2 and $-\overline{u_1 u_2}$ are almost equal at $x_1 = 16.0 \text{ m}$.

This supports the conclusion that side wall effects are absent in the axis of the flume in this experiment.

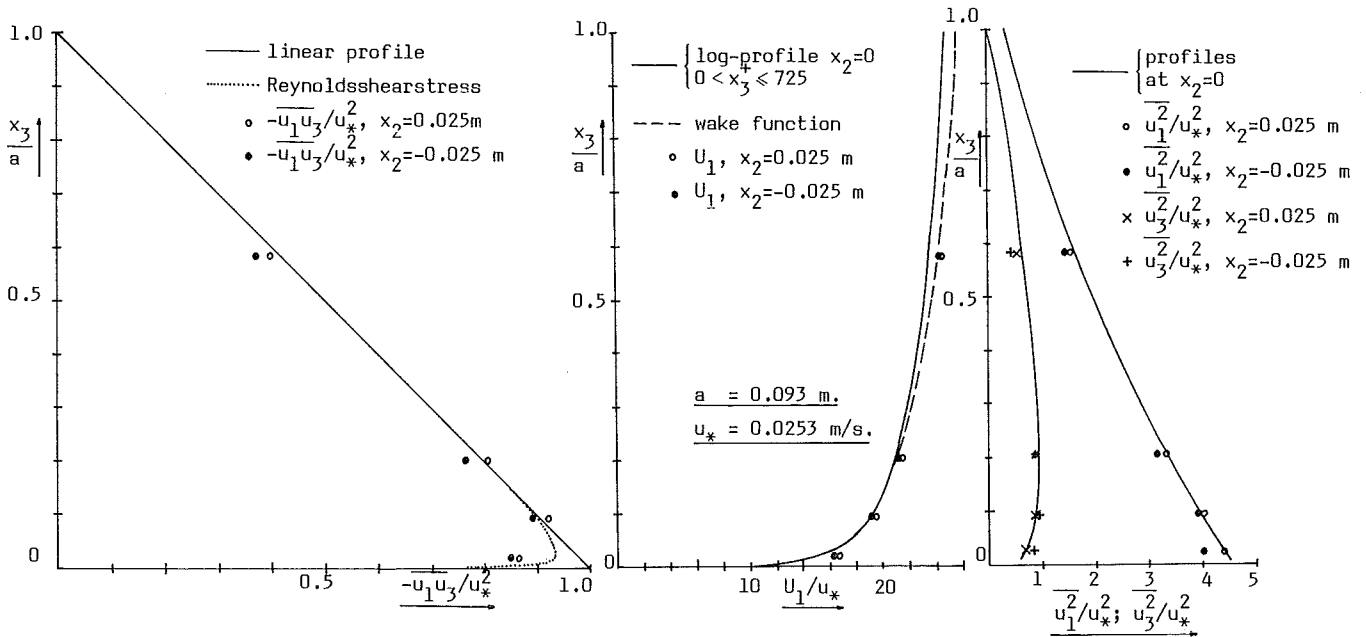


Figure 4.7: Reynolds shear stresses, mean flow velocity and turbulent energies at $x_2 = 0.025 \text{ m}$ and $x_2 = -0.025 \text{ m}$.

Length of measuring time:

The measuring time of an instantaneous flow velocity in a point is 8 minutes (only one point is measured 15 minutes for specific reasons)

To check whether this time is long enough or too long, the flow quantities are also calculated using only 4 minutes of the data.

The results are presented in table 4.E.

x_3/a	U_1 (m/s)		difference	$-\overline{u_1 u_3}$ (m^2/s^2)		difference
	8 min.	4 min.		8 min.	4 min.	
0.0215	0.4027	0.4010	0.4	$0.5173 \cdot 10^{-3}$	$0.5201 \cdot 10^{-3}$	-0.5
0.0430	0.4282	0.4282	0.0	$0.5366 \cdot 10^{-3}$	$0.5357 \cdot 10^{-3}$	0.2
0.0753	0.4655	0.4679	-0.5	$0.5667 \cdot 10^{-3}$	$0.5508 \cdot 10^{-3}$	2.8
0.0968	0.4791	0.4805	-0.3	$0.5410 \cdot 10^{-3}$	$0.5458 \cdot 10^{-3}$	-0.9
0.1505	0.5057	0.5051	0.1	$0.5507 \cdot 10^{-3}$	$0.5528 \cdot 10^{-3}$	-0.4
0.2043	0.5267	0.5279	-0.2	$0.5146 \cdot 10^{-3}$	$0.5163 \cdot 10^{-3}$	-0.3
0.2581	0.5427	0.5429	-0.1	$0.4756 \cdot 10^{-3}$	$0.4691 \cdot 10^{-3}$	1.4
0.3118	0.5592	0.5605	-0.2	$0.4374 \cdot 10^{-3}$	$0.4462 \cdot 10^{-3}$	-2.0

A measuring time of 4 minutes seems to be long enough, the difference for the mean flow velocity is less than $\pm 1\%$. The difference for the Reynolds shear stress is less than $\pm 3\%$.

For the measurements in the solitary dune situation a measuring time of 4 minutes is chosen.

Measuring volume L1:

The size of the measuring volume of the LDA is made smaller to measure the Reynolds shear stresses more accurate.

The length of the measuring volume is changed to about 1 mm (see sub-section 3.4.3), the width and thickness of the measuring volume are hardly changed.

Calculating the Prandtl mixing length scale, the measured Reynolds shear stresses should be accurate from 2.5 mm ($x_3/a = 0.0269$) distance from the bottom (see sub-section 3.4.3).

Measurements with the measuring volume L1 are carried out in the axis of the flume ($x_2 = 0$) at $x_1 = 16.0 \text{ m}$, and are compared with the results of measurements with the measuring volume L2.

Comparing the results of L1 and L2 is done in figure 4.8.

The mean flow velocity profile measured with L1 fits the profile measured with L2, but not satisfactory.

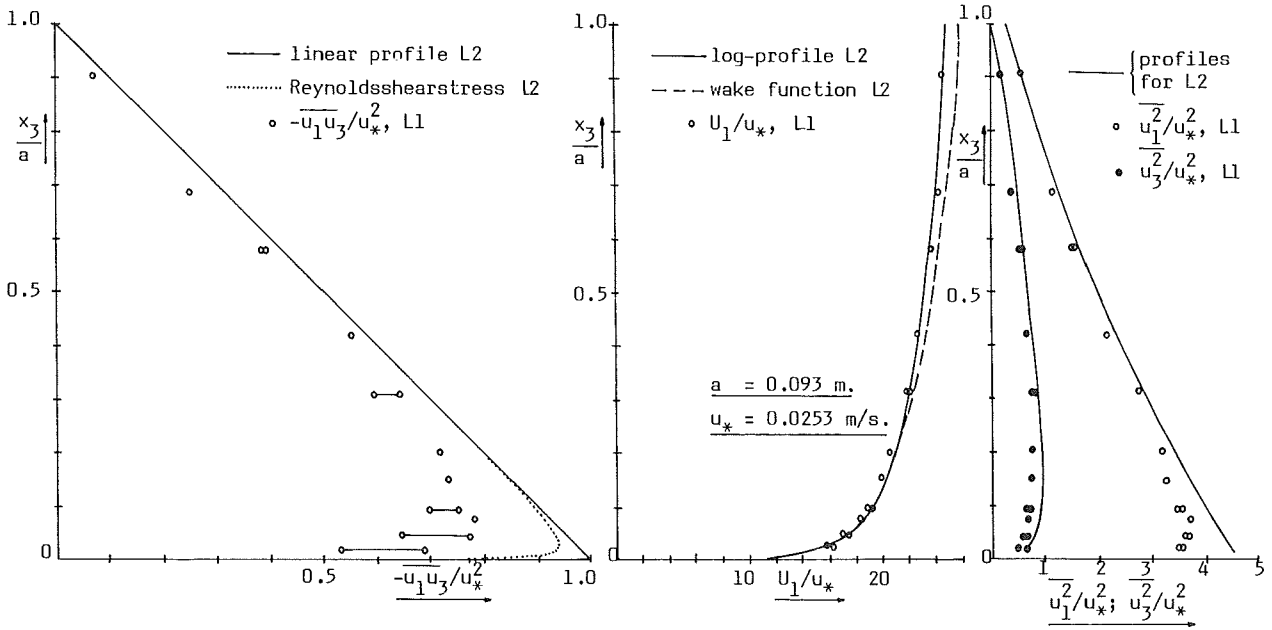


Figure 4.8: Reynolds shear stresses, mean flow velocity and turbulent energies for measuring volume L1.

The constants a_1 and a_2 from equation (4-2) and u_* and z_0 from equation (4-3) for the mean flow velocity profile measured with the measuring volume L1 are compared with the values for the measuring volume L2, the results are presented in table 4.F.

	a_1	difference	a_2	difference	u_* (m/s)	difference	z_0 (m)	difference
L1: logarithmic profile $0 < x_3^+ \leq 725$	2.249	9%	6.855	20%	0.0235	7%	$2.4 \cdot 10^{-6}$	40%
L2: logarithmic profile $0 < x_3^+ \leq 725$	2.473		5.772		0.0250		$4.0 \cdot 10^{-6}$	

The difference between the results of the two measurements is considerable.

From figure 4.8 it is also clear that the Reynolds shear stresses are very poor, too low values occur for $x_3/a < 0.4$.

This effect also occurs for the turbulent energies $\overline{u_1^2}$ and $\overline{u_3^2}$.

In general the results of the measurements with the measuring volume L1 are poor compared to results with the measuring volume L2.

Reasons for the poor results with L1 are:

- The measuring volume L1 is not adjusted as accurate as the measuring volume L2, the three laser beams do not intersect in one point. This was checked later in a test.
- The accuracy of the lenses is important for the creation of a very small measuring volume.

From tests with the optics of the measuring volume L1, it appeared that the dimensions of the measuring volume were not as calculated (see sub-section 3.4.3) but were even larger than the dimensions of L2 !

Preliminary measurements are also carried out with a measuring volume L20 (length of the measuring volume about 20 mm), but results are not presented here because they are too poor, due to a bad adjustment of the LDA optics. Interpretation of the results makes no sense.

So comparing results of the measuring volumes L1, L2 and L20, to show the effect treated in sub-section 3.4.3, can not be done unfortunately.

4.2.3 Solitary dune situation

The results of measurements with the LDA (measuring volume L2) and results of computations with the ODYSSEE computer program (Alfrink, 1983) of the flowfield in the solitary dune situation, are treated in this sub-section.

Measurements are carried out in three situations, the experiments: T1, T2 and T3.

The shape of the dune and the flowfield in the three experiments differ, due to disturbances in the flowfield, although the total discharge is constant for T1, T2 and T3.

To compare the measurements with theory and to test the mathematical model, a numerical solution of the flowfield over the dune is computed with the ODYSSEE program.

One calculation is carried out for a mean dune shape which fits the shape of the dunes in T1, T2 and T3 best.

The program solves the equations of mass and momentum, (2-3), (2-8) and (2-9), together with the k - ϵ equations, (2-41) and (2-42) numerically with finite difference methods in fractional time steps, as described in Alfrink (1983).

In this sub-section the following aspects are treated: The boundaries and grid and the boundary conditions for ODYSSEE, the numerical results, comparison of the measured and calculated flowfield, comparison of measured and calculated flowquantities along the dunesurface.

Boundaries and grid:

From the experiments T1, T2 and T3, a mean duneshape is determined which is used as a boundary for the calculation with ODYSSEE.

The dune is situated from $x_1 = 15.75$ m to $x_1 = 16.25$ m. Upstream and downstream the dune a horizontal bed with a length of 0.50 m is present, so the total length of the numerical model is 1.50 m, with an inflow boundary at $x_1 = 15.25$ m and an outflow boundary at $x_1 = 16.75$ m.

For the watersurface a rigid-lid approximation is made, with a waterlevel at $x_3 = 0.210$ for the complete model.

The geometry of the model is presented in figure 4.9.

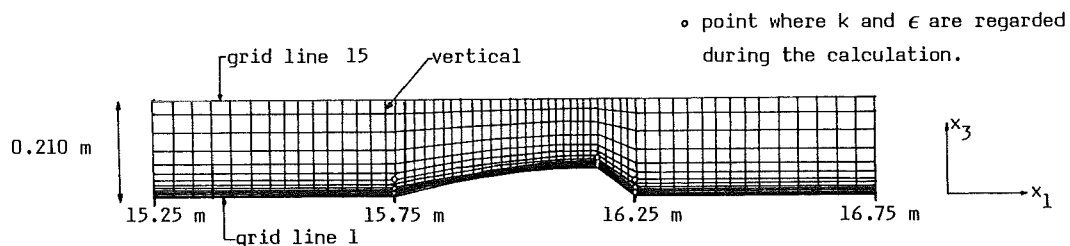


Figure 4.9: Geometry and grid used in the ODYSSEE computer program.

Only the coordinates of the boundaries are stated in the program, the grid is computed by ODYSSEE.

The program calculates a curvilinear grid for the field between the boundaries.

The grid consists of 15 grid lines and 60 verticals, the vertical coordinates of inflow and outflow boundary are divided logarithmically.

The waterdepth in the experiments at $x_1 = 15.00$ m is $a = 0.234$ m and at $x_1 = 15.45$ m $a = 0.210$ m, the strong decrease of waterdepth over this small distance is an effect of the perspex supports, which start at $x_1 = 15.25$ m. The waterlevel above the dune is also at $x_3 = 0.210$ m, although the watersurface is whirly.

For the calculation the waterlevel is chosen at $x_3 = 0.210$ m.

Boundary conditions:

The boundary conditions are already given in sub-section 2.2.5, here only the inflow boundary is treated more specifically.

In the experiments, the flow quantities upstream the dune at $x_1 = 15.45$ m and $x_2 = 0$ from bottom to water-surface are measured. This vertical is positioned inbetween the perspex supports.

The U_1 -profile is used for the inflow boundary at $x_1 = 15.25$ m, the U_1 -profile is a mean flow velocity profile which fits the profiles of T1, T2 and T3 best.

The measured values of U_3 in the vertical are very small and close to zero, so $U_3 = 0$ is stated at the inflow boundary.

Profiles for the turbulent energy k and the dissipation ϵ have to be estimated because only $\overline{u_1^2}$ and $\overline{u_3^2}$ are measured and $\overline{u_2^2}$ and ϵ could not be measured.

For uniform flow k is proportional to x_3 and ϵ is proportional to x_3^{-1} in a region near the bottom, in an equilibrium situation (law of the wall).

Both relations are used as an estimate for the profiles over the complete waterdepth and over the horizontal bed upstream the dune the profiles can adjust to equilibrium profiles.

The relations for k and ϵ read (see sub-section 2.2.5):

$$k = \frac{u_*^2}{\sqrt{c_\mu}} \cdot (1 - x_3) \quad \text{and} \quad \epsilon = \frac{u_*^3}{\kappa \cdot x_3} \quad (4-9)$$

with $c_\mu = 0.09$ and $\kappa = 0.4$.

A value for u_* must be known, so u_* is estimated from the U_1 -profile.

From the mean flow velocity profile U_1 at $x_1 = 15.45$ m for T1, T2 and T3, a mean value of u_* and z_0 is determined.

Using equation (2-20) and with linear regression the values read: $u_* = 0.0230$ m/s and $z_0 = 0.35 \cdot 10^{-6}$ m.

No estimate for u_* and z_0 is made from theory (equation (2-27) and the Chézy-equation), because the perspex supports produce sidewall effects and influence the flowfield in a way which can not be detected from the measurements.

With the equations (4-9) and the estimated value of u_* , k and ϵ can be calculated.

The boundary conditions at $x_1 = 15.25$ m are presented in figure 4.10, values are stated from $x_3 = 0.002$ m ($x_3 = 0$ belongs to the condition of the bottom) to $x_3 = 0.180$ m ($x_3 = 0.210$ m belongs to the condition of the watersurface).

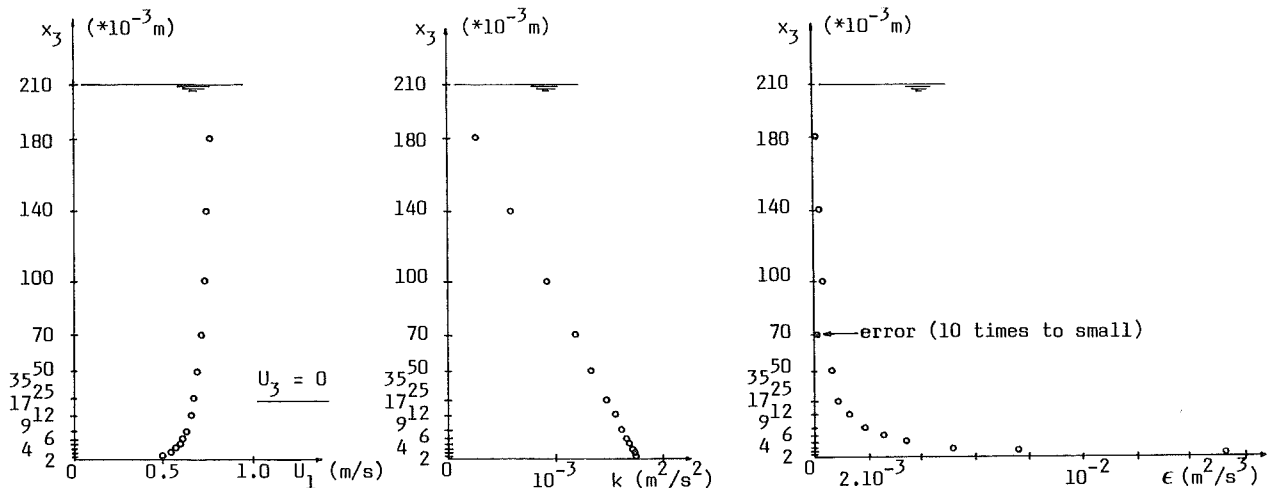


Figure 4.10: Inflow boundary conditions at $x_1 = 15.25$ m for ODYSSEE.

When the input data for ODYSSEE were prepared a value for $\epsilon(x_3=0.07$ m), which is 10 times smaller than ment, was used by mistake.

The results of the calculation are influenced by this, because the turbulent viscosity is proportional to ϵ^{-1} , so the turbulent viscosity is 10 times higher at $x_3 = 0.07$ m ($x_1 = 15.25$ m), see equation (2-40).

This affects the shearstress which is proportional to the turbulent viscosity (equation 2-22).

Furthermore ϵ influences k through the equations (2-41) and (2-42).

The disturbance due to the wrong value of ϵ will decay downstream, but due to diffusion it has also its influence in the x_3 -direction.

The effect of the disturbance will be regarded later.

Time step and convergance:

Before the results are regarded, the proces of the calculation is described.

The ODYSSEE program is based on difference methods in fractional time steps, how the equations are solved in detail is treated in Alfrink (1983).

The calculation starts from a non-stationary situation and iterates in time to a stationary solution of the flowfield.

A small time interval (= iteration step) is necessary, smaller than about 0,02 s for this case, to prevent an instable calculation.

The small time step is demanded by the interaction of U_1 , U_3 , k and ϵ .

An estimate of the time needed for a stationary solution can be made from the length of the model (1.50 m) and the overall mean flowvelocity (0.50 m/s), so $1.50/0.50 = 3$ seconds.

The small time interval and the required time result in a considerable amount of time steps.

In a few point in the grid (see figure 4.9), the values of k and ϵ (which become instable first) are plotted during the proces of calculation.

The results for 9 points (3 verticals, 3 points each) are presented in figure 4.11.

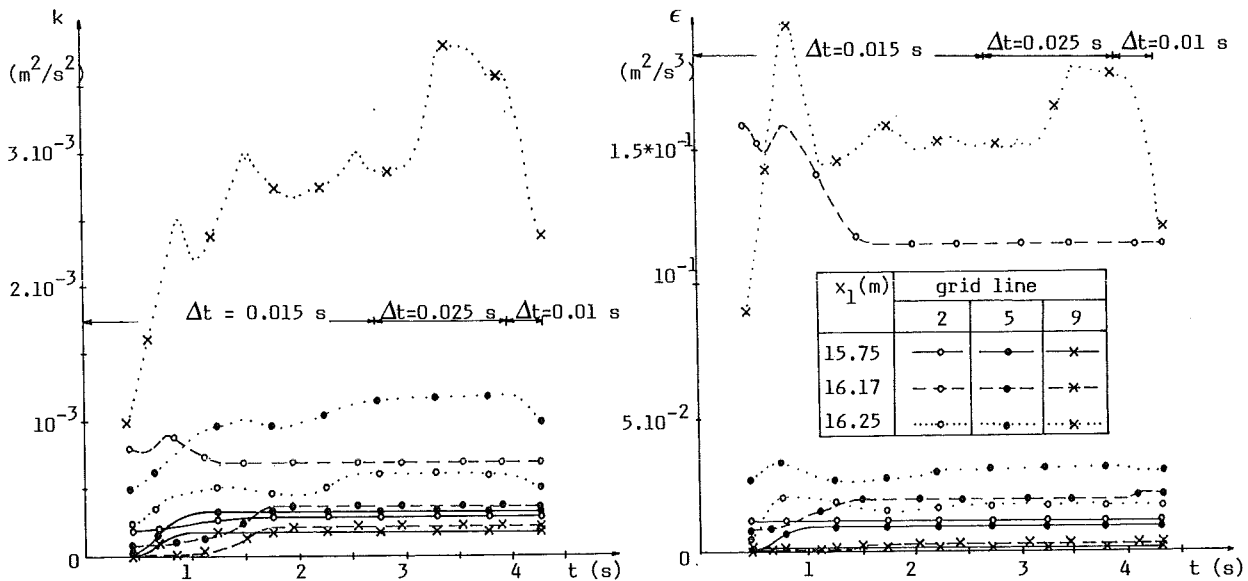


Figure 4.11: Development of k and ϵ in time during the calculation with ODYSSEE.

The calculation is started with a time interval of 0.015 s, k and ϵ at the foot and the top of the dune reach after about 2 s stationary values.

The proces in the wake takes longer, because this area is governed mainly by diffusion which has a larger time scale than the proces of accelerating flow above the dune.

After 2.73 s (173 time steps) the time interval is changed to 0.025 s.

The values above the dune remain stable, the values in the wake oscillate strongly, especially values in the point at the edge of the wake and the main flow.

After 3.95 s (220 time steps) the time interval is decreased to 0.01 s.

Again the values in the wake are influenced largely, the values decrease strongly for the point at the edge of wake and main flow.

After 4.305 s the calculation is stopped.

The flowfield above the dune is stationary and this part is most important, the wake is still developing, but is less interesting for the purpose of the investigation (the flowfield along the dune surface).

Numerical results:

The numerical results are presented in the figures 4.13 , 4.14 and 4.15 , but are treated extensively in the next part together with the experimental results.

To show some of the results of the calculation and the influence of the disturbance in ϵ at the inflow boundary, the turbulent viscosity in several cross-sections is presented in figure 4.12.

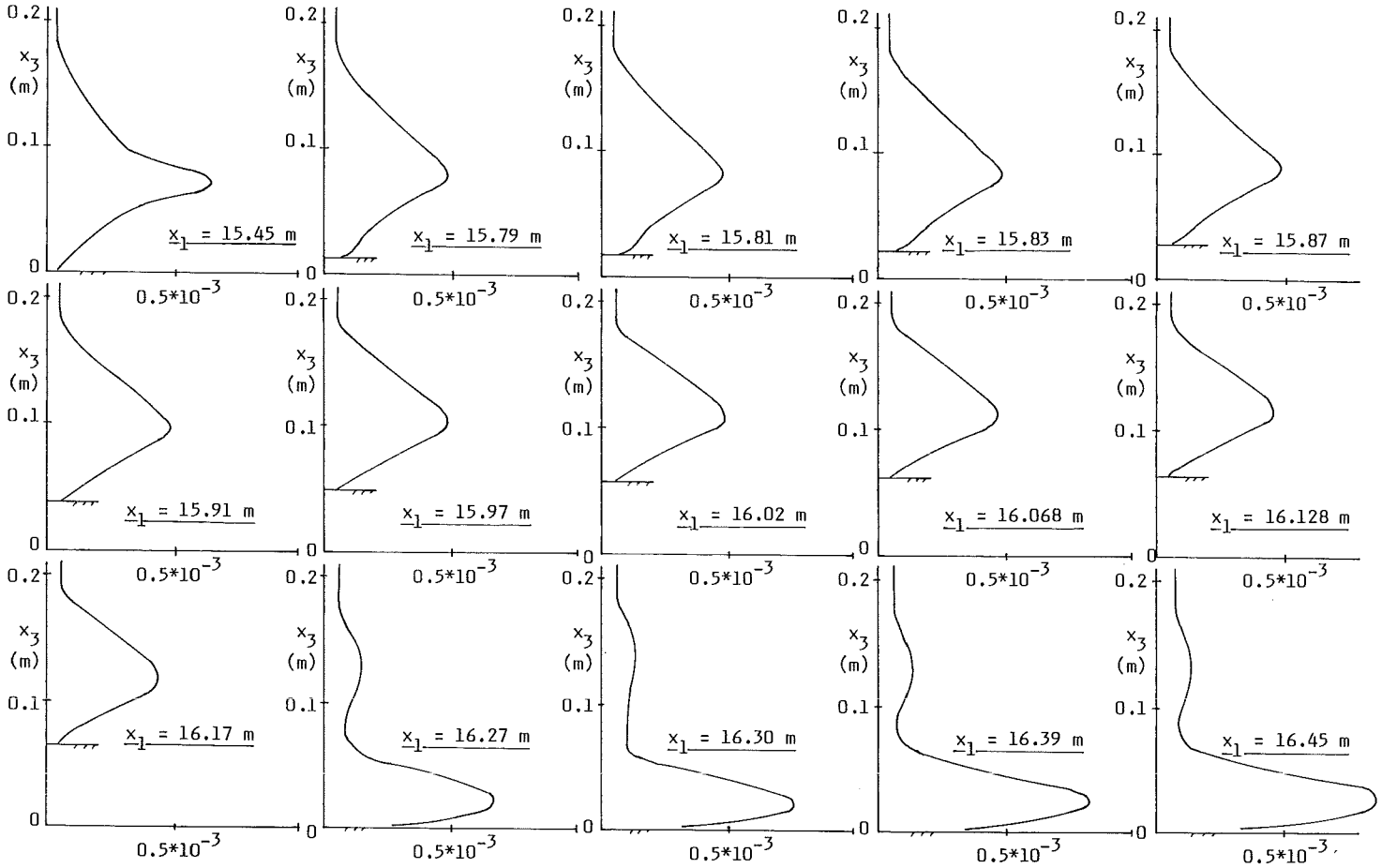


Figure 4.12: Calculated turbulent viscosity in several cross-sections, horizontal axis ν_t (m^2/s).

The coordinate $x_1 = 15.45$ m is chosen because the flowfield in the calculation can develop from the inflow boundary $x_1 = 15.25$ m to $x_1 = 15.45$ m and later the measured flow quantities at $x_1 = 15.45$ m are compared with the results of ODYSSEE.

The disturbance at $x_1 = 15.45$ m due to the small value of ϵ at $x_3 = 0.07$ m is clear, the influence is decreasing downstream.

As pointed out in sub-section 2.2.5, the boundary conditions at the watersurface, $\partial h / \partial x_3 = \partial \epsilon / \partial x_3 = 0$, give through equation (2-40): $\partial \nu_t / \partial x_3 = 0$, so at the surface the turbulent viscosity is not zero.

Apart from the disturbance the turbulent viscosity profile is satisfactory and has a nearly constant shape in the accelerating part of the flow above the dune.

In the wake the turbulent viscosity is large, due to the production of turbulence, furthermore the profile is still developing due to the developing of k and ϵ in the wake.

Comparison of experimental and numerical results:

Comparing results of the experiments T1, T2 and T3 with the numerical results of ODYSSEE, is done in the figures (4.13, 4.14 and 4.15).

At the top of the figures the shape of the dune in the experiments is plotted as well as the shape of the dune in ODYSSEE (solid lines)

In each figure the cross-sections are sketched where measurements are carried out.

Figure 4.13 : Results of experiment T1 (°, •), compared with numerical results of ODYSSEE (—, - -).

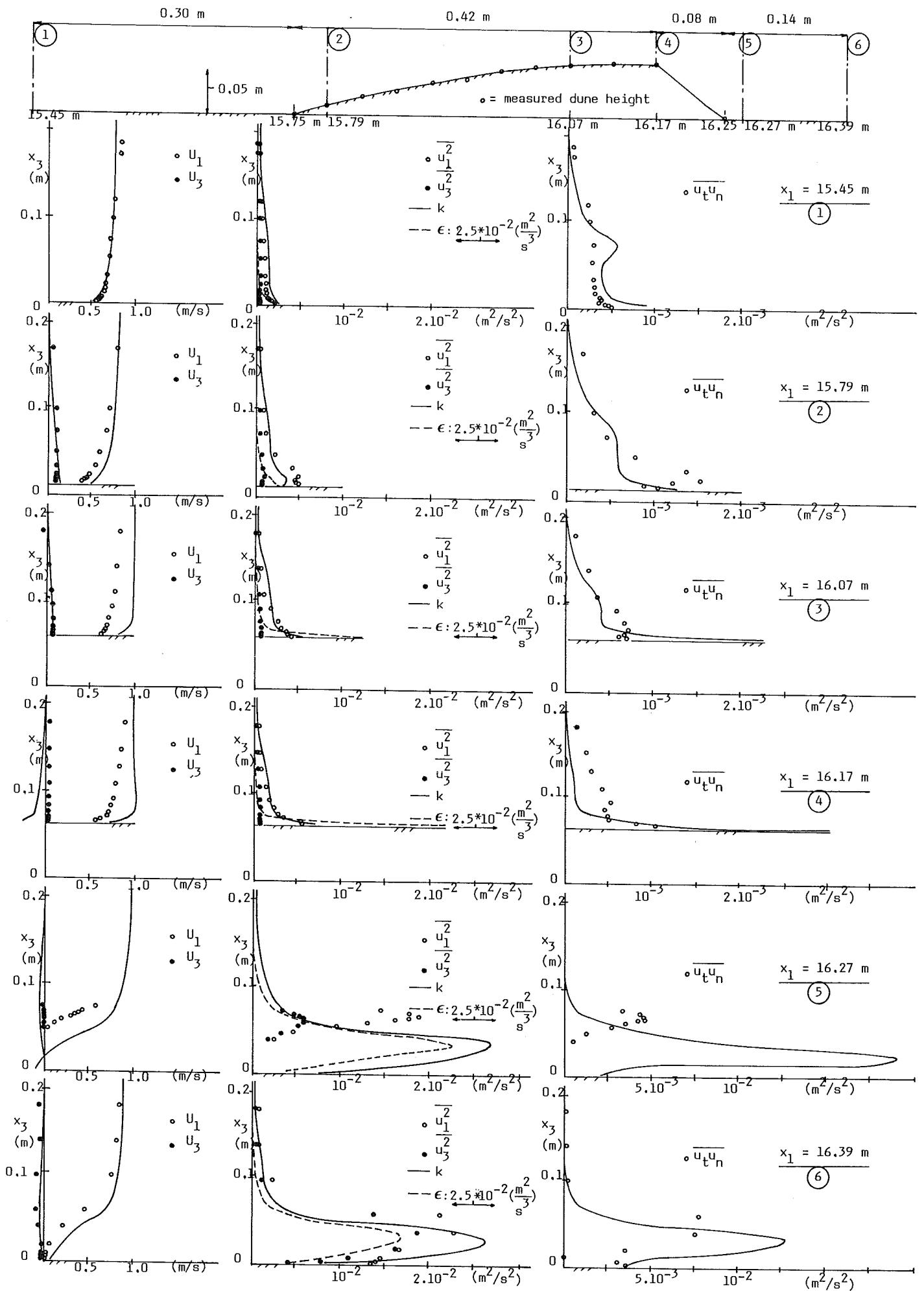


Figure 4.14 : Results of experiment T2 (\circ , \bullet), compared with numerical results of ODYSSEE (—, ---).

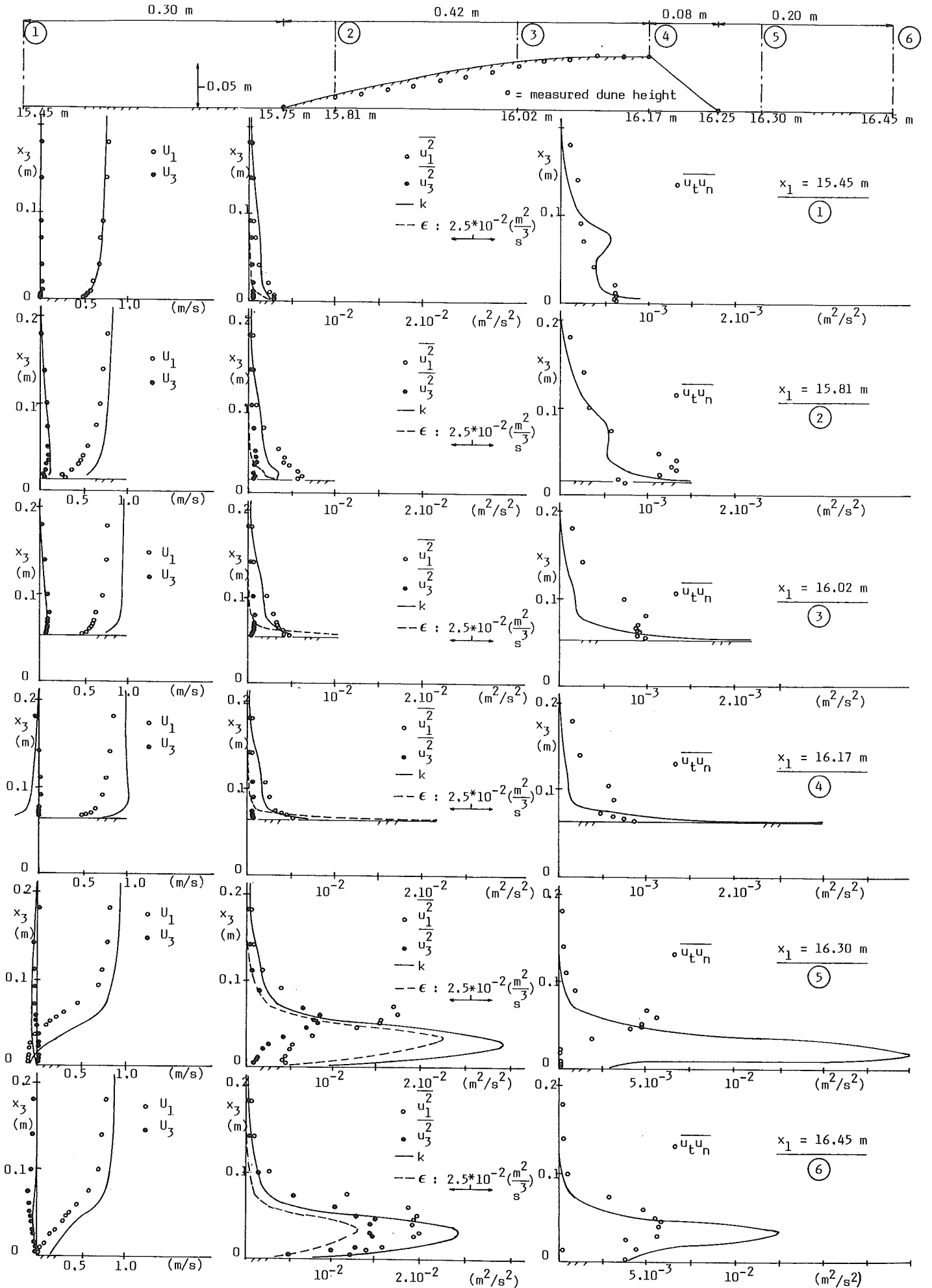
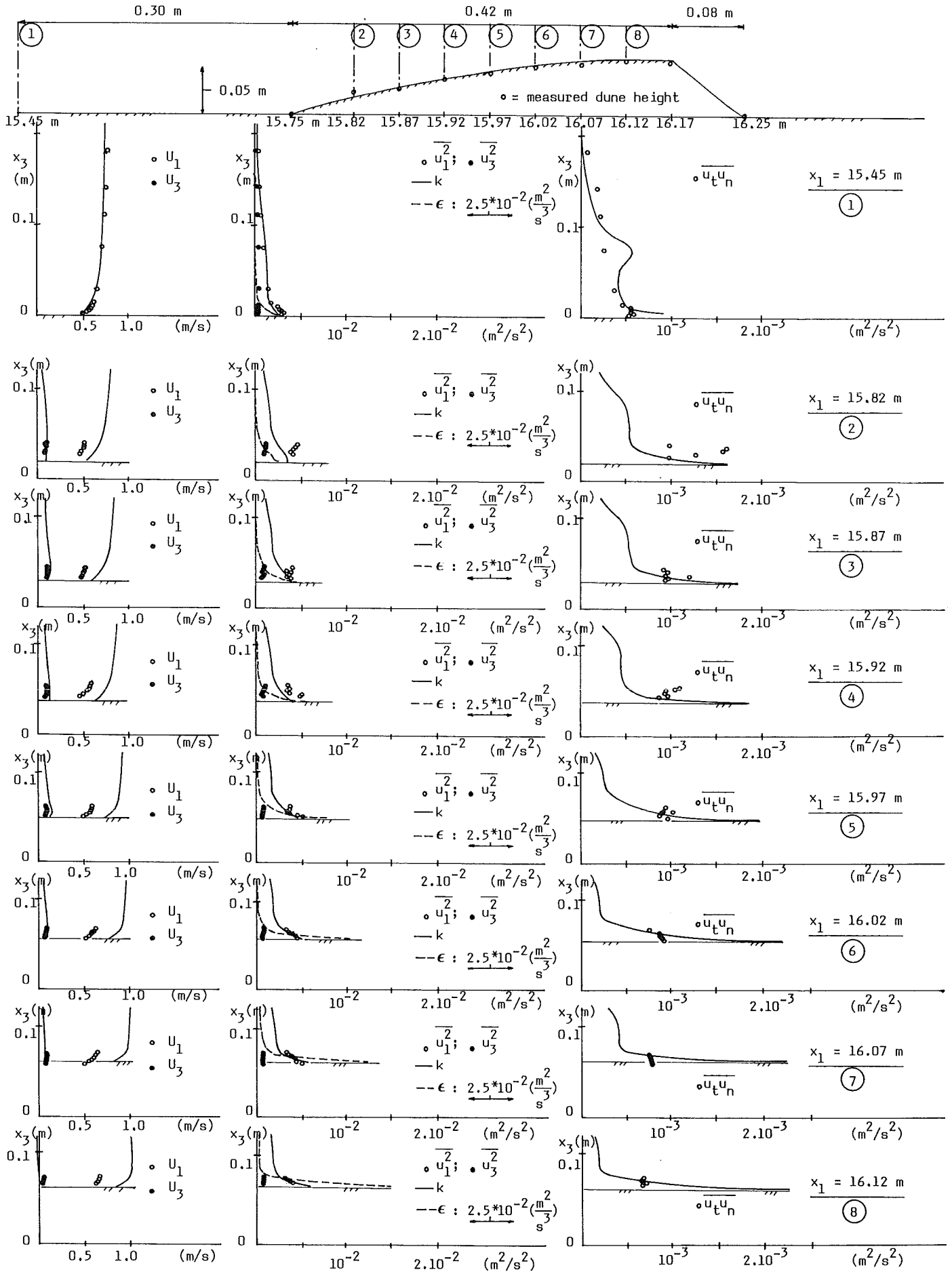


Figure 4.15 : Results of experiment T3 (\circ, \bullet), compared with numerical results of ODYSSEE (—, ---).



Below the dune three plots with values for (U_1, U_3) , $(\overline{u_1^2}, \overline{u_3^2}, k, \epsilon)$ and $-\overline{u_t u_n}$ per cross-section are presented next to each other.

Vertically the profiles per flowquantity progressing downstream can be compared.

The measured flowvelocities and turbulent energies are given in the x_1 - and x_3 -direction. The measured values of $\overline{u_1^2}$ and $\overline{u_3^2}$ are only part of the total turbulent energy $k = \frac{1}{2}(\overline{u_1^2} + \overline{u_2^2} + \overline{u_3^2})$, which is given by the program.

The $\overline{u_2^2}$ -component could not be measured as even as ϵ , the calculated ϵ is given as an indication.

The Reynoldsshearstress $-\overline{u_t u_n}$ is given as the shearstress along a streamline, with t perpendicular to the streamline and n normal to the streamline.

The direction of the streamline is calculated as the angle α between U_1 and U_3 .

The direction of the streamlines in different points for measurements and calculation is given in appendix C.

From the measurements the Reynoldsshearstress is calculated with the relation:

$$-\overline{u_t u_n} = (\overline{u_1^2} - \overline{u_3^2}) \cdot \sin \alpha \cdot \cos \alpha - \overline{u_1 u_3} \cdot (2 \cos^2 \alpha - 1)$$

From the calculation the Reynoldsshearstress is calculated with the relation:

$$-\overline{u_t u_n} = \nu_t \cdot \partial u_t / \partial x_t, \text{ with } u_t = (\overline{u_1^2} + \overline{u_3^2})^{\frac{1}{2}}.$$

After these general remarks the results are treated more detailed.

For the three experiments the flowvelocity profile U_1 at the inflow boundary fits very well into the computed one.

For cross-sections above the dune the measured values are smaller than computed.

This is possibly caused by the three-dimensional flowfield in the experiments. Due to the perspex supports (see section 3.2) and the symmetrical but not uniform cross-section of the dune in the x_2 -direction, the flowfield is influenced.

Part of the water in the axis of the flume upstream the dune does not flow in the axis of the flume above the dune, so the specific discharge in the axis of the flume is not fulfilled in each cross-section.

The numerical slolution holds for a vertical plane, so here continuity for the specific discharge is fulfilled in each cross-section.

In the wake two problems occur: the wake in the calculation is not yet in equilibrium as explained before and the position of the cross-section in the measurements is not exactly determined.

So differences occur between calculated and measured profiles.

The turbulent energy profiles show that half the sum of $\overline{u_1^2}$ and $\overline{u_3^2}$ for the three experiments is not roughly equal to the calculated k , if the $\overline{u_2^2}$ is considered small (about the order of $\overline{u_3^2}$).

Further from the bottom the calculated value of k is large due to the disturbance in ϵ . Close to the bottom calculated values of k are high compared with the measured $\overline{u_1^2}$ and $\overline{u_3^2}$.

Upstream the dune a horizontal bed is present, so k is almost linear with the waterdepth, except near the bottom where k increases.

The measured Reynoldsshearstress $-\overline{u_t u_n}$ can not directly be compared with the calculated values, because of the difference in the direction of the streamlines in measurements and calculation.

However, a reasonable similarity can be seen between experiment and calculation.

The influence of the disturbance in ϵ on $-\overline{u_t u_n}$ is clear, but remains in the vertical position near $x_3 = 0.07$ m. Again the measured values do not fit the calculated values in the wake very well.

Considering the calculated flowquantities along the dune the next remarks can be made:

- The flowvelocity profile U_1 becomes steeper downstream near the bottom, this results in a higher value for u_* .

What causes the steep flowvelocity profile downstream is not clear, it can be an effect of convection.

In the program the boundary condition at the bottom fits a logarithmic profile, with a certain value of u_* , from the bottom to the first grid point. An increasing value of u_* results in a steeper profile.

- Due to the steep flowvelocity profile near the bottom resulting in a high value of u_* , the values of k and ϵ near the bottom are high as well. (equations 4-9)
- Due to the steep flowvelocity profile the flowvelocity gradient near the bottom is high which results in high values of the Reynolds shear stress $-\overline{u_t u_n}$ (even though the turbulent viscosity is small near the bottom) near the bottom.

Considering the measured flow quantities along the dune the next remarks can be made:

- The steepness of the flowvelocity profile U_1 is different in each cross-section, but no specific trend is noticeable.
The values of u_* from the flowvelocity profiles along the dune show arbitrary differences, this is treated later.
- The shape of the turbulent energy profiles for $\overline{u_1^2}$ and $\overline{u_3^2}$ at $x_1 = 15.45$ m agree reasonably with the measured profiles in the experiment with the horizontal bed (sub-section 4.2.2).
Above the dune the shape of the profiles coincide for every cross-section, also the turbulent energies near the bottom do not differ considerably.
- The Reynolds shear stress at $x_1 = 15.45$ m is not linear with the depth as expected in case of a developed uniform flow.
This can be an effect of the disturbed flowfield upstream the dune due to the perspex supports.
The profiles coincide but show considerable variations in values, the bottom shear stress is for all cross-sections almost equal.

Computed and measured flow quantities along the dune surface:

For a better interpretation of flow quantities near the dune surface, these quantities are plotted along the dune surface.

Measurements are carried out at about $3 \cdot 10^{-3}$ m from the transport layer above the dune surface.

In the calculations the distance to the dune surface decreases downstream from $2 \cdot 10^{-3}$ m at the foot of the dune to $1.4 \cdot 10^{-3}$ m at the dune top, for the first grid line above the dune surface.

The next grid line is $4 \cdot 10^{-3}$ m from the dune surface at the foot of the dune and $2.8 \cdot 10^{-3}$ m at the dune top (see also figure 4.16).

Calculated flow quantities of both grid lines are used.

In figure 4.16 the mean flowvelocity, turbulent energy and Reynolds shear stress for T1, T2 and T3 are plotted and compared with calculated values.

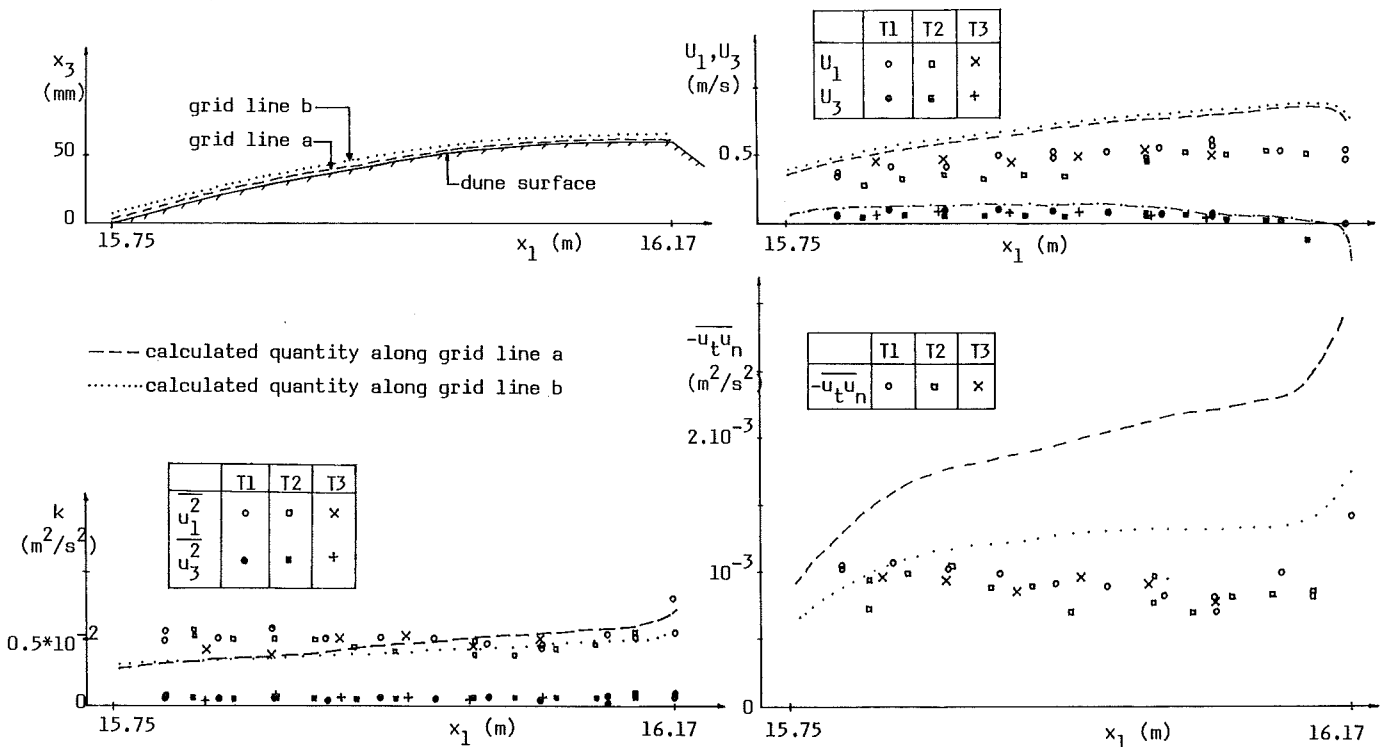


Figure 4.16: Flow quantities along the dune surface.

For the three experiments the measured values of the flowvelocity is smaller than the calculated values, which can be mainly an effect of the three-dimensional flowfield in the experiments. An increase of the flowvelocity for measured and calculated values downstream occurs.

Half the sum of the measured turbulent energy components $\overline{u_1^2}$ and $\overline{u_3^2}$ differs considerably from the calculated k . Even though the $\overline{u_2^2}$ -component is not known from measurements it can not be too large and certainly it is smaller than $\overline{u_1^2}$.

Near the foot of the dune the calculated value of k is even larger than the $\overline{u_1^2}$ -component alone.

The measured Reynoldsshearstress deviates strongly from the calculated values. Even the calculated values of $-\overline{u_t u_n}$ along the two stream lines differ strongly (about 50%). This is an effect of the steep flowvelocity profile.

The measured values of $-\overline{u_t u_n}$ along the dune surface slightly decrease downstream, the calculated values of $-\overline{u_t u_n}$ increase downstream.

The high values of $-\overline{u_t u_n}$ from measurements and calculation at the dune top is an effect of the wake, which has its influence already near the dune top (due to high shearstresses in the wake).

Some general reasons for the difference between the calculated and measured flowquantities and the behaviour of the measured quantities above the dune are:

- The flowfield is three-dimensional in the experiments, due to the perspex supports.
- The stream lines in the experiment and in the calculation differ, so comparison of Reynoldsshearstresses is troublesome.
- The size of the measuring volume L2 affects the turbulent quantities near the bottom (in a region of about 1 cm from the bottom). Measured values of $\overline{u_1^2}$, $\overline{u_3^2}$ and $-\overline{u_t u_n}$ are less than expected (as pointed out in sub-section 3.4.3). However, in this situation it is unknown what the shearstress near the bottom should be, only the bedshearstress can be estimated from the logarithmic part of the flowvelocity profile, which is in this case not accurate enough (see also figure 4.17).
- The position of the dune surface is not accurately known. Definition of the dune surface is troublesome due to the transport layer with moving sand particles. This inaccuracy has great influence on the determination of u_* from the logarithmic part of the flowvelocity profile. A minor difference in vertical position results in considerable differences in the flowvelocity due to the steepness of the flowvelocity profile.
- The moving sand particles in the transport layer influence the flowquantities just above the dune surface. The transport layer is like a moving wall which makes the wall smoother, but on the other hand the flow provides the sand particles with kinetic energy. From the measurements it follows that the Reynoldsshearstress is almost constant along the dune surface.

Finally u_*^2 calculated from the logarithmic part of the flowvelocity profile is compared with u_*^2 from the $-\overline{u_t u_n}$ profile. This is done both for measurements and calculation.

The correlation between u_*^2 from the U-profile and the $-\overline{u_t u_n}$ profile should be one.

The relation is presented in figure 4.17.

For the measurements the correlation is weak.

The values from the calculation are correlated, but u_*^2 from the $-\overline{u_t u_n}$ profile is consequent higher than u_*^2 from the U-profile.

It is mentioned that in both cases the used values from the $-\overline{u_t u_n}$ profile are not the bottomshearstresses, but values of $-\overline{u_t u_n}$ close to the bottom.

Known values as close as possible to the bottom are used, so figure 4.17 is of minor importance.

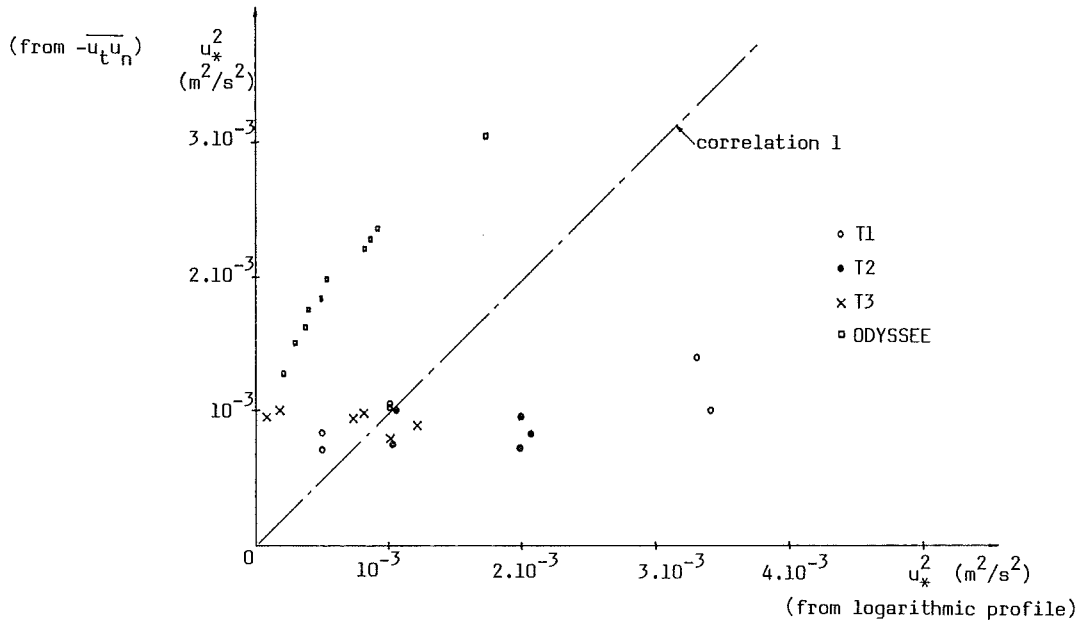


Figure 4.17: Correlation u_*^2 from log-profile and bedshearstress.

4.3 Sedimentmovement

4.3.1 General

The sediment transport can be calculated accurately if the conveyor belt velocity c_b and the local dune height $z_b(x_1)$ are known.

The relation between the local sediment transport S and the local Reynolds shearstress $-\overline{u_t u_n}$ is studied. No comparison took place with existing transport models.

The calculated shearstress is not regarded, because of the difference with the measured shearstress.

Furthermore the measured shearstress is logically related to the local sediment transport, in the calculation no transport occurred.

4.3.2 Sediment transport

In the experiments T1, T2 and T3, three different dune shapes occurred with three different conveyor belt velocities, which are presented in the figures 4.13, 4.14 and 4.15.

The local sediment transport along the dune surface is presented in figure 4.18.

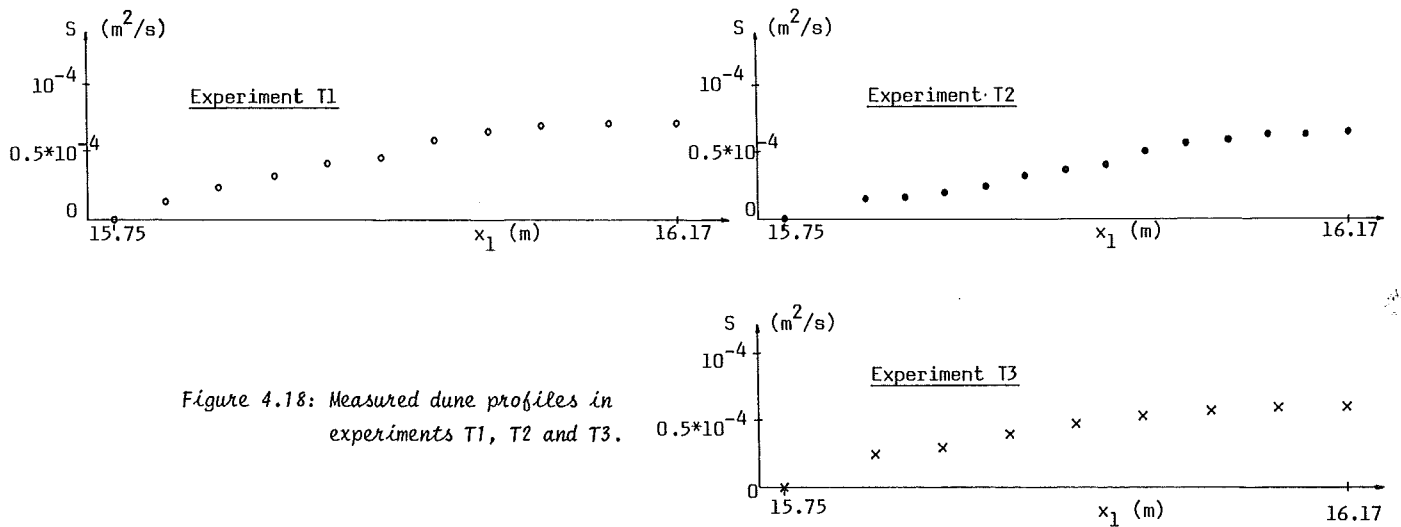


Figure 4.18: Measured dune profiles in experiments T1, T2 and T3.

The local sediment transport can easily be deduced from equation (2-57), where for an equilibrium situation $\partial z_b / \partial t = 0$, so the remaining expression reads:

$$\frac{\partial}{\partial x_1} (S - c_b \cdot z_b) = 0$$

After integration over x_1 and with the boundary condition at $x_1 = 0$; $S = 0$, the result is

$$S(x_1) = c_b \cdot z_b(x_1) \tag{4-10}$$

The transport is proportional to the shape of the dune. It is mentioned that the local sediment transport is a mean local transport, instantaneous transports could not be determined.

4.3.3 Sediment transport and flow quantities

In this sub-section the local sediment transport and the measured local flow quantities are related. A first indication of the relation transport-flowfield is presented in figure 4.16. The mean flow velocity and the turbulent energy, however, are less important to be related directly to the local sediment transport. An important flow quantity is the Reynolds shear stress which directly governs the sediment transport. The Reynolds shear stress is in fact transporting energy from the main flow to turbulence, but in this case also transports energy to the sand particles, which gain kinetic energy. In figure 4.19 the local sediment transport S is plotted versus the local Reynolds shear stress $-\overline{u_t u_n}$ for T1, T2 and T3.

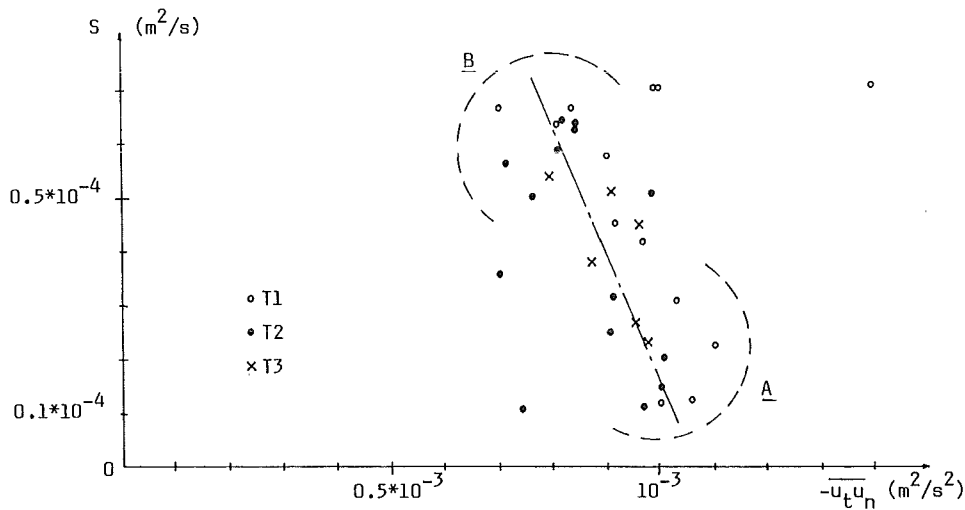


Figure 4.19: Relation of local sediment transport S and local Reynolds shear stress $-\overline{u_t u_n}$.

The transport and shear stress at the foot of the dune are plotted in area A and values near the dune top are plotted in area B. From the figure it follows that a small transport and large shear stress coincide as well as a large transport and a small shear stress ! This is not commonly found in literature. Before the results are treated further, first some results from literature are presented.

Raudkivi (1976) carried out measurements above a series of solid dunes, which is also treated in (---, DHL, 1981). Puls (1981) also gives results of measurements and calculations of shear stresses above a series of solid dunes. In figure 4.20 results from literature above solid dunes are presented.

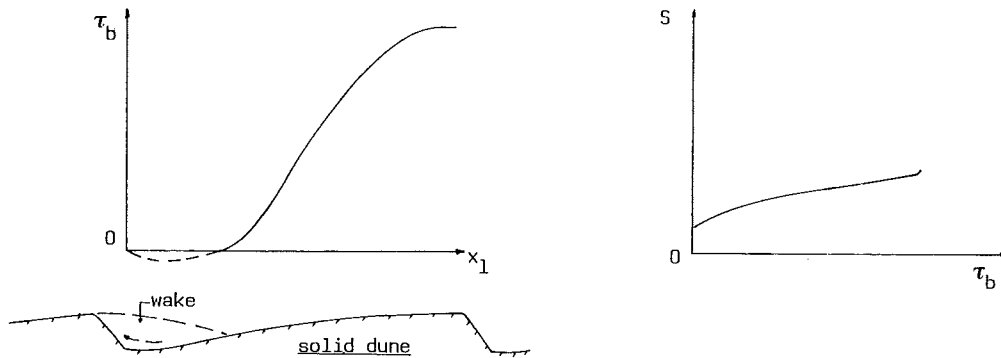


Figure 4.20: Shearstress over a solid dune and S versus τ_b , qualitative plots (from --, DHL, 1981).

The transport (deduced from the dune shape) is increasing with increasing shearstress follows from figure 4.20. The rate of increase of S with $-\overline{u_t u_n}$ is decreasing for large values of S , because the shape of the dune becomes almost horizontal near the dune top.

The shape of $S = f(-\overline{u_t u_n})$ in figure 4.20, disagrees with the shape presented in figure 4.19.

Reasons for the similarity are already mentioned at the end of sub-section 4.2.3, but a possible reason can be added:

- Near the foot of the dune the sand particles have to be accelerated from velocity zero to a certain value (area A in figure 4.19).

This demands a large shearstress, also because the slope of the dune is steep near the foot.

Once moving the sand particles lose kinetic energy due to collisions with other particles in and below the transport layer, but less energy is needed to keep them moving compared to the particles near the foot of the dune (area B in figure 4.19).

Also the slope of the dune decreases near the top of the dune.

Considering the dune, more particles are moving going downstream from foot to top of the dune, the transport increases.

So for this effect extra shearstress is needed to accelerate more sand particles further downstream.

So downstream the foot of the dune a decreasing shearstress is expected due to sand particles with a certain kinetic energy, on the other hand further downstream the foot of the dune more sand particles are moving so the shearstress must increase.

Which effect is most important is not answered here, but from the experiments it is clear that the shearstress near the dune surface along the dune is almost constant.

4.4 Recapitulation

4.4.1 Horizontal bed situation

The results of the measurements agree very well with theory.

The measured flowvelocity profile, turbulent shearstress profile and power spectra fit theoretical profiles satisfactory.

Near the bottom there is some influence of the size of the measuring volume of the LDA (in a region of about 1 cm from the bottom), so the measured shearstress occurs to be smaller than expected.

The shearstressvelocity u_* calculated from the logarithmic part of the flowvelocity profile fits theory, and the extrapolated shearstress gives a bedshearstress which fits the theoretical value of u_* as well.

The influence of the convergent flow is minor but noticeable.

As a test for the LDA this experiment is successful and a valuable preparation for the measurements in the solitary dune situation.

4.4.2 Solitary dune situation

The results of the measurements can be compared reasonably well with the results of the calculation with the computer program ODYSSEE.

An important relation between the local sediment transport and the measured local Reynolds shear stress gives a troublesome picture (see figure 4.21).

The relation found in literature above solid dunes differs strongly from the relation found in the experiments (see figure 4.21).

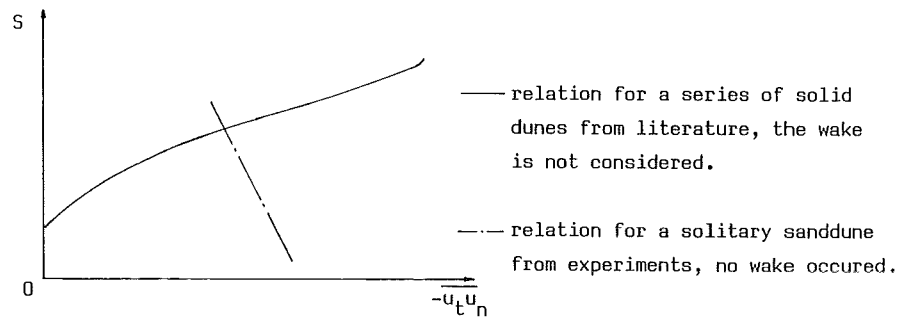


Figure 4.21: Principle of $S = f(-\overline{u_t u_n})$ for a solid dune (literature) and a sanddune (experiments), the relations are qualitative.

The reasons for the weak agreement between the results for a series of solid dunes and a solitary dune with a transport layer are:

- In the experiments a three-dimensional flowfield occurred.
- The measuring volume L_2 of the LDA provides smaller values of the measured Reynolds shear stresses near the bottom.
- The position of the measuring volume is inaccurately determined with respect to the dune surface.
- The moving sand particles in the transport layer above the dune create a moving wall, which is smooth with respect to a rigid wall.
- The sand particles near the foot of the dune have to be accelerated which demands a high shear stress. Once moving the sand particles need less shear stress to keep them moving, but more sand particles are moving downstream the foot of the dune, so for this effect an increasing shear stress is required.
- The kinetic energy transported by $\overline{u_t u_n}$ to the sand particles results in less energy for the flowfield. However, the moving sand particles create a smooth wall, which has its effect on the flow quantities.

All these effects can not be detected separately from the results of the measurements.

Finally it is mentioned that in the experiments a horizontal bed upstream the dune is present, so at the foot of the dune a high shear stress occurs.

In a series of dunes a wake is present near the foot of the dune, so the shear stress is small (negative or even zero).

The wake, however, plays an important role in the sediment transport phenomena.

An experiment with wakes and moving sand particles should be carried out to study the mechanism of local sediment transport in a more natural situation.

But first a two-dimensional flow situation with a solitary dune should be created, to determine the influence of moving sand particles on the Reynolds shear stress along the dune surface.

5. Recommendations

5.1 Introduction

During the investigations of water movement and sediment transport as described in this report, a first attempt is made to investigate the mechanism of local sediment transport with the experimental set up described in section 3.2.

The conveyor is especially designed for the experiments and under certain flow conditions a stable solitary dune is created which satisfies the demands.

The LDA is adapted for the experiments and showed to be satisfactory accurate, in an experiment in a flume with a horizontal bed.

The measurements in the solitary dune situation are not too comprehensive, but showed that measurements above the dune with moving sediment are possible.

The results of the measured flowfield above the dune are satisfactory.

To understand the mechanism of local sediment transport, however, comprehensive measurements in a solitary dune situation are necessary.

In this chapter recommendations for the experimental set up and measuring equipment are given, as well as for further experimental and theoretical research.

5.2 Solitary dune

In the solitary dune situation a stable dune is created by adapting the flowfield just upstream the conveyor. The flow upstream the dune appeared to be asymmetric which created a strongly asymmetric dune.

By partly blocking the space between glass walls and perspex supports the dune is made nearly symmetric. Adapting the flowfield made the flow and the water surface whirly.

The dune is reasonably symmetric and stable due to the whirly flow pattern and eddies generated by the perspex supports.

For further experiments the flowfield should be symmetrical just after the inflow section of the flume, so a completely developed symmetrical flowfield appears at the measuring section.

The measuring section in the flume should be so far downstream the inflow section, that a completely developed boundary layer flow is present.

The walls and bottom of the flume should be very plane, the present flume contains joints in the walls and bottom which influence the roughness in an undefined way.

The position of the solitary dune on the conveyor must be constant.

The measurements last at least 8 hours and during the experiments it appeared that the complete dune sometimes moves over about 5 to 10 cm in 2 to 4 hours, the shape is not much affected.

The velocity of the conveyor belt is increased or decreased temporarily to move the dune to the right position again and the measurements can carry on.

It is, however, advisable to prevent movements of the complete dune and to adjust the velocity of the conveyor belt very accurately.

5.3 Measuring equipment

The results of measurements with the LDA are satisfactory, the L1 measuring volume, however, gave poor results.

It can be recommended to use lenses of high quality and to adjust the LDA very accurately.

Then it is possible to create a real L1 measuring volume and the accuracy of the results increases with respect to the L2 measuring volume.

The laser beam should pass the rotating grating perpendicularly, otherwise the angles between the illuminating beam and the two reference beams are not equal.

When this demand is not fulfilled, the 45° configuration is not present and errors of 5 to 10 % can occur in the results.

In general the angle between the reference beams and the illuminating beam should be measured accurately after every adjustment of the beams, in order to calculate the proper conversion factor.

The vertical position of the measuring volume in the experiments is read from a scale, with an accuracy of 0.5 mm.

Near the bottom of the flume or near the dune surface the flowvelocityprofile is very steep, so a small error in the vertical position results in a large error in the flowvelocity.

It is recommended to use an electronic scale for the determination of the vertical position of the measuring volume.

With this device the vertical position can be adjusted accurately and reproducibly.

The scale must be gauged with respect to a determined fixed point in the flume.

5.4 Experiments

For a complete insight in the interaction between water movement and local sediment transport a series of experiments is needed, in which flow conditions are varied.

Different flow conditions create different dune shapes and propagating velocities of the solitary dune.

Also different grain sizes or a mixture of grain sizes can be used.

A quantity which is used in the DUGRO program (de Ruiter, 1981) is the standard deviation of the Reynolds-shear stress, as pointed out in figure 5.1.

This quantity can be calculated easily from the measured data.

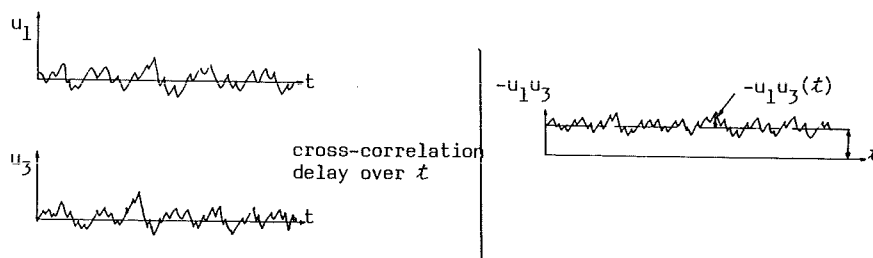


Figure 5.1: Definition of standard deviation of Reynolds shear stress in time.

To investigate the influence of the moving sand particles, an experiment with a solid dune could be carried out with the same flow conditions as in the solitary dune situation.

The shape of the solitary dune can be measured and a solid dune of the same shape can be placed in the flume instead of the sand dune.

An advantage is that the local sediment transport is known from the solitary dune situation (the sand dune).

Another way to investigate the influence of the moving sand particles on the flow quantities near the dune surface, is to reduce the flow velocity so the shear stress decreases and the sand particles just do not move. When the local Reynolds shear stress in both cases (moving and not-moving sand particles) is made dimensionless in a convenient way (dividing by the local value of u_*^2) the results can be compared.

The simplest way to investigate the effect of moving sand particles is an experiment with moving sand particles over a horizontal bed.

Comparison of Reynolds shear stresses in case of a rigid horizontal bed and a bed with moving sand particles shows the influence for a horizontal bed.

The disadvantage of the solitary dune is that the situation deviates strongly from a natural situation, a series of dunes.

To create a situation which is more realistic with respect to the situation in nature, it is useful to try to create two dunes on one conveyor, as sketched in figure 5.2.

In this set up a wake occurs upstream the second sand dune, which is essential in a natural situation.

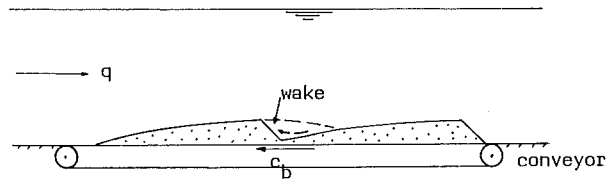


Figure 5.2: Two sanddunes on a conveyor.

5.5 Theory

The investigation described in this report mainly considered the water movement above a solitary dune. Theoretical or empirical models for the local sediment transport are not studied. For further investigations, however, it is essential to study theoretical and empirical models and experimental results of sediment transport over dunes.

Mean flow velocities and turbulent energy seem to be insufficient to be related to local sediment transport.

A more important quantity is the Reynolds shear stress and of great importance is the influence of moving sand particles along the bed on the Reynolds shear stress.

Power spectra and correlation functions are convenient to get insight in the structure of the turbulent quantities of the flowfield.

Knowledge of the influence of convection on the flow quantities is important with respect to estimates of shear stress velocities (u_*) from the logarithmic part of the mean flow velocity profile and with respect to the turbulent energy and Reynolds shear stress profiles.

Furthermore a sufficient knowledge of the $k-\epsilon$ model is required when the ODYSSEE program is used.

Symbols

a	local waterdepth, with subscript: 1 coefficient 2 coefficient e equilibrium waterdepth	H_s	bottomstep height
A	total area cross-section with subscript: b area with bottom influence w area with wall influence	i	integer, complex number, with subscript: E slope of energy line
A(II)	coefficient	j	integer
B	flume width	k	integer, wavenumber, turbulent energy ($\frac{1}{2}\overline{u_1 u_1}$), with subscript: b bottom roughness b wavenumber where influence viscosity starts e wavenumber at maximum spectrum w wall roughness
c	fluctuation of concentration, or correlation coefficient, with subscript: b conveyor belt velocity D empirical coefficient f drag coefficient s empirical coefficient 1E empirical coefficient 2E empirical coefficient μ empirical coefficient	l	wavenumber in x_1 -direction
\hat{c}	instantaneous concentration	K	non-linear dune celerity
C	mean concentration, with subscript: b bottom roughness (Chézy) B coefficient o concentration of dune w wall roughness (Chézy)	K'	non-linear dune celerity
c(t)	correlation function, with subscript: 1 auto-correlation function u_1^2 3 auto-correlation function u_3^2 13 cross-correlation function $-u_1 u_3$	K''	non-linear term
D_E	Euler dissipation scale	L_f	integral scale
D_f	dissipation scale of integral scale	m	coefficient
dx_1	infinitesimal distance in x_1 -direction	M	constant ($m \cdot q^n / c_b$)
dx_2	infinitesimal distance in x_2 -direction	n	integer, power, direction normal to streamline
dx_3	infinitesimal distance in x_3 -direction	N	total number of values in a measured discrete signal
E	coefficient	p	fluctuating pressure
$E_1(k_1)$	power spectrum of u_1^2	\hat{p}	instantaneous pressure
$E_3(k_1)$	power spectrum of u_3^2	P	mean pressure
$E_{13}(k_1)$	power spectrum of $-u_1 u_3$	$p(x_1)$	function describing equilibrium duneshape
f_B	burst frequency	q	specific discharge
f_1	lower boundary BPF	Q	total discharge
f_{j+1}	Fourier transform of F_{j+1} (time domain)	r	distance
Fr	Froude number ($\overline{U_1} / (g \cdot a)$)	R	hydraulic radius, with subscript: b hydraulic radius of bottom w hydraulic radius of wall
F_{j+1}	Fourier transform of f_{j+1} (freq. domain)	Re	Reynoldsnumber
$f(r)$	spatial correlation	s	fluctuating sediment transport
$f(..)$	function of ..	\hat{s}	instantaneous sediment transport
g	gravity	S	mean sediment transport
\vec{g}	gravity vector (0,0,-g)	t	time, direction tangent to streamline, with subscript: e equilibrium time 0 starting time l time
h	waterlevel with respect to $x_3 = 0$	T	temperature, measuring time
H	local dune height	T_E	Euler integral scale time scale
H'	transport layer thickness	u_A, u_B	flowvelocity in point A respectively point B
		u_i	fluctuating flowvelocity
		u_1, u_3	fluctuating flowvelocity in x_1 -, x_3 -direction
		u_*	shearstress velocity
		u_i	instantaneous flowvelocity
		$u_{1, 0_3}$	instantaneous flowvelocity in x_1 -, x_3 -direction
		U	with subscript: e equilibrium local mean flowvelocity i mean flowvelocity o flowvelocity outer layer, critical flowvelocity t mean flowvelocity tangent to streamline l mean flowvelocity in x_1 -direction

U	with subscript:	ν	molecular viscosity, frequency, with subscript:
3	mean flowvelocity in x_3 -direction		t turbulent viscosity
le	mean flowvelocity at t_e	Π	pressure parameter
lo	mean flowvelocity at t_o	ρ	density, with subscript:
ll	mean flowvelocity at t_l		s density of sand
U_1^+	dimensionless mean flowvelocity		w density of water
\bar{U}_1	depth averaged mean flowvelocity in x_1 -dir.	$\sigma_k, \sigma_\epsilon$	emperical constant
\vec{U}	flowvelocity vector	τ_{fil}	filtered shearstress
$\frac{u_1^2}{2}$	turbulent energy	τ_{ij}	shearstress vector
$\frac{u_1^2, u_2^2, u_3^2}{2}$	turbulent energy in x_1 -, x_2 -, x_3 -direction	τ_o	non-filtered shearstress
$-\frac{u_1 u_n}{t_n}$	Reynoldsshearstress in t,n-plane	τ_{13}	Reynoldsshearstress in x_1, x_3 -plane
$-\frac{u_1 u_3}{t_3}$	Reynoldsshearstress in x_1, x_3 -plane	$\vec{\tau}$	shearstress vector
$u_1^2(t)$	auto-correlation function of u_1^2	$\frac{\tau_b}{\tau_o}$	mean bottom shearstress
$-u_1 u_3(t)$	cross-correlation function of $-u_1 u_3$	$\frac{\tau_o}{\tau_w}$	mean overall shearstress
ϕ_1, ϕ_2	instantaneous flow velocity vector		mean wall shearstress
$W(x_3/a)$	wake function		
x_i	coordinate		
x_1, x_2, x_3	coordinate		
x_3^+	dimensionless coordinate		
z	with subscript:		
o	bottom roughness		
0	reference level		
1	level with respect to z_0		
2	level with respect to z_0		
3	level with respect to z_0		
z_b	local dune height		
z_{be}	equilibrium local dune height		
$\partial a / \partial x_1$	watersurface slope		
%SF _b	percentage of bottom shearforce		
%SF _w	percentage of wall shearforce		
ℓ	integral length scale		
ℓ^+	dimensionless integral length scale		
L	length scale		
O(..)	order of ..		
P	production of turbulent energy		
t	delay time		
ν, ν	flowvelocity scale		
α	angle		
α_b	angle of boundary layer development		
β	angle		
γ	angle		
δ	boundary layer thickness with subscirpt:		
b	viscous layer thickness of bottom		
w	viscous layer thickness of wall		
Δ	normalized boundary layer thickness		
Δt	time interval		
ϵ	dissipation rate of turbulent energy		
η	Kolmogorov length scale		
η^+	dimensionless Kolmogorov length scale		
κ	von Kármán constant		

Literature

- Abramowitz, M., Stegun, I.A.
Handbook of mathematical functions
Dover Publ. Inc., New York, 1965
- Alfrink, B.J., Officier, M.J., Vreugdenhil, C.B.,
Wind, H.G.
Applications in hydraulics of a curvilinear
finite-difference method for the Navier-Stokes
equations
DHL, Delft, 1983
- Blackman, R.B., Tukey, J.W.
The measurement of power spectra
Dover Publ. Inc, New York, 1959
- Bradshaw, P., Wong, F.Y.F.
The reattachment and relaxation of a turbulent
shear layer
J. Fluid Mech., vol. 52, 1972, pp. 113-135
- Brigham, E.O.
The fast fourier transform
Prentice Hall Inc., New Jersey, 1974
- Dronkers, J.
Correlation between fluctuations of the sali-
nity and the horizontal current velocity in
a partially mixed estuary
RWS, The Hague , 1983
- Durrani, T.S., Greated, C.A.
Laser systems in flow measurement
Plenum Press, New York, 1977
- Durst, F., Melling, A., Whithelaw, J.H.
Principles and practice of laser-doppler
anemometry
Academic Press, New York, 1976
- Etheridge, D.W., Kemp, P.H.
Measurements of turbulent flow downstream
of a rearward-facing step
J. Fluid Mech., vol. 86, 1978, pp. 545-566
- Evers, D.J.W.M, Huigen, G., Welling, W.A.
Laser doppler snelheidsmetingen, signaalverw.
PT-werktuigbouw, 2, 1983, pp. 71-75 (in dutch)
- Fredsg e, J.
Shape and dimensions of stationary dunes in
rivers
J. of Hydraulic division ASCE, vol.108, HY8,
1982, pp. 932-947
- Haque, M.I., Mahmood, K.
Analytical determination of form friction factor
J. of Hydraulic division ASCE, vol.109, HY4,
1983, pp. 590-610
- Hinze, J.O.
Turbulence
McGraw-Hill Int. Book co., London, 1975
- Knight, D.W.
Boundary shears in smooth and rough channels
J. of Hydraulic division ASCE, vol.107, HY7,
1981, pp. 839-851
- Launder, D.E., Spalding, D.B.
Mathematical models of turbulence
Academic Press, New York, 1972
- Menzel, D.H. (ed.)
Fundamental formulas of physics (2 vol.)
Dover Publ. Inc., New York, 1960
- Papoulis, A.
Probability, random variables and stochastic
processes
McGraw-Hill Int. Book co., London, 1982
- Prandtl, L, Tietlens, O.G.
Fundamentals of hydro- and aeromechanics
Dover Publ. Inc., New York, 1957
- Prins, A.
Sedimenttransport, f10
TH, Delft, 1981 (lecture notes in dutch)
- Puls, W.
Numerical solution of bed form mechanics
Mittenburger des Instituts f ur Meereskunde der
Universit t Hamburg, nr. 24, 1981
- Raudkivi, A.J.
Loose boundary hydraulics
Pergamon Press, Oxford, 1976
- Ribberink, J.S.
Experiments with non-uniform sediment in case of
bed-load transport
Delft University of Technology, report no. 83-2, 1983
- van Rijn, L.C.
Siltation in dredged trenches,
Two-dimensional mathematical flow model with a
two-equation turbulence closure, S 488 part I
DHL, Delft, 1983,

Rodi, W.
Turbulence models and their applications in
hydraulics
IAHR, Delft, 1980

de Ruiter, H.
Dugro, R 657 - XXIX
DHL, Delft, 1981

Schlichting, H.
Boundary layer theory
McGraw-Hill Int. Book co., London, 1979

Tennekes, H., Lumley, J.L.
A first course in turbulence
The MIT Press, Cambridge, 1977

Verhagen, C.J.D.M.
Systemen en signalen I, c19
TH, Delft, 1981 (lecture notes in dutch)

Verspuy, C., de Vries, M.
Lange golven I & II (2 vol.), b73
TH, Delft, 1981 (lecture notes in dutch)

Vreugdenhil, C.B.
Waterloopkundige berekeningen II, b85
TH, Delft, 1981 (lecture notes in dutch)

Vreugdenhil, C.B.
Boundary layer flow over a sloping bottom, S 488 II
DHL, Delft, 1982

de Vries, M.
Inleiding vloeistofmechanica, b71
TH, Delft, 1979 (lecture notes in dutch)

de Vries, M.
Vloeistofmechanica, b72
TH, Delft, 1980 (lecture notes in dutch)

de Vries, M.
Morphological computations, f10A
TH, Delft, 1981 (lecture notes)

Weast, C. (ed.)
CRC handbook of chemistry and physics, 63rd ed.
CRC Press Inc., Boca Raton Florida, 1982

Welling, W.A.
De laser doppler methode
PT-werktuigbouw, 12, 1982, pp. 72-75 (in dutch)

Weyl, H.
Space-time-matter
Dover Publ. Inc., New York, 1952

Whitham, G.B.
Linear and nonlinear waves
John Wiley & Sons, New York, 1972

-- , DHL
Watermovement over a dune-covered river bed,
R 657 - XXX
DHL, Delft, 1981

appendix A

Operation of the Laser Doppler Anemometer, heterodyne system

contents:

Introduction

The doppler effect

Frequency pre-shift and diffraction

The measuring volume

Intensity due to moving particles in the measuring volume

Signal processing by a frequency tracker

The influence of glass walls on the measuring volume

Particles in the fluid

Two component flowvelocity measurements with the LDA

Resolution of flowvelocities

The overall LDA system

Overview of important formulas and data

A LDA heterodyne system in practice

List of symbols

Literature

Operation of the Laser Doppler Anemometer, heterodyne system

Introduction

The Laser Doppler Anemometer (LDA) is a very suitable apparatus for measurements of mean and turbulent flow quantities in fluids.

The principle of the LDA is based on the Doppler-effect which occurs when a light emitting body moves with respect to an observer.

When the body moves away from an observer then the observer sees the light at a lower frequency and when the body moves toward an observer the light is seen by the observer at a higher frequency.

So the frequency shift is a measure for the velocity of a body moving with respect to an observer.

With the LDA two or more light beams, generated by a laser, are made to intersect in an area of the fluid where the flow velocity and if desired some turbulent quantities are to be known.

At the intersection of the light beams a so called 'measuring volume' is created.

Small particles in the fluid passing through the measuring volume scatter the laser light and cause a frequency shift.

The scattered light is caught by a detector and its frequency shift measured.

The velocity of the particles is determined in this way and so indirectly the flow velocity.

The light beams passing through the fluid do not disturb the fluid, besides a negligible temperature rise.

The laser light must satisfy certain requirements which means in practice:

- a narrow light beam to create a small measuring volume,
- monochromatic laser light which has a narrow frequency band,
- the laser light must be coherent.

Two systems of measuring flow velocities with the LDA are the real fringe system and the heterodyne system.

The real fringe system

Two light beams of equal intensity intersect in the fluid. The light is scattered in all directions by particles moving through the measuring volume.

Outside the fluid in an arbitrary direction scattered light from the measuring volume is caught and concentrated on a photodetector.

The signal from the photodetector is converted to a flow velocity in the measuring volume. (See figure A-1)

This system is not treated further, extensive treatment of the system can be found in Durrani (1977).

The heterodyne system

Two light beams of unequal intensity intersect in the fluid. The beam with high intensity is called the illuminating beam, the beam with low intensity is called the reference beam.

Scattered light, of the illuminating beam, by particles moving through the measuring volume, is mixed (heterodyned) with light of the reference beam.

The reference beam is directly projected on a photodetector.

The signal from the photodetector is converted to a flow velocity in the measuring volume. (See figure A-1)

This system is treated further.

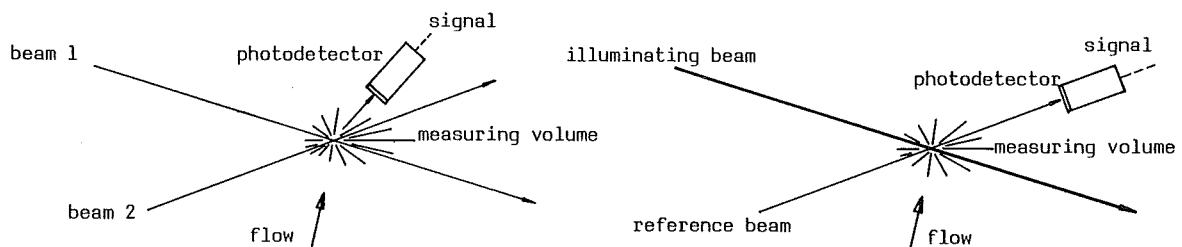


Figure A-1: Principle of the real fringe system (left) and the heterodyne system (right).

The doppler effect

Light radiated by a body which moves away from an observer with a velocity U_o , is seen by the observer with a frequency (Menzel,1960):

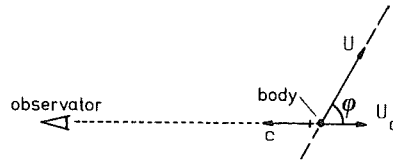
$$\nu = \nu_o \cdot (1 - U_o/c) \tag{a-1}$$

The number of lightwaves per unit time which reach the observer decreases when the body moves away, the total number of lightwaves however remains constant.

A body moving away from the observer in an arbitrary direction radiates light seen by the observer with a frequency:

$$\nu = \nu_o \cdot (1 - \cos \phi \cdot U/c) \tag{a-2}$$

In which ν_o is the undisturbed frequency of the light, and c is the velocity of light.



Formula (a-2) holds generally for velocities of the body much less than the velocity of light, $U \ll c$.

The frequency of light radiated by a body moving toward an observer in an arbitrary direction, is seen by the observer with a frequency:

$$\nu = \nu_o / (1 - \cos \phi \cdot U/c) \tag{a-3}$$

The illuminating beam and the reference beam create at their intersection a measuring volume in the fluid, as shown in figure A-2.

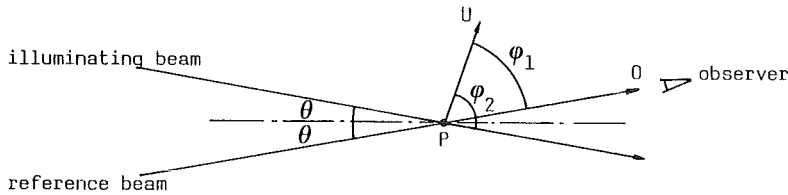


Figure A-2: Definition of the angles.

Assume a particle P in the fluid moves in the plane of the two beams through the measuring volume. The particle P sees the light from the reference beam and the illuminating beam with frequencies respectively:

$$\nu_{Pr} = \nu_o \cdot (1 - \cos \phi_1 \cdot U/c)$$

and
$$\nu_{Pi} = \nu_o \cdot (1 - \cos \phi_2 \cdot U/c)$$

An observer in O sees the light reflected by P from the reference and illuminating beam with frequencies:

$$\nu_{Oi} = \nu_o \cdot (1 - \cos \phi_1 \cdot U/c) / (1 - \cos \phi_1 \cdot U/c) = \nu_o \tag{a-4}$$

$$\nu_{Or} = \nu_o \cdot (1 - \cos \phi_2 \cdot U/c) / (1 - \cos \phi_1 \cdot U/c) \tag{a-5}$$

Formula (a-4) shows that there is no change in frequency of light from the reference beam in the direction of the beam, when a particle passes the beam.

An observer in O however does not see the light reflected by particles passing the measuring volume with frequencies described by the formulas (a-4) and (a-5), see figure A-3.

The two lightwaves interfere, the light of the reference beam is mixed with the light from the illuminating beam reflected by the particle P. This is called heterodyning.

The velocity of light is a constant, so $c = \nu_o \cdot \lambda_o = \nu_{Oi} \cdot \lambda_{Oi} = \nu_{Or} \cdot \lambda_{Or}$, with λ as the wavelength.

So a lightwave $\sin \nu_{Oi} \cdot t$ and a lightwave $\sin \nu_{Or} \cdot t$ are mixed and produce a new lightwave $(\sin \nu_{Oi} \cdot t + \sin \nu_{Or} \cdot t)$. The amplitude of the light signal is not regarded in this deviation.

This expression can be rewritten in: $(2 \cdot \sin \frac{1}{2}(\nu_{0i} + \nu_{0r})t \cdot \cos \frac{1}{2}(\nu_{0i} - \nu_{0r})t)$.
 Two new frequencies occur, one high frequency $\frac{1}{2}(\nu_{0i} + \nu_{0r})$ of order ν_0 and a beat frequency $\frac{1}{2}(\nu_{0i} - \nu_{0r})$.
 The high frequency is not of importance, but the beat frequency is of importance to determine the doppler frequency, see figure A-3.

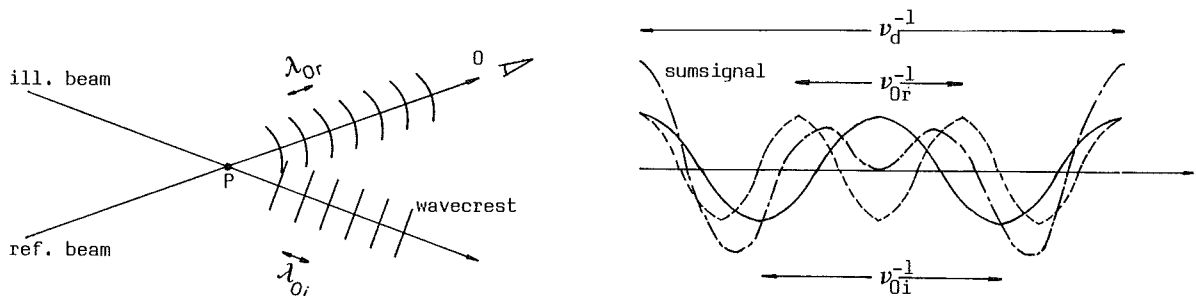


Figure A-3: Interfering lightwaves reflected by a particle P in the measuring volume.

Generally in O a photodetector is placed which is capable to detect only the beat frequency, the detector is not fast enough to detect the high frequency.
 The photodetector follows light intensities, whether the amplitude of the lightwave is positive or negative is not of importance.
 The photodetector thus sees a lightwave with twice the beatfrequency, this is called the doppler frequency:

$$\nu_d = \nu_{0i} - \nu_{0r} \tag{a-6}$$

This frequency is much smaller than ν_0 because of the slight difference between the frequencies ν_{0i} and ν_{0r} . (see the forthcoming example)

The intensity of the reference beam must be of the same order as the intensity of the lightwaves reflected by the particles in the measuring volume.
 A difference in intensity which is too great does not show the doppler frequency, this effect is pointed out in the next figure.

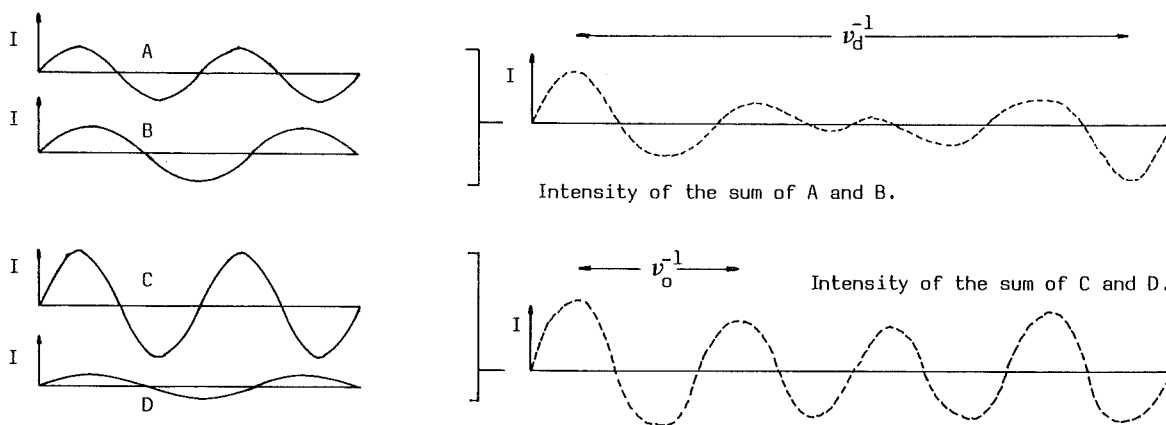


Figure A-4: Influence of intensities of lightwaves.

The laserlight must be monochromatic for reasons of interference. Light built up by many different frequencies does not generate a doppler frequency when interference occurs.
 Particles in the fluid which pass the lightbeams outside the measuring volume do not contribute to the doppler frequency.

Formulas (a-4) and (a-5) substituted in (a-6) give:

$$\nu_d = \nu_0 \cdot (\cos \varphi_1 - \cos \varphi_2) \cdot (u/c) / (1 - \cos \varphi_1 \cdot u/c) \tag{a-7}$$

The denominator of (a-7) is almost one compared with the nominator for flowvelocities of U occurring generally in fluids ($U/c \ll 1$).

So formula (a-7) reduces to:

$$v_d = v_o \cdot (\cos \varphi_1 - \cos \varphi_2) \cdot U/c \quad (\text{a-8})$$

The flowvelocity vector U can be expressed in a velocity vector U_b , which stands normal to the bisectrice of the angle between the two lightbeams.

U and U_b lie in the plane of the two beams.

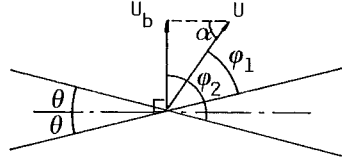


Figure A-5: Definition of velocity U_b .

The following equations hold:

$$\varphi_2 - \varphi_1 = 2\theta \quad \text{and} \quad \alpha = \frac{1}{2}(\varphi_1 + \varphi_2)$$

So $(\cos \varphi_1 - \cos \varphi_2) \cdot U = -2 \cdot \sin \frac{1}{2}(\varphi_1 - \varphi_2) \cdot \sin \frac{1}{2}(\varphi_1 + \varphi_2) \cdot U = 2 \cdot \sin \theta \cdot \sin \alpha \cdot U = 2 \cdot \sin \theta \cdot U_b$
Substituted in (a-8) with $c = v_o \cdot \lambda_o$ in which λ_o is the wavelength of the undisturbed lightbeam, gives:

$$v_d = 2 \cdot \sin \theta \cdot U_b / \lambda_o \quad (\text{a-9})$$

The constants λ_o and θ are known and v_d is known from measurements, so the flowvelocity U_b can be determined. U_b lies in the plane of the reference and illuminating beam.

The expression $2 \cdot \sin \theta / \lambda_o$ is called the optical transfer factor.

The doppler frequency is mixed with the light of the reference beam which has the frequency v_o .

The mixed lightbeam is projected on the photodetector.

Example to point out the simplifications and assumptions:

Data: $c = 3 \cdot 10^8$ m/s , $U = 3$ m/s , $\cos \varphi_1 = 0,8$, $\cos \varphi_2 = 0,3$, $v_o = 10^{14}$ Hz.

The nominator of formula (a-7) is: $5 \cdot 10^{-9}$ and the denominator is: $(1 - 8 \cdot 10^{-9})$

It is justified to simplify the denominator to one.

From equation (a-8) it follows that: $v_d = 5 \cdot 10^{-9} \cdot v_o = 5 \cdot 10^5$ Hz.

The photodetector can determine frequencies in the range of $5 \cdot 10^4$ Hz to $5 \cdot 10^6$ Hz, which does contain the doppler frequency but not the frequency v_o .

Frequency pre-shift and diffraction

The sign of the doppler frequency is not detected in the way described above, so a change of direction of U_b is not precieved.

A method to detect the direction of U_b is to add a frequency v_s . This can be done by preshifting the frequency of one beam , illuminating or reference beam, by v_s .

So the measured frequency reads:

$$v_{ds} = 2 \cdot \sin \theta \cdot U_b / \lambda_o + v_s \quad (\text{a-10})$$

The pre-shift frequency is constant and has a known value. The direction of U_b can be detected:

$$\begin{aligned} U_b > 0 & , \quad v_{ds} > v_s \\ U_b = 0 & , \quad v_{ds} = v_s \\ U_b < 0 & , \quad v_{ds} < v_s \end{aligned}$$

Adding v_s to v_d can be done in different ways; the method described here is based on diffraction due to a rotating grating.

The laserbeam is projected on the rotating grating and due to diffraction of the lightwaves, lightbeams of different order occur.

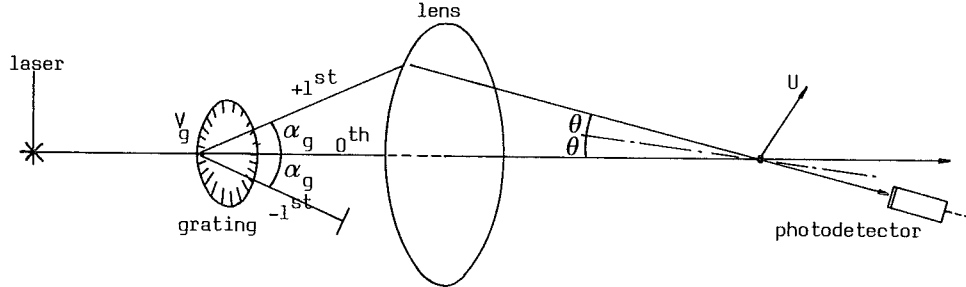


Figure A-6: Diffraction of the laserbeam due to the rotating grating.

For further explanation only the high intensity 0th order lightbeam (illuminating beam) and the low intensity +1st order lightbeam (reference beam) are taken into account.

The grating consists of a disc with slots in the radial direction. The disc rotates with a constant velocity. The velocity in the tangential direction at the point where the laserbeam passes the grating is v_g .

The number of slots of the grating is N .

The tangential velocity $v_g = v_g \cdot d_g \cdot N$, in which v_g is the rotation frequency of the disc and d_g is the distance between the slots.

A Doppler frequency results: $v_s = 2 \cdot v_g \cdot \sin \alpha_g / \lambda_0$, the difference in frequency between the 0th and +1st order beams is: $v_s = v_g \cdot \sin \alpha_g / \lambda_0$, the pre-shift frequency.

The angle α_g is determined by d_g and λ_0 : $\sin \alpha_g = \lambda_0 / d_g$, so $v_s = v_g / d_g$ or $v_s = v_g \cdot N$.

The pre-shift frequency is only consequently determined by the geometry of the grating (N) and the rotating frequency (v_g) of the disc.

How do the beams of the ...-2nd, -1st, 0th, +1st, +2nd,... order arise?

Assume a lightwave arrives at a slot, which is not moving, and is deflected by an angle α_g .

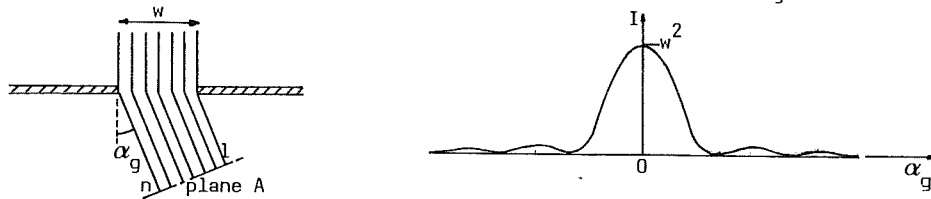


Figure A-7: Diffracting lightwave and its intensity, one slot.

The front of the beam consists of n equal waves. It is clear that at a plane A a phase difference occurs between wave 1 and n .

It can be shown (Durst, 1976) that the intensity of the lightwave reads:

$$I_1 = w^2 \cdot \sin^2(\pi \cdot w \cdot \sin \alpha_g / \lambda_0) / (\pi \cdot w \cdot \sin \alpha_g / \lambda_0)^2$$

the so called Fraunhofer deflection, in which w is the amplitude of the lightwave.

In figure A-7 it is also shown that a maximum of intensity occurs at $\alpha_g = 0$.

For N slots the intensity reads (Durst, 1976):

$$I_N = I_1 \cdot \sin^2(N \cdot \pi \cdot d_g \cdot \sin \alpha_g / \lambda_0) / \sin^2(\pi \cdot d_g \cdot \sin \alpha_g / \lambda_0)$$

From the formula for I_N and from figure A-8, it can be seen that maxima of intensity occur at $k \cdot \pi$ radians, with $k = \dots -2, -1, 0, +1, +2, \dots$

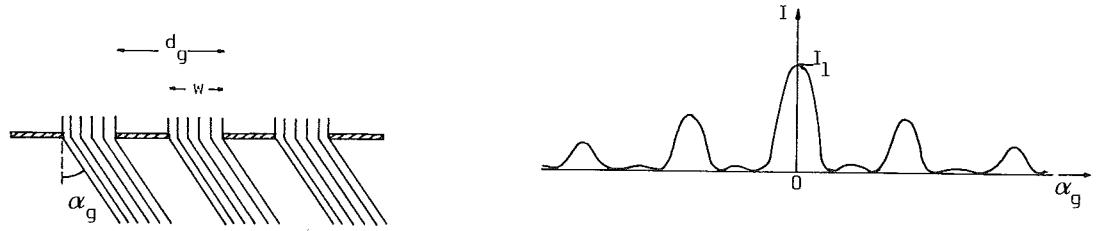


Figure A-8: Diffracting lightwave and its intensity, N slots.

So $\sin \alpha_g = k \cdot \lambda_0 / d_g$, and I_N is maximal for $k = 0$ ($\alpha_g = 0$) the 0th order beam. The 1st order beams make an angle $\sin \alpha_g = \lambda_0 / d_g$ with the 0th order beam and also their intensity is lower. In practice the higher order beams (2nd, 3th, ...) are screened.

The measuring volume

The two lightbeams which create the measuring volume are focussed through a lens. The light intensity of a beam is Gaussian in a cross-section of the beam. After passing the lens the lightbeam diameter is decreasing by convergence, but does not become zero. The minimum beam diameter, the waist of the beam, occurs in the focal point of the lens. After the waist the beam diverges again.

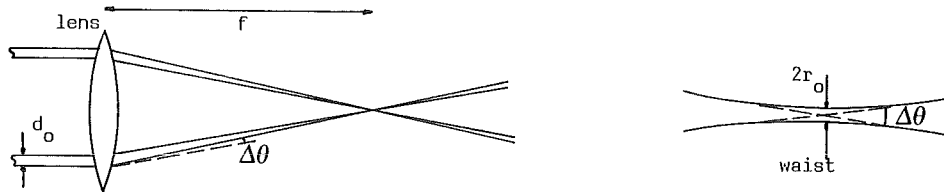


Figure A-9: Convergence of the lightbeams.

Scattered light in a point r_1 from stationary particles in a point r in an optical field can be described by Mie's scattering theory. (r_1 and r are vectors in the three-dimensional space) For more background information see Weyl (1952). A first approximation of the optical field is given in Durrani (1977):

$$E(r_1) = \sigma \cdot E(r) / (i \cdot k \cdot |r_1 - r|) \cdot e^{i \cdot k \cdot |r_1 - r|} \tag{a-11}$$

σ denotes the dimensionless scattering amplitude function and consists of a series of Legendre polynomials, which are not given here. The wavenumber $k = 2 \cdot \pi / \lambda_0$.

In the following analysis the assumptions are:

- the scattering particles in the fluid are spherical,
- the wave fronts in the vicinity of the focal point are plane and parallel.

The intensities of the lightbeams near the focal point are Gaussian and read:

$$I(x, y, z) = I_0 \cdot e^{-2 \cdot (x^2 + y^2) / (r_0^2 \cdot (1 + (\lambda_0 \cdot y / \pi \cdot r_0^2)^2))} \cong I_0 \cdot e^{-2 \cdot (x^2 + y^2) / r_0^2}$$

I_0 is the intensity in the centre of the lightbeam and $r_0 = 2 \cdot \lambda_0 / (\pi \cdot \Delta\theta)$ is the radius of the lightbeam in the waist. $\Delta\theta$ is the far field convergence angle of the lightbeam, $\Delta\theta = d_0 / f$. (f is focal length) The definition of r_0 is the radius of the lightbeam where the light intensity is $I_0 \cdot e^{-2}$.

The optical distribution in the field of the focussed lightbeam may be expressed as:

$$E(x, y, z) = E_0 \cdot e^{(i k y - (x^2 + y^2) / r_0^2)} \tag{a-12}$$

with $E_0 = I_0^{1/2} \cdot e^{-2 \pi i \cdot \nu \cdot t}$

The reflected light from the particles in the fluid is finally projected to a photodetector.

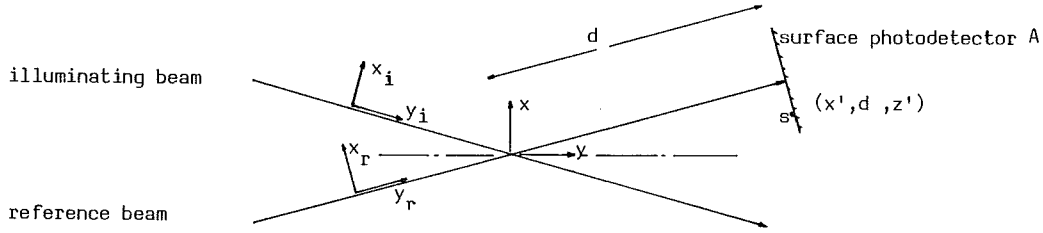


Figure A-10: Definition of coordinate systems.

For a point s on the surface of the photodetector formula (a-11) reads:

$$E_{is}(x', d, z') = \sigma / (i \cdot k \cdot d) \cdot E_i \cdot e^{i \cdot k \cdot s_1} ,$$

the field of the reflected light by particles due to light from the illuminating beam.

$$\text{And } E_{rs}(x', d, z') = \sigma / (i \cdot k \cdot d) \cdot E_r \cdot e^{i \cdot k \cdot s_1} ,$$

the field of the reflected light by particles due to light from the reference beam.

$$\text{With } s_1 = d_0 + (x_r - x')^2 / (2 \cdot d) + (z_r - z')^2 / (2 \cdot d) ,$$

which is defined in the x_r, y_r, z_r -coordinate system.

The complete field in a point on the surface of the photodetector reads:

$$E_d(x', d, z') = E_r(x', d, z') + E_{is}(x', d, z') + E_{rs}(x', d, z') \quad (\text{a-13})$$

In which $E_r(x', d, z')$ denotes the field of the reference beam directly projected on the photodetector.

The total intensity of the light on the surface of the photodetector is:

$$i_d = \eta \int_A |E_d|^2 \cdot dA \quad (\text{a-14})$$

η is the sensitivity of the photodetector.

Note that for complex numbers the following operation yields: $|X + Y|^2 = |X|^2 + |Y|^2 + X^*Y + X Y^*$.

Substituting (a-13) in (a-14) gives:

$$\begin{aligned} i_d = & \eta \int_A (|E_r|^2 + |E_{is}|^2 + |E_{rs}|^2) \cdot dA + \eta \int_A (E_r \cdot E_{rs}^* + E_r^* \cdot E_{rs}) \cdot dA + \\ & + \eta \int_A (E_{rs} \cdot E_{is}^* + E_{rs}^* \cdot E_{is}) \cdot dA + \eta \int_A (E_r \cdot E_{is}^* + E_r^* \cdot E_{is}) \cdot dA \end{aligned}$$

In short notation this reads:

$$i_d = i_i + i_{rr} + i_s + i_{ri} \quad (\text{a-15})$$

i_i : contribution of the individual fields,

i_{rr} : contribution due to mixing of the reference beam with scattered light from the reference beam,

i_s : contribution due to mixing of the two scattered radiations,

i_{ri} : contribution due to mixing of reference beam and scattered light from the illuminating beam.

The terms i_i and i_{rr} do not contain doppler frequency information, so these intensities are not significant. The intensity of the illuminating beam is far greater than that of the reference beam, which gives a very poor fringe contrast. The amplitude of i_s is very small compared to the amplitude of i_{ri} .

When the surface of the photodetector is large compared to the beam cross-section, than the first term of

i_{ri} reads:

$$\int_A E_R \cdot E_{is}^* \cdot dA = \iint_{-\infty}^{\infty} E_R(x', d, z') E_{is}^*(x', d, z') \cdot dx' \cdot dz' =$$

$$= 2 \cdot \pi \cdot \sigma / k^2 \cdot E_i^* \iint_{-\infty}^{\infty} E_R(x', d, z') / (-i \cdot \lambda_0 \cdot d) \cdot e^{-i \cdot k \cdot s_i} \cdot dx' \cdot dz'$$

In Durrani (1977) a solution for this equation is given which reads:

The integral represents the inverse propagation convolution of the reference field at a point (x', d_0, z') , on the photodetector surface, to the reference field on the particle at (x_R, y_R, z_R) .

Hence $\int_A E_R \cdot E_{is}^* \cdot dA = 2 \cdot \pi \cdot \sigma / k^2 \cdot E_i^*(x_i, y_i, z_i) \cdot E_R(x_R, y_R, z_R)$

and $i_{ri} = 4 \cdot \pi \cdot \sigma \cdot \eta / k^2 \cdot \text{Re}(E_i^*(x_i, y_i, z_i) \cdot E_R(x_R, y_R, z_R))$ (a-16)

with $E_i(x_i, y_i, z_i) = E_I \cdot e^{(i \cdot k \cdot y_i - (x_i^2 + z_i^2) / r_0^2)}$

$E_R(x_R, y_R, z_R) = E_R \cdot e^{(i \cdot k \cdot y_R - (x_R^2 + z_R^2) / r_0^2)}$

E_I^2 and E_R^2 are intensities of the illuminating and reference beam in the measuring volume.

Substitution in (a-16) and $C_0 = 4 \cdot \pi \cdot \sigma / k^2$ gives:

$$i_{ri} = \eta \cdot C_0 \cdot E_I \cdot E_R \cdot [e^{-(x_i^2 + z_i^2 + x_R^2 + z_R^2) / r_0^2}] \cdot \cos k(y_R - y_i)$$
 (a-17)

Transformation of (x_i, y_i, z_i) and (x_R, y_R, z_R) to (x, y, z) , see also figure A-10, gives:

$$\begin{aligned} x_i &= x \cdot \cos \theta + y \cdot \sin \theta & x_R &= x \cdot \cos \theta - y \cdot \sin \theta \\ y_i &= y \cdot \cos \theta - x \cdot \sin \theta & y_R &= y \cdot \cos \theta + x \cdot \sin \theta \\ z_i &= z & z_R &= z \end{aligned}$$

Substitution in (a-17):

$$i_{ri} = \eta \cdot C_0 \cdot E_I \cdot E_R \cdot [e^{-2(x^2 \cdot \cos^2 \theta + y^2 \cdot \sin^2 \theta + z^2) / r_0^2}] \cdot \cos(2 \cdot k \cdot x \cdot \sin \theta)$$
 (a-18)

The maximum of i_{ri} occurs for $x=y=z=0$ and the intensity is decreased to a value of e^{-2} times the maximum at:

$$x^2 \cdot \cos^2 \theta + y^2 \cdot \sin^2 \theta + z^2 = r_0^2$$
 (a-19)

Formula (a-19) represents an ellipsoide.

The measuring volume is limited arbitrarily by the value e^{-2} , so the dimensions of the measuring volume are:

$$\Delta x = 2 \cdot r_0 / \cos \theta \quad ; \quad \Delta y = 2 \cdot r_0 / \sin \theta \quad ; \quad \Delta z = 2 \cdot r_0$$

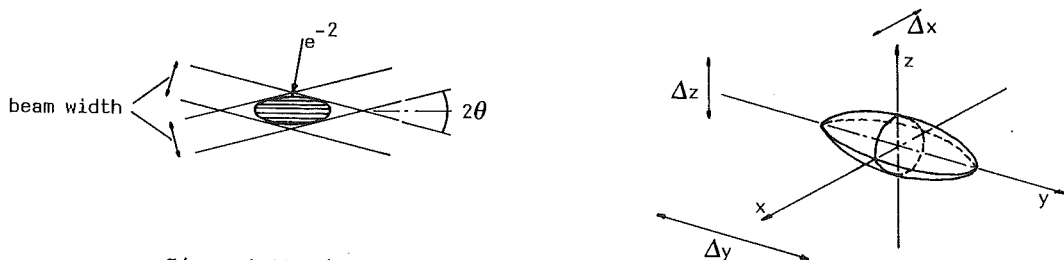


Figure A-11: The measuring volume.

Example:

data: $\theta = 10^\circ$, $2 \cdot r_0 = 1 \text{ mm}$. The dimensions of the measuring volume are: $\Delta x = 1.02 \text{ mm}$,
 $\Delta y = 5.76 \text{ mm}$,
 $\Delta z = 1.00 \text{ mm}$.

with $\theta = 20^\circ$ the dimensions of the measuring volume are: $\Delta x = 1.06 \text{ mm}$,
 $\Delta y = 2.92 \text{ mm}$,
 $\Delta z = 1.00 \text{ mm}$.

Intensity due to moving particles in the measuring volume

The coordinates of particles in the measuring volume moving with a velocity U_b are $(x_0 + U_b \cdot t, y_0, z_0)$. The expression $\cos(2.k.x.\sin\theta)$ in formula (a-18) can be corrected in case of a pre-shift frequency ν_s , the expression then reads: $\cos(2.\pi.\nu_s.t + 2.k.x.\sin\theta)$.

With $x_0 = 0$ for convenience formula (a-18) reads:

$$i_{ri}(t) = \eta.C_0.E_I.E_R \cdot [e^{-2(U_b^2.t^2.\cos^2\theta + y_0^2.\sin^2\theta + z_0^2)/r_0^2}] \cdot \cos(2.\pi.\nu_s + 4.\pi.U_b.\sin\theta/\lambda_0)t \tag{a-20}$$

The behaviour of $i_{ri}(t)$ when a particle moves through the measuring volume with a velocity U is shown in figure A-12. This effect is called the doppler burst.

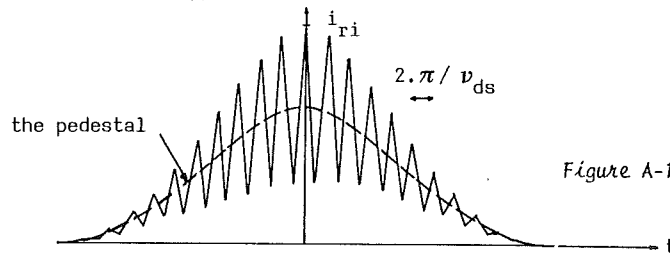


Figure A-12: The doppler burst.

The light intensity sketched in figure A-12 is converted by the photodetector to a voltage. This voltage is processed by a so-called tracker, which selects the frequency ν_{ds} from the doppler burst. Through formula (a-10) the particle velocity U_b is known.

Signal processing by a frequency tracker

There are different methods to detect the doppler frequency from a doppler burst.

In this part the method with a frequency tracker is described.

From figure A-12 it is clear that the signal consists of a part with low frequency, the pedestal, and a part with high frequency.

To detect the frequency ν_{ds} the pedestal is removed with a high pass filter (HPF), this is done inside the tracker.

After filtering the following signal results:

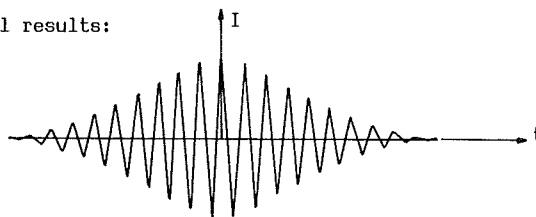


Figure A-13: The doppler burst after the HPF.

The tracker converts the voltage from the photodetector to a voltage level which is proportional to ν_{ds} . Different particles moving through the measuring volume with different doppler frequencies, generate converted voltages V_1, V_2, \dots . The doppler frequency is replaced by: $V.K$.

V is the voltage due to a moving particle through the measuring volume and K is the conversion factor of the tracker in Hz/volt.

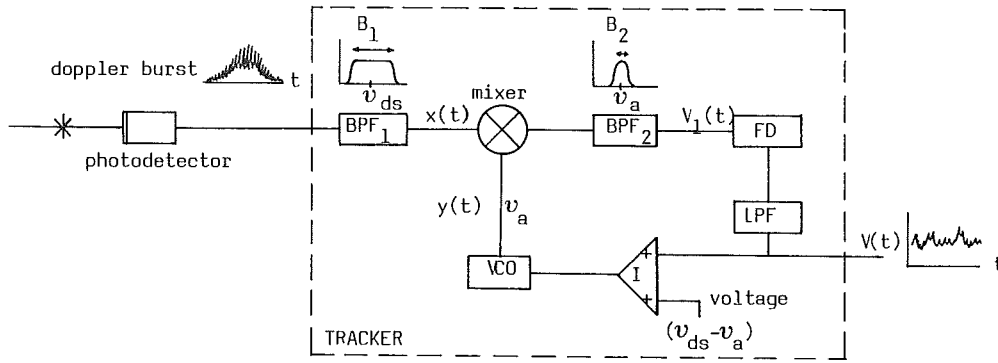
The principle of the tracker is shown in figure A-14.

The BPF_1 removes the pedestal of the doppler burst and also the high frequencies due to noise.

The resulting signal $x(t)$ is mixed with the signal $y(t)$ from the VCO.

The mixed signal has a frequency $\nu_0 - \nu_{ds}$ and is filtered by a BPF_2 with bandwidth $B_2 \ll B_1$.

The frequency discriminator determines the difference between $\nu_0 - \nu_{ds}$ and ν_a and generates a voltage to change the frequency ν_a , in such a way as to make $\nu_0 - \nu_{ds}$ equal to ν_a .



BPF = bandpass filter, LPF = lowpass filter, FD = frequency discriminator, I = integrator, VCO = voltage controlled oscillator.

Figure A-14: Frequency tracker (Durrani, 1977)

The variations in the voltage due to the FD are analogous to v_{ds} .
 From the analog output signal $V(t)$ the flow velocity of the fluid can be determined.
 The pre-shift frequency can be eliminated by setting the output voltage of the tracker to zero, when the flow velocity of the fluid is zero.
 The voltage read from the output voltmeter is a direct measure for the flow velocity of the fluid in the measuring volume.
 The relation between the doppler frequency $v_d = V(t) \cdot K$ and the flow velocity U_b is:

$$U_b(t) = \lambda_0 / (2 \cdot \sin \theta) \cdot K \cdot V(t) \tag{a-21}$$

Note: The tracker must be fast enough to determine changes in v_{ds} .
 When two particles enter the measuring volume almost simultaneously the doppler burst of the second particle can not be distinguished from the doppler burst of the first particle. A mean doppler frequency is determined in that case. This situation occurs when too many particles are present in the fluid.

The influence of glass walls on the measuring volume

Generally the laser, the lenses, the photodetectors and the tracker will be positioned outside the medium in which the measurements are done.
 For example in case of measurements in water in a flume the lightbeams enter and leave the water generally through glass walls.
 A light beam passing from air into glass undergoes refraction due to the change in refractive index. The same occurs when the beam passes from glass into water.

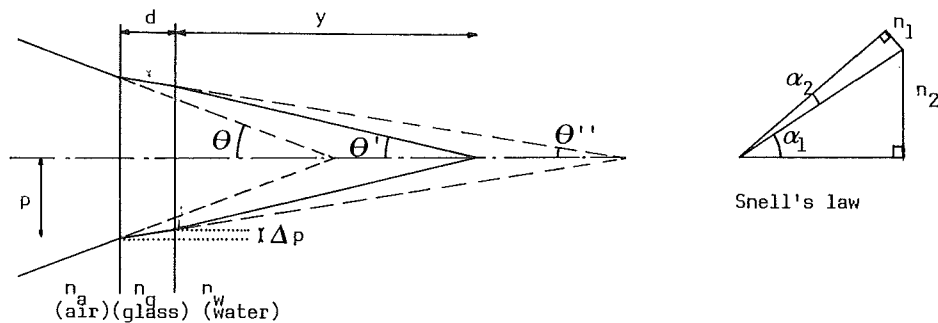


Figure A-15: Influence of the wall on the position of the measuring volume.

Due to refraction the two beams will intersect at a greater distance from the wall.
 In that case Snell's law can be used: $\sin \alpha_1 / \sin \alpha_2 = n_2 / n_1$, with n_1, n_2 as refractive index for the two materials.

For determination of U_b , $\sin\theta$ is of importance. The angle between the beams is 2θ in air, $2\theta'$ in water and $2\theta''$ in glass.

So,
$$\sin\theta''/\sin\theta = n_a/n_g \quad \text{and} \quad \sin\theta'/\sin\theta'' = n_g/n_f$$

give:
$$\sin\theta' = n_a/n_f \cdot \sin\theta \quad (\text{a-22})$$

The values of the refractive indices are: $n_{\text{air}} \cong 1$; $n_{\text{glass}} \cong 1.5$; $n_{\text{water}} \cong 1.3$.

From formula (a-22) follows, that θ' is independent from the glass. The same holds for refraction which occurs for a beam passing water, glass and air.

As the photodetector is placed in air on the other side of the flume formula (a-9) holds:

$$v_d = 2 \cdot U_b \cdot \sin\theta / \lambda_0$$

and is independent of glass and fluid, because both $\sin\theta$ and λ are proportional to n .

The length y to the measuring volume in the fluid is however influenced by refraction.

So $\Delta p = d \cdot \tan\theta'' = d \cdot \arcsin(n_a/n_g \cdot \sin\theta)$ and

$$y = (p - \Delta p) / \tan\theta' \quad (\text{a-23})$$

In practice $\Delta p \ll p$, so (a-23) simplifies to: $y \cong p / \tan\theta'$.

Particles in the fluid

Essential for the determination of a doppler burst is the presence of scattering particles which scatter the laser light in the fluid.

Generally there are enough scattering particles present in water, but often particles have to be seeded to receive a good doppler signal, specially when a small measuring volume is used.

Particles have to fulfill the following demands specific for water:

- The density of particles must be approximately equal to the density of the surrounding fluid,
- The particles must have the same velocity as the surrounding fluid,
- The particles size must be small enough to follow the fluctuations of the flow almost instantaneously. (mass and acceleration forces must be very small),
- The particles must scatter the laser light sufficiently,
- The particles concentration in the fluid must be so that a homogeneous refractive index in the fluid occurs,
- The number of particles in the fluid must be large enough to give a detectable signal, but must not be too large.

Notes:

- In a stagnant fluid the tracker can sometimes determine a 'flow velocity' which is due to Brownian movements,
- Particles may be subjected to lift forces due to flow velocity gradients, which occur near walls. Due to these forces extra flow velocity components are added.

Two component flow velocity measurements with the LDA

With the beam configuration of one illuminating and one reference beam, one flow velocity component can be determined.

This flow velocity component is normal to the bisectrice of the angle between the two beams and lies in the plane of the two beams.

To determine another flow velocity component in the same measuring volume, an extra reference beam can be added. For instance the other -1^{st} order lightbeam of the rotating grating can be used for this. Interference of the -1^{st} order beam and the 0^{th} and the other $+1^{st}$ order beam will occur, like discribed in formula (a-15).

However these signals are not significant because they do not contain doppler frequency information.

The beam configuration with two reference and one illuminating beam sketched in figure A-16, can be used to obtain two velocity components V_1 and V_2 .

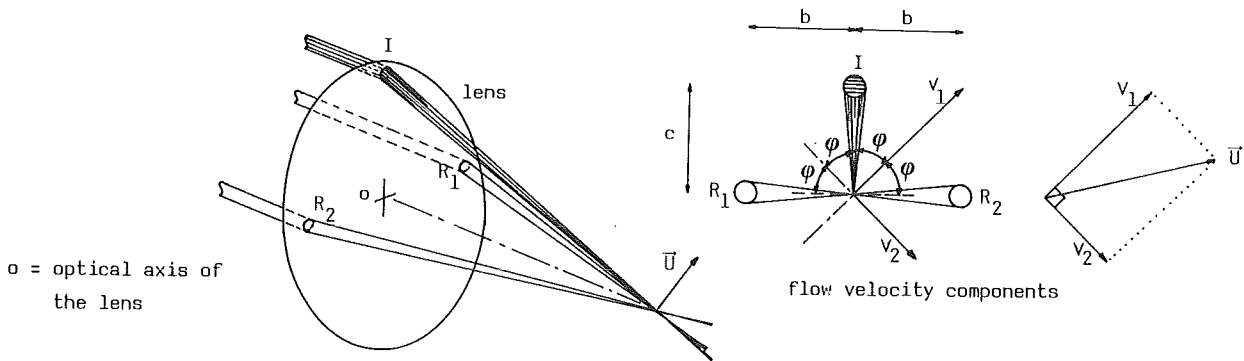


Figure A-16: Two component LDA system.

In principle a 3^{th} reference beam can be added to determine three flow velocity components, this configuration is not treated.

The beams are set in a configuration as sketched in figure A-16. The angle 2θ between the beams R_1 and R_2 is equal to the angle between the beams R_2 and I .

Flow velocity component V_1 is measured in the plane of the beams R_1 and I and component V_2 is situated in the plane of R_2 and I .

Composition of V_1 and V_2 gives the velocity vector \bar{U} and turbulent quantities are easily determined when the angle $\phi = 45^\circ$. This will be made clear in figure A-17.

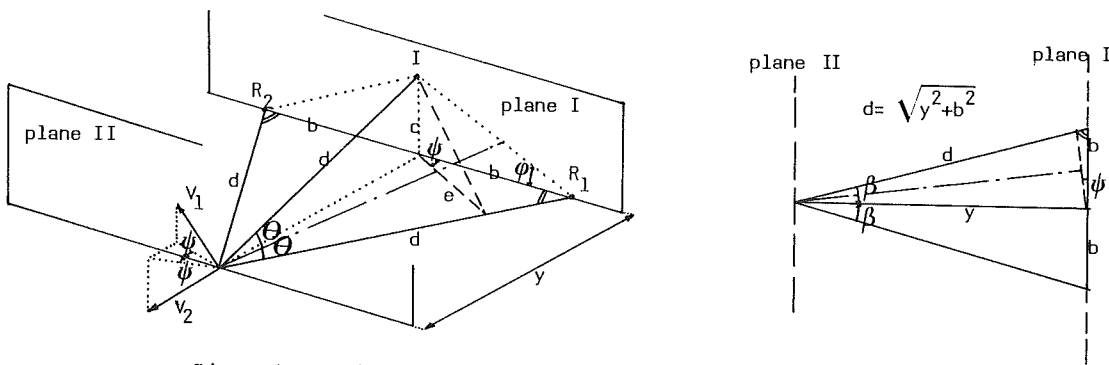


Figure A-17: Direction of the flow velocity vector in relation to ϕ .

The given length's are y , b and the angle θ is known, the plane I is parallel to plane II.

The sine-rule gives:

$$(\sqrt{y^2+b^2} - d)/\sin\psi = e/\sin(\frac{1}{2}\pi - \beta) = e \cdot \sqrt{y^2+b^2} / y$$

so:

$$\sin\psi = (1 - d/\sqrt{y^2+b^2}) \cdot y/e \tag{a-24}$$

It is convenient when the flow velocity vectors V_1 and V_2 are in the plane II, which is parallel to plane I. For example plane I is a glass wall and plane II is an imaginary plane somewhere in the fluid.

To obtain this situation ψ must be zero, substituting this in (a-24) gives: $d/\sqrt{y^2+b^2} = 1$, and from figure A-17 it is clear that $d = \sqrt{y^2+c^2}$.

This yields $b = c$ and so $\phi = 45^\circ$. The beam configuration with $b = c$ is called the 45° beam configuration.

Resolution of flow velocities

In some cases it is not possible to measure directly the desired flow velocity components, so two other components are measured and resolved in the desired components.

A demand for the two reference beams is that these beams must be projected to the photodetectors, so no obstacles are allowed in the path of the reference beams.

A demand for the illuminating beam is that this beam cannot pass a free water surface before intersecting the measuring volume. A free water surface is not at rest when the water flows, so due to this effect and refraction the direction of the illuminating beam is not stable.

For instance near a wall or a water surface flow velocity components have to be measured as sketched in figure A-18.

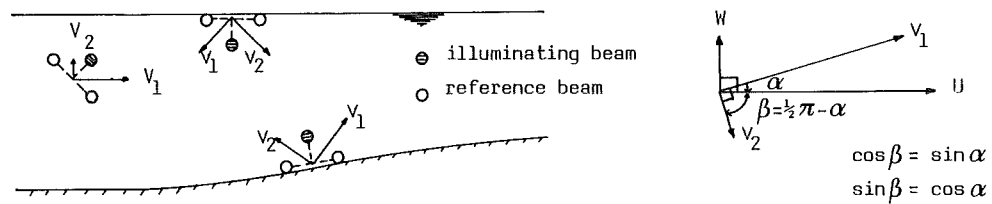


Figure A-18: Velocity components.

In many situations it is convenient to transform the flow velocity components V_1 and V_2 , to the components U and W . This transformation reads:

$$\begin{aligned} U(t) &= V_1(t) \cdot \cos \alpha + V_2(t) \cdot \cos \beta \\ W(t) &= V_1(t) \cdot \sin \alpha - V_2(t) \cdot \sin \beta \end{aligned} \quad (\text{a-25})$$

Turbulent quantities can be determined after the Reynolds decomposition:

$$\begin{aligned} V_1(t) &= \bar{V}_1 + v_1' & \text{and} & & \bar{V}_1(t) &= \bar{V}_1 & ; & & \bar{v}_1' &= 0 \\ V_2(t) &= \bar{V}_2 + v_2' & \text{and} & & \bar{V}_2(t) &= \bar{V}_2 & ; & & \bar{v}_2' &= 0 \end{aligned} \quad (\text{a-26})$$

The mean flow velocities with the aid of (a-26) read:

$$\begin{aligned} \bar{U} &= \bar{V}_1 \cdot \cos \alpha + \bar{V}_2 \cdot \cos \beta \\ \bar{W} &= \bar{V}_2 \cdot \sin \alpha - \bar{V}_1 \cdot \sin \beta \end{aligned} \quad (\text{a-27})$$

The turbulent quantities can be determined with the aid of (a-25), (a-26) and (a-27) and read:

$$\overline{u'w'} = (\overline{v_1'^2 - v_2'^2}) \cdot \sin \alpha \cdot \cos \alpha + \overline{v_1'v_2'} \cdot (\sin^2 \alpha - \cos^2 \alpha) \quad (\text{a-28})$$

$$\overline{u'^2} = \overline{v_1'^2} \cdot \cos^2 \alpha + 2 \cdot \overline{v_1'v_2'} \cdot \sin \alpha \cdot \cos \alpha + \overline{v_2'^2} \cdot \sin^2 \alpha \quad (\text{a-29})$$

$$\overline{w'^2} = \overline{v_1'^2} \cdot \sin^2 \alpha - 2 \cdot \overline{v_1'v_2'} \cdot \sin \alpha \cdot \cos \alpha + \overline{v_2'^2} \cdot \cos^2 \alpha \quad (\text{a-30})$$

Formula (a-28) denotes the Reynolds shear stress, (a-29) and (a-30) denote turbulent energies.

The terms $\overline{v_1'^2}$, $\overline{v_2'^2}$, $\overline{u'^2}$ and $\overline{w'^2}$ are auto-correlations, the terms $\overline{v_1'v_2'}$ and $\overline{u'w'}$ are cross-correlations.

The overall LDA system

The system sketched in figure A-19 is for a situation in which the instantaneous flow velocities in a vertical plane are measured.

The measurements are carried out in a flume and the fluid is water.

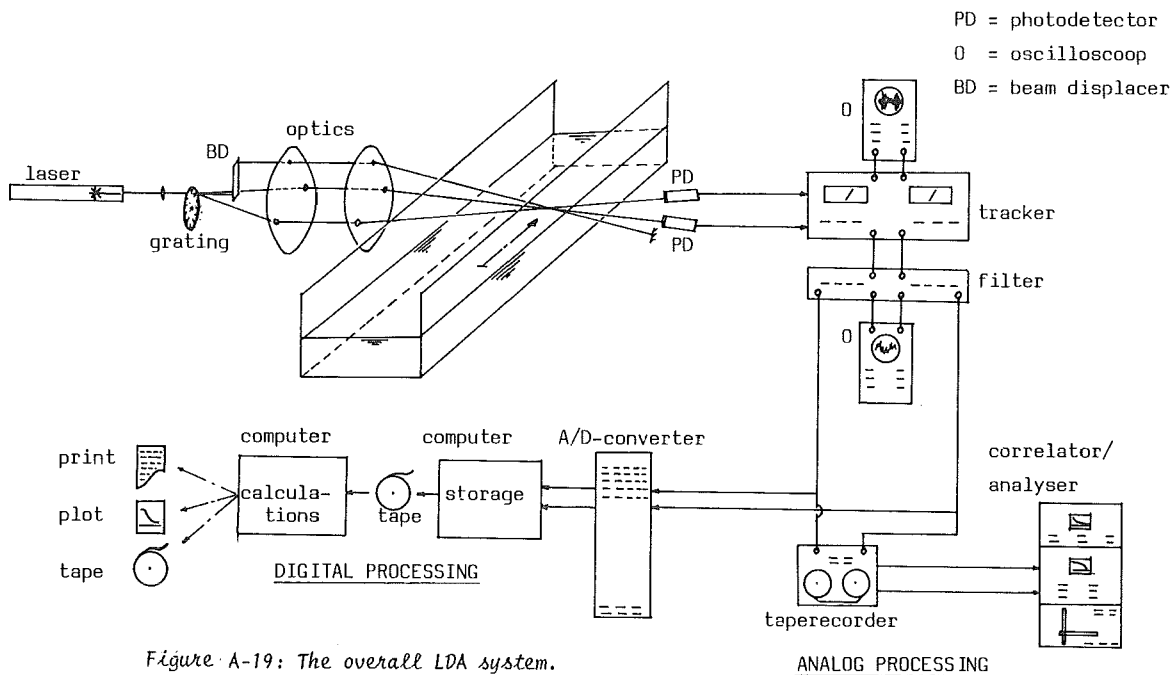


Figure A-19: The overall LDA system.

The laser beam is focussed on the rotating grating. The 0th and 1st order beams are focussed in the measuring volume by means of optics.

The 0th order beam is displaced by a beam displacer in order to create the 45° beam configuration.

The measuring volume is projected in the water at the desired position.

The photodetectors registrate the doppler bursts and the tracker converts this into a voltage level for both signals. The signals from the tracker are filtered in order to remove high frequencies (noise) or if desired low frequencies (mean velocity).

The filtering is carried out with lowpass filters (LPF), highpass filters (HPF) or bandpass filters (BPF).

The voltage levels represent the flow velocities V_1 and V_2 as a function of time.

The signals can be stored analog as well as digital.

Analog: The signals are recorded with a taperecorder. From the tape the signals can be processed by a correlator/spectrum analyser, to produce auto- and cross-correlations and power-spectra of the turbulent quantities. The results can be shown on a screen or can be plotted.

Digital: The analog signals are lead to an A/D-converter which converts the signals and sends the digital information to the computer.

The data are stored on computer tape, and can be processed by the computer.

When software is available mean values of the flow velocities can be calculated and also turbulent quantities or correlations or spectra.

The results can be printed, plotted or stored on tape or disk.

A LDA system used in practice is shown in figure A-20.

Overview of important formulas and data

The data given below are specific for one of the types of the LDA systems in use at the Laboratory of Fluidmechanics Delft.

Laser:

5mW Spectra Physics Model 120, TPD heterodyne system.

He-Ne laser with a wavelength: $\lambda_0 = 632.8 \cdot 10^{-9}$ m, beamdiameter $d_0 = 1$ mm at $I_0 \cdot e^{-2}$.

Grating:

rotation frequency: $\nu_g = 48.5$ Hz.

There are three tracks of gratings on the disc:

number of lines N:	2^{14}	2^{13}	2^{12}
distance between the lines d_g :	$6.08 \mu\text{m}$	$11.45 \mu\text{m}$	$21.4 \mu\text{m}$

pre-shift frequency $\nu_s = 800 \cdot 10^3$ Hz.

Optical system:

Type 400.

optical transfer factor: $K_0 = 2 \cdot \sin\theta / \lambda_0$ (m^{-1}), with 2θ as the angle in air between the illuminating beam and the reference beam.

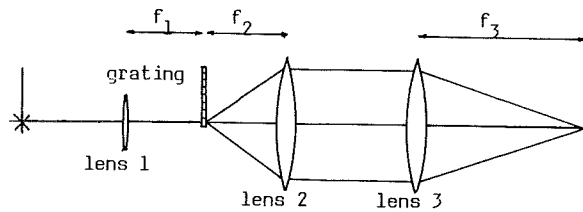
Lenses:

focus lengths: $f_1 = 120$ mm or 50 mm

$f_2 = 250$ mm

$f_3 = 330$ mm or 600 mm

beamdiameter after passing the grating: $d_1 = d_0 \cdot f_2 / f_1$.

Measuring volume:

dimensions: width $\Delta x = 2 \cdot r_0 / \cos\theta$; length $\Delta y = 2 \cdot r_0 / \sin\theta$; thickness $\Delta z = 2 \cdot r_0$

Near the measuring volume the beam radius is $r_0 = 2 \cdot \lambda_0 / \pi \cdot \Delta\theta$ and $\Delta\theta \cong d_1 / f_3$.

The width and thickness of the measuring volume are not influenced by refraction of the beams, the length however is influenced through $\sin\theta' = \sin\theta / n$. With refractive index $n = n_{\text{water}} / n_{\text{air}} = 1.333$.

After substitution the dimensions of the measuring volume in water are:

$$\text{width: } \Delta x = 4 \cdot \lambda_0 \cdot f_3 / (\pi \cdot d_1 \cdot \cos\theta) \quad (\text{m})$$

$$\text{length: } \Delta y = 4 \cdot \lambda_0 \cdot f_3 \cdot n / (\pi \cdot d_1 \cdot \sin\theta) \quad (\text{m})$$

$$\text{thickness: } \Delta z = 4 \cdot \lambda_0 \cdot f_3 / (\pi \cdot d_1) \quad (\text{m})$$

Photodetectors:

HP 4220, frequency range: $60 \cdot 10^3 - 5 \cdot 10^6$ Hz.

Tracker:

Frequency tracker type 1077/2M

Input frequency range: $100 \cdot 10^3 - 2 \cdot 10^6$ Hz.

Conversion factor: $K = 200 \cdot 10^3$ Hz/volt.

A/D-converter:

conversion: $10 \text{ volt} \cong 2^{14} - 1 = 16383$ (digital)

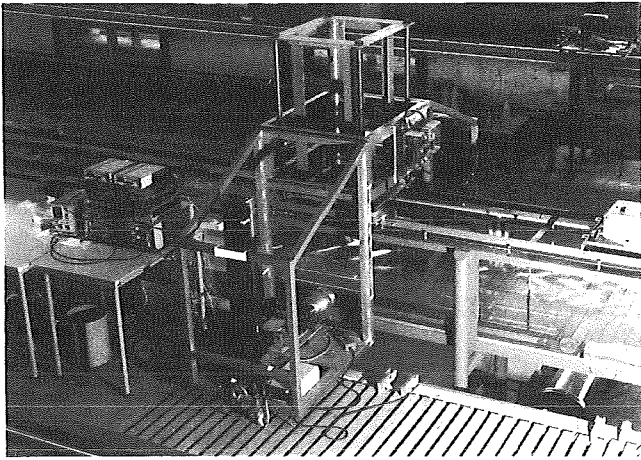
Flow velocity representation:

The representation in volts from the tracker is: $1 \text{ volt} \cong K / K_0$ (m/s)

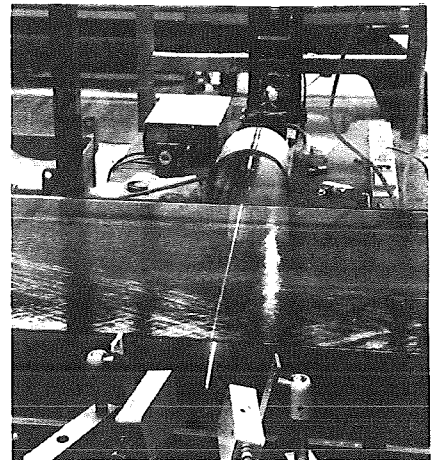
The representation from the A/D-converter: $1 \cong K / (16383 \cdot K_0)$ (m/s)

Note that amplification of the signals must be taken into account to derive the right conversion.

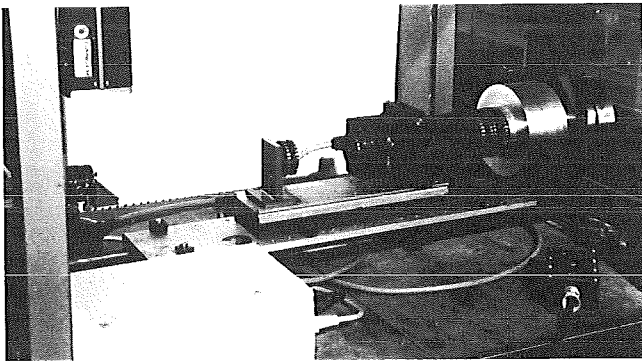
A LDA heterodyne system in practice



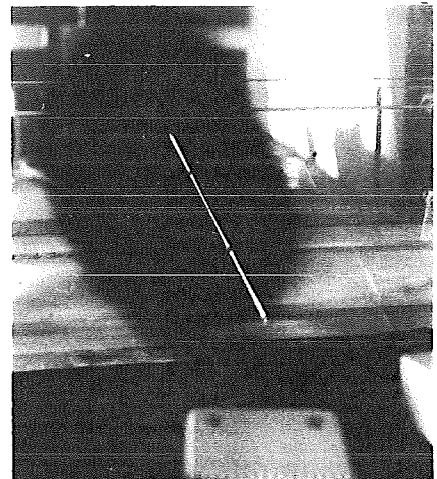
overall view



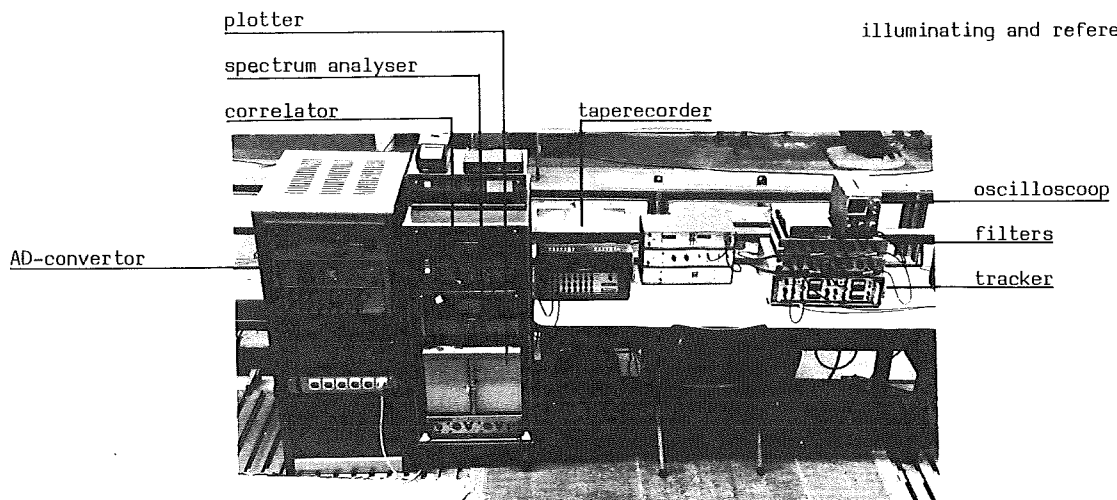
optics and photodetectors



optics



illuminating and reference beams



analog and digital processing equipment

Figure A-20: The LDA system in practice

List of symbols

a	distance	w	width of slot
A	Surface of the photodetector	x	coordinate, or with index: i, o, r, '
b	distance	y	coordinate, or distance, or with index: i, r
B_1, B_2	bandwidth of filter	z	coordinate, or with index: i, r, '
c	velocity of light, or distance	Δx	width of measuring volume
C_0	factor: $4 \cdot \pi \cdot \sigma / k^2$	Δy	length of measuring volume
d	distance, with subscript:	Δz	thickness of measuring volume
g	distance between slots	$x(t), y(t)$	signal in the tracker
o	beam diameter from the laser	$E(..)$	optical field, or with index: d, I, is, r, R, rs
O	distance measuring volume to photodetector	$Re(..)$	real part of a complex expression
l	beam diameter after grating: $d_0 \cdot f_2 / f_1$	α	angle, or with index: 1, 2
e	distance	β	angle
f	focal length	Θ	angle, or with index: ', ''
f_1, f_2, f_3	focal length	φ	angle, or with index: 1, 2
i	complex number, with subscript:	ψ	angle
d	total light intensity	η	sensitivity of the photodetector
i	light intensity of individual fields	λ	wavelength of the laser light, or with index: o, Oi, Or
ri	intensity after mixing of light	ν	frequency of the laser light, or with index: a, d, ds, g, Pi, Pr, o, Oi, Or, s
rr	intensity after mixing of light	σ	dimensionless scattering amplitude function of the optical field
s	intensity after mixing of light	$\Delta \Theta$	far field convergence angle of the beam
I	intensity of optical field, with subscript:		
N	intensity for N slots		
o	intensity in the centre of the beam		
l	intensity for l slot		
k	wavenumber: $2 \cdot \pi / \lambda_0$, or integer		
K	conversion factor		
K_0	optical transfer factor		
n	refractive index air-water, with subscript:		
a	refractive index of air		
g	refractive index of glass		
w	refractive index of water		
1	refractive index of material 1		
2	refractive index of material 2		
N	number of slots on the disc		
p, Δp	distance		
r, r_1	place vector in the optical field		
r_0	beam radius in the waist		
s_1	distance		
t	time		
u'	fluctuating flowvelocity		
U, U_0	instantane flowvelocity		
\vec{U}	velocity vector		
\bar{U}	mean flow velocity		
v'_1, v'_2	fluctuating flowvelocity		
V_1, V_2	instantane flowvelocity, of voltages		
\bar{V}_1, \bar{V}_2	mean flowvelocity		
V_g	tangential velocity of the grating		
w'	fluctuating flowvelocity		
W	instantane flowvelocity		
\bar{W}	mean flowvelocity		

Literature

Durrani T.S., Greated C.A., Lasersystems in flow measurement, Plenum Press, New York, 1977

Durst F., Melling A., Whitelaw J.H., Principles and practice of laser-doppler anemometry, Academic Press, London, 1976

Evers D.J.W.M., Huigen G., Welling W.A., Laser-doppler snelheidsmetingen, signaalverwerking (in dutch) PT-werktuigbouw 38, nr. 9, 1983, p. 71-75

Menzel D.H., Fundamental formulas of physics (2 vol) Dover Publications, New York, 1960

Welling W.A., De laser-doppler methode (in dutch), PT-werktuigbouw 37, nr. 12, 1982, p. 72-75

Weyl H., Space-Time-Matter, Dover Publications, New York, 1952

appendix B

Preliminary experiments with a dune on a conveyor

Preliminary experiments with a dune on a conveyor

To measure local instantaneous flow velocities and local sediment transport under well defined conditions, an experiment in a straight laboratory flume is suitable.

The flow conditions in the flume are kept constant, so a quasi-steady situation occurs.

When a series of sand dunes is created in the flume, however, the shape of the dunes is changing, dunes are catching up and the local sediment is not constant.

To create a steady situation solid dunes can be used, but then no sediment transport occurs so the local transport along the dunes is not known in principle.

However, an estimation of the transport can be made from experiments with moving sand dunes.

Another set up is to fix a series of solid dunes to the bottom of the flume, remove one solid dune and put a conveyor in its place, on the conveyor belt a certain quantity of sand (the volume of one dune) is laid. The solid dunes upstream and downstream the conveyor create a water movement which corresponds with the situation of moving dunes and the sand on the conveyor belt behaves like a moving dune.

The sand on the conveyor belt is transported downstream over the surface of the sand dune and so the dune propagates downstream.

The propagation of the sand dune, however, is neutralized by the upstream propagation velocity of the conveyor belt. The sand dune has a propagation velocity zero relative to the flume.

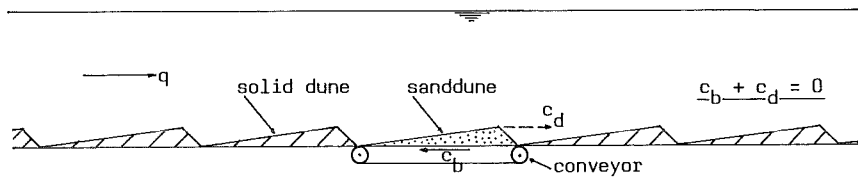


Figure B-1: Principle of a sanddune on a conveyor.

The advantages of this set up are:

- The mean local sediment transport along the dune is known (conveyor belt velocity times local dune height),
- The measuring equipment does not have to be moved in order to keep up with a point along the dune,
- The set up corresponds satisfactory with a situation of a series of moving dunes.

Preliminary experiments showed that the sanddune on the conveyor is not stable.

Due to the wake behind the solid dune the propagation velocity along the sanddune is not constant.

With respect to the solid dunes a so-called 'return transport' occurred.

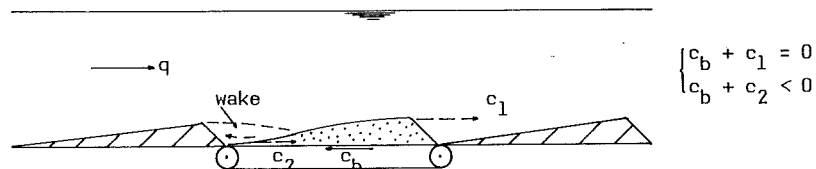


Figure B-2: Return transport in the wake upstream the sanddune.

The top of the dune propagated with a velocity c_1 , but the foot of the dune in the vicinity of the wake has a propagation velocity $c_2 < c_1$, so the dune 'stretched' more and more sand piled up in the wake.

This effect is even stronger near the walls of the flume where the flow velocity is too small to transport the sand sufficiently.

Due to both effects the dune height decreased in time, the sand piled up in the wake and one large dune occurred consisting of the solid dune upstream the conveyor and the sand.

Different shapes of the solid dunes upstream the conveyor did not prevent the return transport.

In figure B-3 the shape of the sanddune in time is sketched in top view.

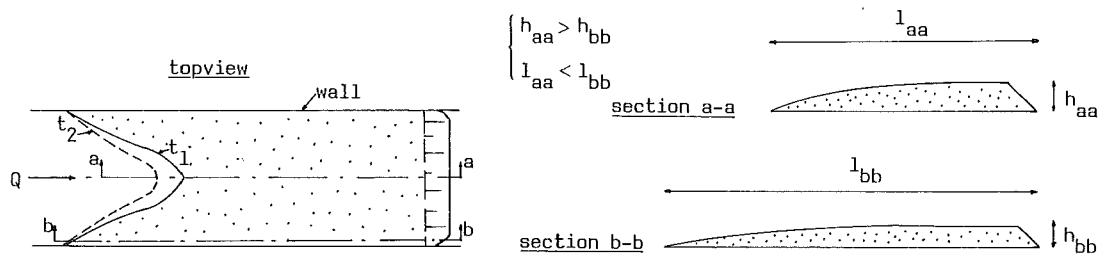


Figure B-3: Behaviour of the sanddune in time.

To create a stationary sanddune the return transport has to be eliminated.

The next rigorous step is to remove the solid dunes and furthermore to reduce the width of the sanddune. This situation is called the 'solitary dune situation'.

Due to the absence of the wake upstream the dune and the reduced influence of the wall of the flume no return transport occurred.

The dune width is reduced by using supports on both sides of the dune as sketched in figure B.4.

The supports also prevented loss of sand on both sides of the dune and the flowvelocity in the centre part of the flume is high enough to transport the sand sufficiently even in the vicinity of the supports. Due to the abrupt upstream end of the supports a vortex street is generated which introduces enough turbulence to transport sand particles very close to the supports.

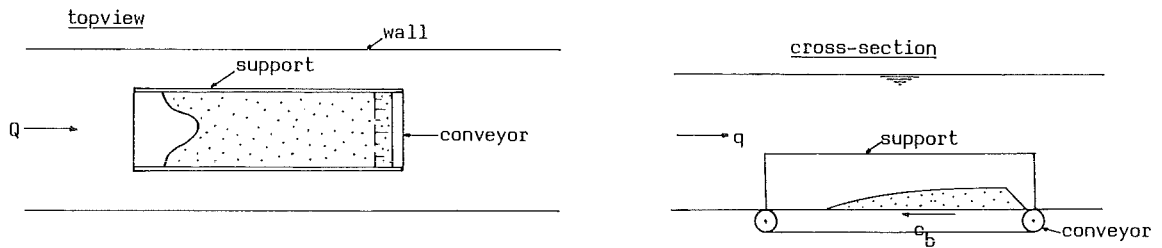


Figure B-4: Principle of set up with solitary dune.

Preliminary experiments showed that the sand on the conveyor belt shaped as a dune.

With this set up a dune is created which:

- has a constant shape during a long period,
- is easily accessible for the measuring equipment,
- has a known local transport along the dune

The flowvelocity profile upstream the solitary dune is almost logarithmic due to the long straight horizontal bed.

This is an advantage for the upstream boundary condition used in the computer program to calculate the flow-field above the dune.

A disadvantage of the set up is that the situation of one dune is not comparable with the natural situation of a series of dunes

But for a start of the investigation of the mechanism of sediment transport in an accelerating flow, the set up is interesting.

The shape of the solitary dune is reasonably symmetric with respect to the flume axis and the sediment transport is mainly directed in the main flowdirection.

appendix C

Tables of measured data

contents:

Table C.1; figures: 4.1, 4.2, 4.3

Table C.2; figure : 4.8

Table C.3; figure : 4.7

Table C.4; figures: 4.13, 4.16

Table C.5; figure : 4.13

Table C.6; figures: 4.14, 4.16

Table C.7; figure : 4.14

Table C.8; figures: 4.15, 4.16

Table C.9; inflow boundary, figure: 4.10

Table C.10; dune heights, figures: 4.13,
4.14, 4.15, 4.16, 4.18

Table C.11; angles of streamlines in
measurements and calculation

Table C.1 figures: 4.1, 4.2, 4.3										
x_1 (m)	x_3 (mm)	U_1 (m/s)	U_3 $\times 10^{-2}$ (m/s)	$\overline{u_1^2}$ $\times 10^{-2}$ (m^2/s^2)	$\overline{u_3^2}$ $\times 10^{-3}$ (m^2/s^2)	$\overline{-u_1 u_3}$ $\times 10^{-3}$ (m^2/s^2)	$\alpha + \beta$ ($^\circ$)			
16.00	2	0.4027	-0.6445	0.2811	0.4429	0.5173	45	conversion tape : WW8438 pte.mv2mm.C311 label: 1 reorganisation tape: WW8439 pte.mv2mm.R311 label: 3 sample interval : 10 ms number of values : 47000 conversion factor : $1 = 4.3154 \times 10^{-5}$ m/s		
	4	0.4282	-0.6639	0.2793	0.4804	0.5366				
	7	0.4655	-0.7305	0.2603	0.5442	0.5667				
	9	0.4791	-0.7161	0.2604	0.5311	0.5410				
	14	0.5057	-0.7699	0.2429	0.5682	0.5507				
	19	0.5267	-0.7970	0.2199	0.5638	0.5146				
	24	0.5427	-0.8389	0.2019	0.5547	0.4756				
	29	0.5592	-0.9105	0.1774	0.5253	0.4374				
	34	0.5792	-0.9453	0.1696	0.5140	0.4225				
	39	0.5804	-0.9562	0.1510	0.4817	0.3926				
	44	0.5950	-0.9717	0.1338	0.4352	0.3434			225	conversion tape : WW8438 pte.me2mm.C312 label: 2 reorganisation tape: WW8439 pte.me2mm.R312 label: 4 sample interval : 10 ms number of values : 47000 conversion factor : $1 = 4.3154 \times 10^{-5}$ m/s
	54	0.6098	-1.024	0.1089	0.3683	0.2665				
	64	0.6253	-1.077	0.0803	0.2917	0.1856				
	74	0.6331	-1.017	0.0581	0.2109	0.1126				
	84	0.6384	-1.041	0.0388	0.1151	0.0338				
	89	0.6390	-1.052	0.0561	0.0510	0.0027				
	74	0.6340	-0.9307	0.0616	0.2188	0.1159	45	remark: reorganised data on this label (4), also on tape: WW6681/pte.mv2mm.R312/ label: 2		
	44	0.5950	-1.038	0.1444	0.4496	0.3746				
	24	0.5546	-0.8914	0.1871	0.5450	0.4522				
	9	0.4905	-0.7816	0.2459	0.5504	0.5237				
	4	0.4363	-0.7292	0.2756	0.4814	0.5281				

Table C.2 figure: 4.8										
x_1 (m)	x_3 (mm)	U_1 (m/s)	U_3 $\times 10^{-2}$ (m/s)	$\overline{u_1^2}$ $\times 10^{-2}$ (m^2/s^2)	$\overline{u_3^2}$ $\times 10^{-3}$ (m^2/s^2)	$\overline{-u_1 u_3}$ $\times 10^{-3}$ (m^2/s^2)	$\alpha + \beta$ ($^\circ$)			
16.00	2	0.3924	-0.7380	0.2261	0.3905	0.4419	45	conversion tape : WW8003 pte.mv1mm.C313 label: 3 reorganisation tape: WW8056 pte-mv1mm.R313 label: 2 sample interval : 10 ms number of values : 47000 conversion factor : $1 = 4.2187 \times 10^{-5}$ m/s		
	4	0.4280	-0.6655	0.2362	0.4248	0.4948				
	7	0.4587	-0.6344	0.2378	0.4492	0.5015				
	9	0.4749	-0.4685	0.2274	0.4665	0.4831				
	14	0.5031	-0.4529	0.2100	0.4863	0.4717				
	19	0.5197	-0.4405	0.2057	0.4850	0.4616				
	29	0.5557	-0.4576	--	0.4680	0.3807				
	39	0.5749	-0.4445	0.1378	0.4222	0.3523				
	54	0.6028	-0.6093	0.0969	0.3311	0.2467				
	64	0.6144	-0.3700	0.0740	0.2507	0.1607				
	84	0.6254	-0.3883	0.0382	0.1054	0.0461			225	
	54	0.5993	-0.3319	0.1027	0.3484	0.2537				
	29	0.5530	-0.2751	0.1747	0.4945	0.4149				
		9	0.4843	-0.2896	0.2219	0.4441	0.4467	45		
		4	0.4391	-0.2932	0.2340	0.3705	0.4120			
		2	0.4092	-0.2480	0.2231	0.3053	0.3409			

Table C.3 figure: 4.7

x_1 (m)	x_2 (m)	x_3 (mm)	U_1 (m/s)	U_3 $\cdot 10^{-2}$ (m/s)	$\overline{u_1^2}$ $\cdot 10^{-2}$ (m^2/s^2)	$\overline{u_3^2}$ $\cdot 10^{-3}$ (m^2/s^2)	$\overline{-u_1 u_3}$ $\cdot 10^{-3}$ (m^2/s^2)	$\alpha + \beta$ ($^\circ$)	
16.00	0.0 **	4	0.4161	-1.049	0.3121	0.6078	0.5842	45	conversion tape : WW8438 pte.mv2mm.C315 label: 3 reorganisation tape: WW8439 pte.mv2mm.R315 label: 5 sample interval : 10 ms (**: 2 ms) number of values : 41000 (**: 445000) conversion factor : $1 = 4.3154 \cdot 10^{-5}$ m/s remark: reorganised data also on tape: WW6681/pte.mv2mm.R315/label: 1
	0.025	2	0.4261	-0.9777	0.2814	0.4812	0.5550		
	0.025	9	0.4925	-1.127	0.2580	0.5633	0.5897		
	0.025	19	0.5410	-1.177	0.2144	0.5479	0.5162		
	0.025	54	0.6211	-1.250	0.0993	0.3473	0.2555		
	-0.025	2	0.4168	-0.9243	0.2558	0.5348	0.5436		
	-0.025	9	0.4866	-1.092	0.2432	0.5851	0.5692		
	-0.025	19	0.5374	-1.196	0.2036	0.5536	0.4883		
	-0.025	54	0.6164	-1.391	0.0942	0.3402	0.2378		

Table C.4 figures: 4.13, 4.16

x_1 (m)	x_3 (mm)	U_1 (m/s)	U_3 $\cdot 10^{-2}$ (m/s)	$\overline{u_1^2}$ $\cdot 10^{-2}$ (m^2/s^2)	$\overline{u_3^2}$ $\cdot 10^{-3}$ (m^2/s^2)	$\overline{-u_1 u_3}$ $\cdot 10^{-3}$ (m^2/s^2)	$\overline{-u_1 u_3}$ $\cdot 10^{-3}$ (m^2/s^2)	$\alpha + \beta$ ($^\circ$)	
15.79	14	0.3535	7.735	0.5703	0.6350	0.0615	0.9989	56	conversion tape : WW8831 pte.mv2mm.C075 label: 2 reorganisation tape: WW8832 pte.mv2mm.R075 label: 2 sample interval : 10 ms number of values : 23500 conversion factor : $1 = 4.2577 \cdot 10^{-5}$ m/s
15.83	23	0.4211	9.707	0.5094	0.5329	0.1117	1.100	56	
15.87	31	0.4130	9.707	0.5845	0.5837	0.1583	1.028	56	
15.91	41	0.5010	10.03	0.5147	0.4940	0.0887	0.9760	54	
15.95	44	0.5127	8.794	0.5187	0.5009	0.1473	0.9172	54	
15.99	55	0.5352	7.825	0.4895	0.5339	0.2934	0.9041	51	
16.03	60	0.5614	5.664	0.4517	0.5311	0.4241	0.8162	50	
16.07	63	0.5823	4.659	0.4504	0.5359	0.5306	0.8410	50	
16.12	66	0.5477	2.355	0.5439	0.7182	0.7937	0.9964	45	
16.17	66	0.4662	-0.3574	0.8020	1.078	1.455	1.406		
16.27	40	-0.006	2.087	0.2244	1.544	0.3459	0.4750		reorganisation tape: WW8832 pte.mv2mm.R077 label: 5 sample interval : 10 ms number of values : 23500 conversion factor : $1 = 4.2577 \cdot 10^{-5}$ m/s
	50	0.0302	1.024	0.4573	3.124	1.091	1.307		
	56	0.1046	-0.7616	0.9467	5.110	3.017	2.666		
	60	0.1864	-1.296	1.319	5.592	4.117	3.548		
	64	0.2819	-1.170	1.634	5.662	4.962	4.274		
	66	0.3352	-1.817	1.786	5.555	5.202	4.507		
	68	0.3856	-2.040	1.897	5.181	5.214	4.465		
	70	0.4219	-1.740	1.795	4.639	4.807	4.233		
	74	0.5616	-1.713	1.447	3.274	3.679	3.341		
16.39	2	-0.005	-0.7614	1.331	3.768	1.477	3.605		conversion tape : WW8831 pte.mv2mm.C076 label: 1 reorganisation tape: WW8832 pte.mv2mm.R076 label: 1 sample interval : 10 ms number of values : 23500 conversion factor : $1 = 4.2577 \cdot 10^{-5}$ m/s
	6	0.0159	-1.548	1.404	7.850	2.574	3.031		
	10	0.0314	-2.001	1.445	10.80	3.901	0.0054		
	20	0.0723	-3.230	1.668	16.28	5.574	3.566		
	40	0.2278	-6.899	2.304	18.59	10.56	7.564		
	60	0.4779	-10.68	2.129	13.68	10.26	7.663		
	100	0.7675	-9.764	0.2120	1.079	0.4166	0.2719		
	140	0.8158	-7.346	0.0747	0.4177	0.2053	0.1729		
	180	0.8711	-6.266	0.0519	0.4911	0.0596	0.0610		

Table C.5 figure: 4.13

x_1 (m)	x_3 (mm)	U_1 (m/s)	U_3 *10 ⁻² (m/s)	$\overline{U_1^2}$ *10 ⁻² (m ² /s ²)	$\overline{U_3^2}$ *10 ⁻³ (m ² /s ²)	$-\overline{U_1 U_3}$ *10 ⁻³ (m ² /s ²)	$-\overline{U_t U_n}$ *10 ⁻³ (m ² /s ²)	$\alpha+\beta$ (°)		
15.45	2	0.5343	-0.2170	0.2359	0.3208	0.5034	--	45	conversion tape : WW8831 pte.mv2mm.C075 label: 2 reorganisation tape: WW8832 pte.mv2mm.R075 label: 2 sample interval : 10 ms number of values : 23500 conversion factor : 1 = 4.2577*10 ⁻⁵ m/s	
	4	0.5626	0.2764	0.2178	0.3080	0.4664	--			
	6	0.5790	0.5477	0.1820	0.3219	0.4268	--			
	8	0.5954	0.6264	0.1470	0.3116	0.3554	--			
	10	0.6042	1.121	0.1394	0.3397	0.3840	--			
	14	0.6188	1.194	0.1152	0.3819	0.3731	--			
	18	0.6268	1.160	0.0982	0.3986	0.3178	--			
	25	0.6419	1.874	0.0984	0.4131	0.2960	--			
	35	0.6594	1.858	0.0909	0.4349	0.2970	--			
	55	0.6864	1.809	0.0846	0.4577	0.2769	--			
	75	0.7071	1.640	0.0744	0.4966	0.2990	--			
	100	0.7340	1.494	0.0603	0.4254	0.2531	--			
	120	0.7551	1.291	0.0531	0.3580	0.2245	--			
	175	0.8209	0.0157	0.0209	0.1685	0.0781	--			
185	0.8325	-0.3006	0.0194	0.1385	0.0538	--				
15.79	16	0.3757	8.030	0.5045	0.6082	0.1576	1.053	45	conversion tape : WW8831 pte.mv2mm.C076 label: 1 reorganisation tape: WW8832 pte.mv2mm.R076 label: 1 sample interval : 10 ms number of values : 23500 conversion factor : 1 = 4.2577*10 ⁻⁵ m/s	
	18	0.4026	8.255	0.4668	0.6399	0.0981	0.8835			
	20	0.4285	9.044	0.4549	0.7606	0.4823	1.206			
	25	0.4671	9.729	0.4821	0.8689	0.8112	1.534			
	35	0.5275	10.74	0.4216	0.7929	0.7536	1.362			
	50	0.5937	10.87	0.2322	0.5873	0.5106	0.7853			
	75	0.6526	10.34	0.1162	0.4980	0.3723	0.4567			
	100	0.6913	9.249	0.0843	0.4498	0.2634	0.3057			
170	0.7838	6.771	0.0404	0.2565	0.1426	0.1530				
16.07	63	0.6114	6.953	0.4228	0.5370	0.2972	0.7047	49		
	65	0.6403	6.740	0.3797	0.5532	0.2962	0.6269			45
	67	0.6567	7.013	0.3634	0.5567	0.3435	0.6609			
	72	0.6764	7.206	0.3021	0.6383	0.4700	0.7111			
	80	0.7045	7.162	0.2542	0.6798	0.4938	0.6709			
	95	0.7466	6.279	0.1896	0.5997	0.4630	0.5646			
	110	0.7705	4.845	0.1038	0.5157	0.3196	0.3498			
	140	0.7970	0.9410	0.0657	0.4566	0.2480	0.2504			
180	0.8304	-7.141	0.0402	0.2941	0.1006	0.0899				
16.17	68	0.5579	0.2339	0.5453	0.7498	0.9811	1.006	45	conversion tape : WW8831 pte.mv2mm.C077 label: 4 reorganisation tape: WW8832 pte.mv2mm.R077 label: 5 sample interval : 10 ms number of values : 23500 conversion factor : 1 = 4.2577*10 ⁻⁵ m/s	
	70	0.6074	0.5703	0.5251	0.6334	0.7893	0.8295			
	74	0.6887	1.428	0.3422	0.4840	0.4689	0.5032			
	78	0.7100	2.091	0.2719	0.5202	0.4273	0.4917			
	85	0.7382	3.022	0.2195	0.5674	0.4031	0.4671			
	95	0.7633	3.525	0.1884	0.6121	0.4637	0.5194			
	110	0.7919	3.994	0.1268	0.5621	0.3763	0.4100			
	130	0.8327	3.579	0.0782	0.4664	0.2717	0.2844			
	150	0.8543	3.810	0.0600	0.4270	0.2309	0.2378			
	180	0.9049	3.783	0.0429	0.3346	0.1247	0.1282			

Table C.6 figures: 4.14, 4.16									
x_1 (m)	x_3 (mm)	U_1 (m/s)	U_3 *10 ⁻² (m/s)	$\overline{u_1^2}$ *10 ⁻² (m ² /s ²)	$\overline{u_3^2}$ *10 ⁻³ (m ² /s ²)	$-\overline{u_1 u_3}$ *10 ⁻³ (m ² /s ²)	$-\overline{u_t u_n}$ *10 ⁻³ (m ² /s ²)	$\alpha+\beta$ (°)	
15.81	12	0.3087	6.187	0.5317	0.6108	0.0695	0.9684	45	conversion tape : WW8831 pte.mv2mm.CO81 label: 5 reorganisation tape: WW8832 pte.mv2mm.R081 label: 6
15.84	16	0.3520	7.821	0.5185	0.5794	0.0318	1.002		
15.87	21	0.3812	8.451	0.5198	0.6043	0.0914	1.054		
15.90	25	0.3287	6.210	0.4953	0.5990	0.1160	0.9023		
15.93	32	0.3644	6.102	0.4426	0.5709	0.3039	0.9149		
15.96	36	0.3465	4.681	0.4003	0.5651	0.2538	0.7012		
16.02	56	0.4803	5.634	0.3668	0.5779	0.4226	0.7692	conversion tape : WW8831 pte.mv2mm.CO81 label: 5 reorganisation tape: WW8832 pte.mv2mm.R081 label: 7	
16.05	60	0.5225	5.329	0.3613	0.5550	0.4235	0.7194		
16.08	62	0.5092	3.760	0.4291	0.6657	0.5541	0.8130		
16.11	66	0.5370	1.934	0.4573	0.6245	0.7008	0.8435		
16.14	66	0.5017	-1.308	0.5190	0.7369	0.9406	0.8228		
16.30	4	-0.1094	0.7736	0.4535	0.8135	0.1951	0.0658	conversion tape : WW8831 pte.mv2mm.CO83 label: 3 reorganisation tape: WW8832 pte.mv2mm.R083 label: 3 sample interval : 10 ms number of values : 23500 conversion factor : 1 = 4.2577*10 ⁻⁵ m/s	
	8	-0.1084	1.195	0.4231	1.115	0.3632	0.0146		
	12	-0.0951	1.652	0.4462	1.347	0.4688	0.0865		
	20	-0.0883	2.181	0.5045	1.943	0.7668	0.0451		
	25	-0.0777	2.604	0.5450	2.532	0.9144	0.1478		
	35	-0.0122	1.337	0.7594	4.137	2.128	1.907		
	45	0.1049	-0.3805	1.284	6.867	4.351	4.121		
	50	0.1568	-1.203	1.546	8.155	5.421	4.798		
	55	0.2295	-2.226	1.554	7.883	5.613	4.779		
	60	0.2934	-2.552	1.736	8.426	6.484	5.610		
	70	0.4595	-3.177	1.703	6.495	5.823	5.033		
	90	0.7017	-2.401	0.4006	1.608	0.9508	0.8648		
110	0.7575	-2.058	0.1882	0.7211	0.4491	0.4160			
140	0.7966	-1.048	0.0860	0.5050	0.2741	0.2690			
180	0.8332	1.130	0.0595	0.3621	0.1898	0.1930			
16.45	4	0.0082	-1.113	1.203	5.116	1.934	3.874		
	10	0.0434	-2.578	1.386	9.866	3.179	0.2316		
	15	0.0893	-2.746	1.569	12.66	4.471	4.549		
	25	0.1551	-4.794	1.928	14.45	6.395	3.912		
	30	0.2113	-5.488	1.997	14.32	8.043	5.643		
	40	0.2940	-6.709	1.922	14.17	7.509	5.662		
	45	0.3210	-7.803	1.938	14.89	7.726	5.826		
	50	0.3695	-8.366	1.974	12.63	7.820	5.516		
	60	0.4636	-9.337	1.871	10.13	7.108	4.890		
	75	0.5916	-9.200	1.173	5.513	4.059	2.929		
	100	0.7087	-7.783	0.2686	1.454	0.6593	0.5090		
	140	0.7566	-5.259	0.0943	0.4832	0.2576	0.2231		
180	0.7967	-3.810	0.0732	0.3626	0.2418	0.2234			

Table C.7 figure: 4.14									
x_1 (m)	x_3 (mm)	U_1 (m/s)	U_3 $\cdot 10^{-2}$ (m/s)	$\overline{u_1^2}$ $\cdot 10^{-2}$ (m^2/s^2)	$\overline{u_3^2}$ $\cdot 10^{-3}$ (m^2/s^2)	$-\overline{u_1 u_3}$ $\cdot 10^{-3}$ (m^2/s^2)	$-\overline{u_t u_{n3}}$ $\cdot 10^{-3}$ (m^2/s^2)	$\alpha+\beta$ ($^\circ$)	
15.45	2	0.4983	0.2984	0.2987	0.4443	0.6198	--	45	conversion tape : WW8831 pte.mv2mm.C081 label: 5 reorganisation tape: WW8832 pte.mv2mm.R081 label: 7 sample interval : 10 ms number of values : 23500 conversion factor : $1 = 4.2577 \cdot 10^{-5} m/s$
	4	0.5232	0.6621	0.2945	0.4643	0.6045	--		
	6	0.5464	0.9402	0.3032	0.4920	0.6387	--		
	10	0.5772	1.636	0.2674	0.5285	0.6311	--		
	20	0.6232	2.575	0.2291	0.5476	0.6260	--		
	40	0.6807	2.809	0.1315	0.4621	0.3766	--		
	70	0.7110	2.941	0.0865	0.4503	0.2580	--		
	90	0.7259	2.879	0.0692	0.4108	0.2270	--		
	140	0.7632	2.132	0.0479	0.3225	0.1955	--		
180	0.7923	0.4606	0.0266	0.1901	0.1003	--			
15.81	16	0.2989	5.858	0.5897	0.7123	0.2550	0.7434		
	18	0.2481	4.219	0.6223	0.7377	0.2774	0.6494		
	24	0.3710	6.792	0.5607	0.5795	0.2851	1.159		
	30	0.4468	9.174	0.4813	0.8163	0.5898	1.329		
	35	0.4772	10.11	0.4068	0.9471	0.7149	1.288		
	40	0.5066	10.27	0.4156	0.9367	0.7812	1.348		
	50	0.5582	10.22	0.3551	0.8304	0.7101	1.147		
	75	0.6537	9.426	0.1706	0.5713	0.4393	0.5816		
	100	0.6890	8.076	0.0920	0.4510	0.2790	0.3258		
140	0.7322	5.119	0.0652	0.3808	0.2390	0.2555			
180	0.7768	0.1857	0.0358	0.2299	0.1000	0.1030			
16.02	55	0.5136	7.525	0.4864	0.5738	0.3931	0.9895		
	57	0.5591	8.053	0.4204	0.5956	0.4042	0.8972		
	60	0.5759	8.329	0.4057	0.6480	0.4581	0.9207		
	63	0.5931	8.437	0.3741	0.6912	0.4743	0.8809		
	66	0.6101	8.401	0.3544	0.6913	0.4987	0.8639		
	70	0.6319	9.078	0.3275	0.7506	0.5526	0.8865		
	80	0.6665	9.328	0.3063	0.8504	0.6915	0.9697		
	100	0.7242	8.655	0.2193	0.6657	0.5684	0.7320		
	140	0.7680	5.516	0.0703	0.4656	0.2403	0.2548		
180	0.7929	2.359	0.0481	0.3205	0.1280	0.1325			
16.17	66	0.5100	-1.357	0.5399	0.7783	0.9660	0.8438		
	68	0.5570	-0.8128	0.4597	0.6511	0.8032	0.7478		
	70	0.6100	0.1237	0.4213	0.5824	0.5424	0.6179		
	75	0.6646	1.220	0.3240	0.5619	0.4188	0.4699		
	90	0.7230	2.541	0.2608	0.7603	0.5529	0.6160		
	110	0.7789	1.885	0.2034	0.6632	0.5197	0.5526		
	140	0.8163	0.4215	0.0691	0.4460	0.2076	0.2089		
180	0.8566	-2.477	0.0461	0.3192	0.1370	0.1325			

Table C.8 figures: 4.15, 4.16

x_1 (m)	x_3 (mm)	U_1 (m/s)	U_3 $\cdot 10^{-2}$ (m/s)	$\overline{u_1^2}$ $\cdot 10^{-2}$ (m^2/s^2)	$\overline{u_3^2}$ $\cdot 10^{-3}$ (m^2/s^2)	$-\overline{u_1 u_3}$ $\cdot 10^{-3}$ (m^2/s^2)	$-\overline{u_t u_n}$ $\cdot 10^{-3}$ (m^2/s^2)	$\alpha+\beta$ ($^\circ$)	
15.45	2	0.5142	0.0996	0.3026	0.3465	0.5321	--	45	conversion tape : WW8831 pte.mv2mm.C088 label: 6 reorganisation tape: WW8832 pte.mv2mm.R088 label: 8 sample interval : 10 ms number of values : 23500 conversion factor : $1 = 4.2577 \cdot 10^{-5} m/s$
	4	0.5536	0.3224	0.3223	0.3937	0.5892	--		
	6	0.5762	0.6078	0.3114	0.3900	0.5566	--		
	8	0.5903	0.8629	0.2797	0.3973	0.5558	--		
	10	0.6022	1.032	0.2599	0.4113	0.5489	--		
	15	0.6335	1.625	0.1825	0.4221	0.4765	--		
	30	0.6735	2.159	0.1290	0.4776	0.3811	--		
	75	0.7197	2.192	0.0889	0.4382	0.2652	--		
	110	0.7418	1.955	0.0629	0.3917	0.2186	--		
	140	0.7607	1.519	0.0472	0.3183	0.1757	--		
180	0.7798	0.1731	0.0260	0.2049	0.0758	--			
15.82	29	0.4703	8.388	0.4067	0.8369	0.4476	0.9777		
	31	0.4744	9.582	0.3953	1.005	0.7466	1.259		
	35	0.5023	9.648	0.4255	1.040	0.8635	1.573		
	37	0.5074	9.787	0.4452	1.039	0.8734	1.618		
	39	0.5165	10.00	0.4523	1.093	0.9063	0.9903		
15.87	32	0.4762	9.673	0.3816	0.7153	0.3764	0.9522		
	34	0.4894	9.882	0.3471	0.8499	0.5194	0.9867		
	36	0.4965	9.877	0.3805	0.9928	0.7188	1.204		
	38	0.4976	9.777	0.3919	0.7228	0.3775	0.9533		
	40	0.5166	9.889	0.3575	0.8038	0.4909	0.9665		
	42	0.5302	8.859	0.3903	0.8197	0.4474	0.9250		
15.92	43	0.4630	7.708	0.4947	0.7649	0.2053	0.8749		
	45	0.5042	8.599	0.5119	0.5987	0.2266	0.9596		
	47	0.5393	9.383	0.3793	0.7403	0.4282	0.9199		
	49	0.5571	9.544	0.3472	0.8168	0.5183	0.9298		
	51	0.5605	9.913	0.3691	0.8890	0.6058	1.048		
	53	0.5661	9.791	0.3563	0.9458	0.6859	1.085		
15.97	50	0.5016	7.591	0.5168	0.6137	0.3025	0.9623		
	52	0.5217	7.533	0.4603	0.6147	0.3079	0.8584		
	54	0.5666	9.202	0.3631	0.7143	0.4431	0.8808		
	56	0.5744	8.791	0.3459	0.7473	0.5027	0.8852		
	58	0.5877	8.213	0.3840	0.7820	0.6080	1.006		
	60	0.5974	7.964	0.3736	0.8061	0.5743	0.9383		
16.02	56	0.5233	6.393	0.4486	0.5869	0.3909	0.9132		
	58	0.5606	6.812	0.4330	0.5961	0.3970	0.8923		
	60	0.5780	7.063	0.4106	0.6406	0.4324	0.8600		
	62	0.5981	7.377	0.3814	0.6603	0.4817	0.8556		
	64	0.6129	7.458	0.3648	0.6728	0.4601	0.8529		
	66	0.6233	7.748	0.3208	0.7119	0.4472	0.7397		
16.07	59	0.5178	4.814	0.4981	0.6428	0.4003	0.7925		
	61	0.5605	4.950	0.4280	0.6020	0.4671	0.7793		
	63	0.5786	5.403	0.4257	0.6050	0.4310	0.7595		
	65	0.6080	5.820	0.3890	0.6716	0.4806	0.7788		
	67	0.6288	5.349	0.3606	0.6885	0.5199	0.7606		
	69	0.6403	5.554	0.3538	0.6999	0.5061	0.7448		
16.12	67	0.6235	3.566	0.3872	0.5800	0.4824	0.6684		
	69	0.6409	4.484	0.3520	0.6406	0.5011	0.6966		
	71	0.6552	4.437	0.3230	0.6477	0.4422	0.6133		
	73	0.6677	4.379	0.3086	0.6820	0.5041	0.6586		

x_1 (m)	x_3 (m)	U_1 (m/s)	U_3 (m/s)	k $\cdot 10^{-3}$ (m^2/s^2)	ϵ $\cdot 10^{-3}$ (m^2/s^2)	
15.25	0.000	--	--	--	--	$u_* = 0.0230$ m/s
	0.002	0.497	0.0	1.747	15.21	$z_0 = 0.35 \cdot 10^{-6}$ m
	0.004	0.537	0.0	1.730	7.604	
	0.006	0.561	0.0	1.713	5.070	
	0.009	0.584	0.0	1.688	3.380	
	0.012	0.600	0.0	1.663	2.535	
	0.017	0.620	0.0	1.621	1.789	
	0.025	0.643	0.0	1.553	1.217	
	0.035	0.662	0.0	1.469	0.869	
	0.050	0.683	0.0	1.343	0.608	
	0.070	0.702	0.0	1.176	0.044	
	0.100	0.722	0.0	0.924	0.304	
	0.140	0.742	0.0	0.588	0.217	
	0.180	0.756	0.0	0.252	0.169	
	0.210	--	--	--	--	

experiment: T1			experiment: T2			experiment: T3			conveyor-belt velocity
x_1 (m)	z_b (mm)	water-level (m)	x_1 (m)	z_b (mm)	water-level (m)	x_1 (m)	z_b (mm)	water-level (m)	
15.75	0		15.75	0		15.75	0		c_b (m/h)
15.79	12	0.213	15.81	12	0.212	15.82	25	0.220	
15.83	21		15.84	16		15.87	29	0.215	exp. T1:
15.87	28		15.87	21		15.92	40	0.215	<u>4.13</u>
15.91	38		15.90	25		15.97	47	0.215	
15.95	41		15.93	32		16.02	53	0.215	exp. T2
15.99	52		15.96	36		16.07	56	0.210	<u>3.75</u>
16.03	57		15.99	42		16.12	60	0.210	
16.07	59	0.211	16.02	50	0.211	16.17	60	0.210	exp. T3
16.12	63		16.05	56		16.25	0		<u>3.58</u>
16.17	63	0.215	16.08	58					
16.25	0		16.11	62					
			16.14	63					
			16.17	63	0.206				
			16.25	0					

Table C.11 angles of streamlines in measurements and calculation (γ_m angle from measurements γ_c angle from calculation)																								
exp	x_1 (m)	x_3 (mm)	γ_m ($^\circ$)	γ_c ($^\circ$)	exp	x_1 (m)	x_3 (mm)	γ_m ($^\circ$)	γ_c ($^\circ$)	exp	x_1 (m)	x_3 (mm)	γ_m ($^\circ$)	γ_c ($^\circ$)	exp	x_1 (m)	x_3 (mm)	γ_m ($^\circ$)	γ_c ($^\circ$)					
T1	15.79	16	12.1	13.1	T1	15.95	44	9.7	10.2	T2	16.45	4	-53.6	-1.1	T3	16.02	62	7.0	6.7					
		18	11.6	12.5		15.99	55	8.3	9.5			10	-30.7	-2.6			64	6.9	6.6					
		20	11.9	12.0		16.03	60	5.8	6.9			15	-17.1	-3.8			66	7.1	6.4					
		25	11.8	11.4		16.07	63	4.6	3.7			25	-17.2	-4.7			16.07	59	5.3	3.6				
		35	11.5	9.5		16.12	66	2.5	0.0			30	-14.6	-4.6				61	5.0	3.6				
		50	10.4	8.4		16.17	66	-0.4	-16.9			40	-12.9	-4.2				63	5.3	3.7				
		75	9.0	5.9		T2	15.81	16	11.1			11.4	45	-13.7				-3.9	65	5.5	3.8			
		100	7.6	4.4			18	9.7	11.3			50	-12.8	-3.5				67	4.9	3.8				
		170	4.9	1.4		24	10.4	10.8	60			-11.4	-3.0	69			5.0	3.8						
		16.07	63	6.5		3.7	30	11.6	10.0			75	-8.8	-2.3			16.12	67	3.3	0.0	16.07	67	3.3	0.0
65	6.0			3.8	35	12.0	9.7	100	-6.3	-1.7	69	4.0	0.0											
67	6.1			3.8	40	11.5	9.4	140	-4.0	-1.0	71	3.9	0.0											
72	6.1			3.7	50	10.4	8.4	180	-2.7	-0.3	73	3.8	0.0											
80	5.8			3.6	75	8.2	6.5	15.81	14	11.3	11.5	15.84	19	12.5	11.2									
95	4.8			2.9	100	6.7	4.8		15.84	19	12.5			11.2	15.87	24			12.5	11.2				
110	3.6			2.4	140	4.0	3.0		15.87	24	12.5			11.2	15.90	28			10.7	11.2				
140	0.7			1.8	180	1.4	1.4		15.90	28	10.7			11.2	15.93	35			9.5	11.2				
16.17	68			0.3	-13.9	16.02	55		8.3	7.2	15.93			35	9.5	11.2			15.96	40			7.7	10.2
				70	0.5				-9.3	57	8.2			7.1	16.02	56			6.7	7.1			16.05	60
		74	1.2	-7.9	60				8.2	6.9	63			8.1	6.6	16.08	62	4.2	3.6					
		78	1.7	-6.7	66				7.8	6.4	70			8.2	6.1	16.11	66	2.1	0.0					
		85	2.3	-5.8	70				8.2	6.1	80			8.0	5.5	16.14	66	-1.5	0.0					
		95	2.6	-4.7	80				8.0	5.5	100			6.8	4.2	T3	15.82	29	10.1	10.5				
		110	2.9	-3.7	100			6.8	4.2	15.82	29	10.1	10.5	31	11.4			10.3						
		130	2.5	-2.9	140			4.1	2.0	31	11.4	10.3	35	10.9	9.9									
		150	2.6	-2.0	180			1.7	0.9	35	10.9	9.9	37	10.9	9.8									
		180	2.4	-1.5	16.17			66	-1.5	-16.9	37	10.9	9.8	15.87	32			11.5	11.0					
16.27	40	-74.9	-9.2	68		-0.8	-13.9		34	11.4	10.7													
		50	18.7	-6.4		70	1.2		-11.2	36	11.3	10.5												
		56	-4.2	-6.4		75	1.1		-7.9	38	11.1	10.4												
		60	-4.0	-6.2		90	2.0		-5.8	40	10.8	10.2												
		64	-3.5	-6.0		110	1.4		-3.7	42	9.5	10.0												
		66	-3.1	-5.5		140	0.3		-2.7	15.92	43	9.5	10.6											
		68	-3.0	-5.2		180	-1.7		-1.5			45	9.7			10.4								
		70	-2.4	-5.0		16.30	4		-4.0			184.1	47			9.9	10.2							
		74	-1.7	-5.0					8			-6.3	197.7			49	9.7	9.9						
		16.39	2	-122	-1.1			12	-9.9			231.4	51	10.0	9.8									
6	-44.3			-4.7	20			-13.9	-30.0			53	9.8	9.6										
10	-32.5			-6.2	25			-18.5	-18.1			15.97	50	8.6	10.2									
20	-24.1			-8.3	35			-47.5	-10.3					52	8.2	9.8								
40	-16.8			-6.9	45			-2.1	-9.0					54	9.2	9.5								
60	-12.6			-4.0	50			-4.4	-6.0					56	8.7	9.2								
100	-7.3			-2.2	55			-5.5	-5.5	58	8.0			9.0										
140	-5.1			-1.3	60			-5.0	-5.0	60	7.6			8.8										
180	-4.1			-0.4	70	-4.0	-4.2	16.02	56	7.0	7.1													
15.79	14			12.3	13.1	90	-2.0			-3.5	58			6.9	7.0									
		15.83	23	13.0	10	11.3	10.8			60	7.0			6.9										
		15.87	31	13.2	110	-1.6	-3.0																	
		15.91	41	11.3	140	-0.8	-2.0																	
				180	0.8	-0.7																		